D. G. Bakker

A Lasercom terminal for CubeSats

Sizing, analysis and experimental verification

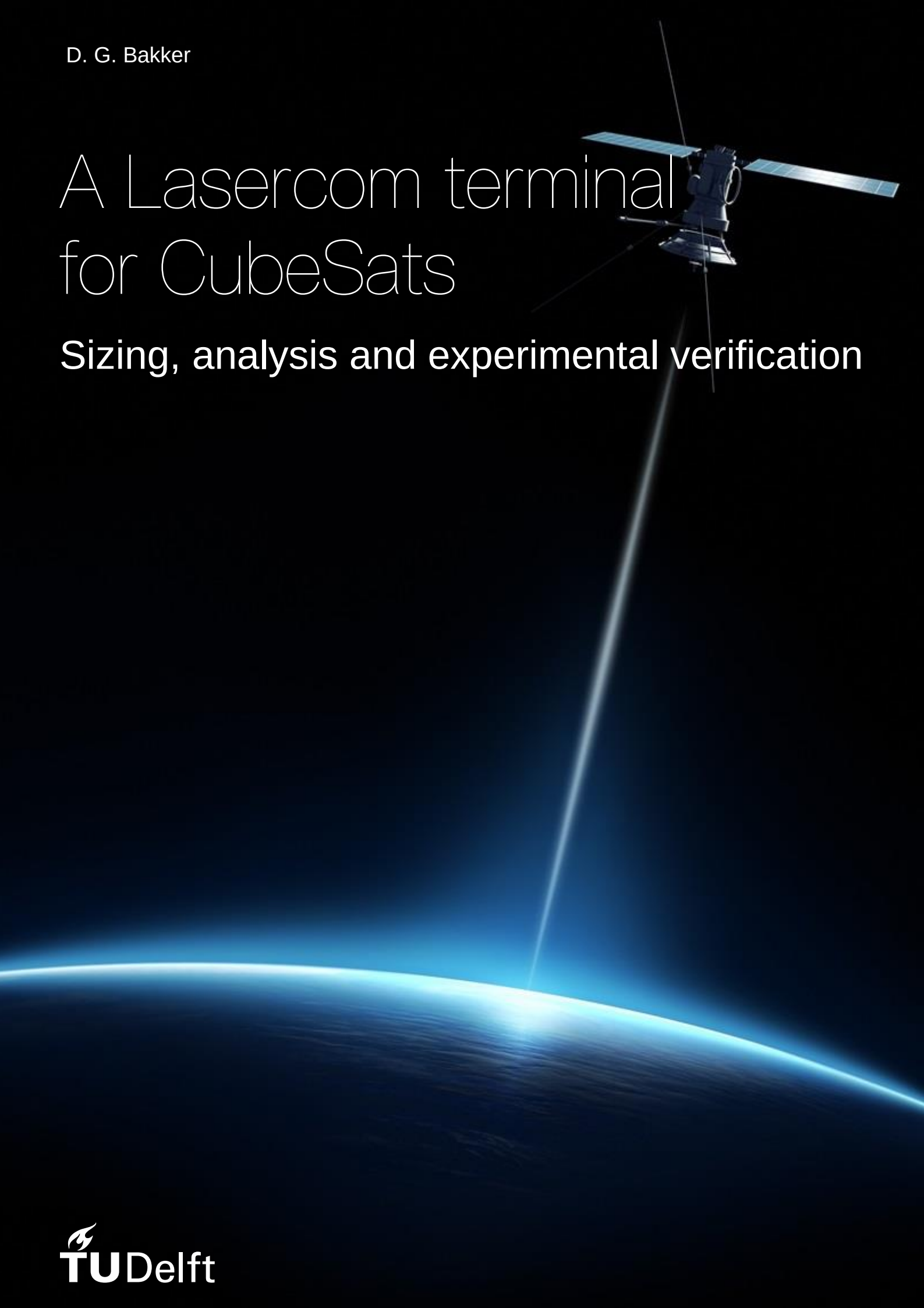

TU Delft

A Lasercom terminal for CubeSats

Sizing, analysis and experimental verification

By

Daniël Gerardus Bakker

in partial fulfilment of the requirements for the degree of

Master of Science
in Aerospace Engineering

at the Delft University of Technology,
to be defended publicly on Friday July 6, 2018 at 9:30 AM.

Supervisor:	Dr. ir. C. Verhoeven	TU Delft
Thesis committee:	Dr. ir. G.L.M. Monna,	Hyperion Technologies
	Dr. G.A. Bohlin,	TU Delft
	Dr. S. Speretta,	TU Delft

TU Delft

Preface

This report contains a description of my thesis work as performed at Hyperion Technologies B.V. for the Lasercom project. Under this project Hyperion is developing optical communication technology in collaboration with the Dutch research institute TNO. In this collaboration Hyperion is responsible for the electronic aspects of the designed Lasercom systems and the integration of these systems in satellites, while TNO is responsible for the optical and photonics design.

I would like to thank Dr. ir. Bert Monna and Dr. ir. Steven Engelen for giving me the opportunity to work on this project as part of my master's thesis for Aerospace Engineering at the TU Delft. Bert, thank you for your advice and the sparring sessions we had, I'm certain that many more will follow. Steven, thank you as well for all your advice on pretty much any subject, and sorry for not making this project the first CubeSAT with a blu-ray laser on board.

Dr. ir. Chris Verhoeven, thank you very much for accepting the role of supervisor and placing your confidence in me. I enjoyed our discussions on the Smallsat trip, perhaps we will run into each other in the future again.

Daniël Bakker
Delft, June 2018

Contents

Abstract

In the past few years there is a trend that one of the smallest classes of satellites, CubeSats, are used increasingly often by commercial parties. The low cost and time required to develop and launch a CubeSat, compared to classic large satellites, has opened up many business opportunities in space. The low launch costs of a CubeSat allow for the launch of constellations of satellites, where the impact of the failure of one satellites is small. This allows for a different design philosophy than with classic satellites, the common development approach for CubeSats is to use commercial off-the-shelf (COTS) components and technologies wherever possible. This has also allowed for quick advances in the functionality and usefulness of these satellites. The extensive usage of COTS components and technologies allows CubeSat designers to employ recent technological advancements in their satellites, such as increasingly sophisticated and miniaturised high-resolution sensors and imagers. Due to this trend, commercial CubeSats generate increasingly large amounts of data.

Up until now CubeSats have employed radio-based communication systems to transfer this data to earth. This is a relatively cheap and reliable method, but the CubeSat size and power constraints limit the maximum datarate that can be achieved using a radio system. Furthermore, the radio spectrum is becoming increasingly crowded due to the increasing number of spacecraft which makes obtaining a license for the use of radio-based system increasingly difficult. Laser-based communication systems, also called lasercom, have the ability to transfer much larger amounts of data within the same power- and size constraints due to their smaller beamwidths. Since the value of commercial CubeSats is related to the data they send down, the larger the amount of data a CubeSat can send to earth, the more profitable this satellite can be. The optical spectrum is unregulated and does not have to be regulated, as the narrow beamwidths used do not lead to interference between satellites or other spectrum users.

Research on lasercom for satellites has been carried out for years, mainly for use on larger satellites and for deep-space missions, but in the last few years also for CubeSat applications. The results obtained in this research indicate that optical communication is a viable alternative to radio-based communication, also for CubeSats. In this work a design for a lasercom system is proposed that fits within the size- and power constraints of the CubeSat platform, while also being a commercially viable alternative to radio-based communication by offering higher datarates at a competitive price. This design is made using a first-order sizing method, where analytical and numerical models are used to simulate all relevant aspects of the design, to support the performance claims of this design, by modelling and predicting its performance with sufficient accuracy.

Since lasercom systems are such a recent development, not every aspect of the proposed system design can be modelled with sufficient accuracy using a first-order sizing method. Most uncertainties and new technologies exist within the electronic design of the lasercom satellite terminal. For this reason this aspect of the design is treated in further detail. Most uncertainties in the electronic design are mitigated by proposing a practical implementation of each required functionality. In this way accurate predictions are made on the expected performance of the electronic design of the satellite terminal and areas where most development effort will be necessary are identified. Based on these predictions additional support is given for the validity of the first-order sizing model as proposed in this work.

One component of the electronic design of the satellite terminal, the quad cell receiver circuit, remains an uncertain item, as the functionality required from this circuit and the requirements imposed on this circuit by the first-order lasercom system design are stringent and quite unique. It is however not prohibitively expensive to construct and test this circuit, so for this reason a prototype implementation of this circuit was constructed in order to characterise it experimentally. From the data gathered from these experiments, it is concluded that imperfections in the experimental setup will have added an additional error in the measured circuit performance. Nevertheless, it is found that the circuit as designed meets the performance requirements as imposed by the proposed lasercom system design under different operating conditions, with a worst-case measurement error that is slightly higher than the required accuracy. It is however assumed that without the error contribution from the experimental setup, this measurement error will be within specifications.

While it is recommended to test this prototype using a more accurate and perhaps more extensive experimental setup, as in this way it can be determined whether a simple calibration procedure during production of the actual lasercom satellite terminal will be sufficient to guarantee the accuracy of the quad cell receiver circuit, the results gathered in this work are sufficient to conclude that the proposed lasercom system design is feasible, and that using this design a commercially viable lasercom system for CubeSats can be constructed.

List of symbols

Symbol	Description
b/s	Bits per second
h_o	Orbital altitude
$m_{SC,min}$	Min. spacecraft mass
$m_{SC,max}$	Max. spacecraft mass
d_{GS}	Aperture diameter ground station
L_{GS}	Ground station downlink optical losses
N_S	Detector photons per bit groundstation
P_{up}	Optical output power uplink
λ_{up}	Wavelength uplink
δ_{up}	Atmospheric angular error uplink
ϵ_{GS}	Satellite orbital position prediction error
δ_{GS}	Closed-loop pointing error ground station
α	Satellite minimum elevation angle
ϵ_{SC}	Orbital position determination error in the ADCS
δ_{SC}	Open-loop attitude determination error in the ADCS
P_{down}	Optical output power downlink
λ_{down}	Wavelength downlink
$\delta_{alignment}$	Misalignment between up/downlink channels satellite terminal
d_{SC}	Aperture diameter satellite terminal
L_{SC}	Satellite terminal uplink optical losses
l_{proj}	Projection optical length
d_{dot}	Projected light dot diameter
P_{bg}	Captured background light power
d_{QC}	Quad cell diameter
l_{QC}	Spacing between quad cells
R_λ	Quad cell sensitivity
I_d	Quad cell dark current
R_{sh}	Quad cell shunt resistance
BW_{QC}	Quad cell circuit bandwidth
I_{ch}	Total RMS output noise per quad cell channel, input referred
I_{meas}	Total RMS output noise per angle measurement channel, input referred
e_{gain}	Max. gain error between any two channels
ϵ_{off}	Max. offset error between any two channels, input referred
L_{point}	Pointing error loss
SNR_{up}	Uplink link budget signal-to-noise margin
SNR_{down}	Downlink link budget signal-to-noise margin
L_{atm}	Atmospheric losses
I_{Sat}	Minimum satellite moment of inertia
R_{max}	Maximum link distance
T_{max}	Maximum satellite time within range
Θ_b	Full-angle beacon divergence angle
δ_{act}	ADCS actuation error
$P_{up,rec}$	Captured beacon light power
I_{det}	Captured light detector RMS noise per cell
$P_{up,wc}$	Worst case convertible light power
ϵ_{angle}	Quad cell angle measurement total current error (3σ)
Θ_{up}	Uplink incoming angle range
$l_{proj,max}$	Maximum uplink projection optical length
R_Θ	Angle of incidence per dot displacement
ΔI_{det}	Minimum detectable current difference
δ_{QC}	Angle measurement accuracy

$SNR_{data,up}$	Uplink data signal-to-noise ratio
Θ_d	Full-angle downlink light divergence angle
$P_{down,det}$	Ground station detector optical power
$R_{b,down}$	Downlink bitrate
P_{buf}	Satellite terminal buffering power consumption
P_{com}	Satellite terminal communication power consumption
1U	One standard CubeSat unit, with a size of $10 \times 10 \times 10cm$
t_s	Laser diode turn-on delay
f_r	Laser diode relaxation frequency
I_s	Laser diode threshold current

1 Introduction

Over the past years the number of commercial CubeSat missions has grown significantly. The low launch cost of these small satellites, often the size of a carton of milk, already makes them an interesting candidate for commercial missions, but this also allows a different development approach compared to conventional, expensive satellites: for CubeSats, it is acceptable to take larger risks by for example allowing for the use of commercial off-the-shelf (COTS) components, as the design lifetime of CubeSats is generally short and if something fails on the satellite in orbit, it is expected to be cheaper to launch a redesigned satellite than to design a completely zero-failure satellite using conventional spacecraft engineering methods and components in the first place. The extensive usage of COTS components and technologies on CubeSats comes with great advantages: not only does it significantly reduce the development time and effort required for a CubeSat, it allows for recent technological advancements to be employed in CubeSats, such as the ongoing miniaturization of electronics and sensors. This has allowed CubeSat missions to become increasingly advanced, with high-resolution imagers, advanced radar and radio receivers, and even hyperspectral imagers.

Commercial CubeSat missions generally create their commercial value by gathering some form of data and sending this data back to earth. This can range from received radio signals, to acquired satellite imagery and to extensive measurements from for example hyperspectral imagers. This does however imply that the commercial value of a CubeSat depends on how much of this data it can acquire and send to earth. Almost all CubeSat missions use a radio link for transferring data between the satellite and a ground station, and while this is a proven and reliable technology, for modern CubeSat missions it is becoming a limitation. Within the size and power constraints of a CubeSat radio transceivers are usually limited to a datarate of several tens of Mb/s. If high-end payloads such as imagers were to acquire high-resolution data continuously, it would be impossible to send all the data gathered in an orbit down over a radio link within that same orbit. Next to this, the radio spectrum is regulated and for every satellite permission is required to use a part of the radio spectrum. With the increasing number of satellites in orbit, the radio spectrum is getting more and more crowded with different satellites potentially interfering with each other's radio links and obtaining permission to use a part of the spectrum is getting increasingly difficult.

Switching from radio-based communication to optical communication, also called lasercom, could solve these issues. By using a laser to generate the signal carrier, much narrower beamwidths can be created than what is achievable with a radio beam. Due to this fact, it is possible to achieve much higher datarates within the CubeSat size and power constraints than what is possible with a radio link. Since the commercial value generated by a commercial CubeSat typically comes from the data it sends to earth, the larger the amount of data a CubeSat can send to earth, the more profitable this satellite can be. Next to this, the optical spectrum is unregulated and does not have to be regulated, as the narrow beamwidths used do not lead to interference between satellites. Research on lasercom systems for satellites has been going on for years and has led to scientific and commercial applications of lasercom in large satellites and interplanetary/deep space missions. By applying the technology developed and the lessons learned from these developments to design a lasercom system suitable for CubeSats, would allow for a great leap in the usefulness and commercial viability of a new generation of advanced CubeSats.

In this work it will be described how a lasercom system can be constructed that fits within the constraints of the CubeSat platform, and that is a commercially viable alternative to radio-based communication systems for CubeSats. This work is conducted at Hyperion Technologies B.V. in Delft and is part of a project, initiated by Hyperion Technologies, to develop a lasercom terminal for CubeSats. This project is executed together with the Dutch research institute TNO, where Hyperion is responsible for all electronic development of this lasercom terminal and for integration with the CubeSat bus, and TNO is responsible for the optical design of the lasercom terminal, for sourcing the laser source and for supplying a reference ground station design, as this ground station is an existing project from TNO. For this reason, the focus of this work will be on the electronic aspects of the lasercom terminal.

Before the development of this lasercom system is treated, first an overview of existing lasercom systems and experiments is given in chapter 2 to illustrate the current state-of-art in this field and to allow for a comparison between existing work and the proposals made in this work. Next a baseline design for a lasercom systems that fits within the constraints of the CubeSat platform and is a commercially viable alternative to radio-based communication systems is established in chapter 0 with the use of systems engineering methods and a first-order sizing approach. In chapter 0 it will be explained that a few aspects of the proposed lasercom system baseline design are not commonly used in CubeSats or are unproven technologies, mainly in the electronic design of the lasercom terminal, and that these aspects are therefore relatively uncertain. In this chapter a detailed implementation of the proposed electronic design for the lasercom terminal is described to support the results from chapter 0. In chapter 0 it is described that for one aspect of the electronic design, the quad cell receiver, uncertainties remain after the discussion in chapter 0 and that the best way of mitigating these uncertainties is by constructing an implementation of this quad cell receiver and evaluating it experimentally. In this chapter details on this experimental implementation are given, along with the practical results obtained using this prototype. Lastly, using the results from chapters 0 and 0 conclusions are drawn on the validity and feasibility of the design proposed in chapter 0, a comparison with existing lasercom systems is made and recommendations are given for future research and development work for this project.

2 Existing reference lasercom systems

In order to evaluate the current state-of-art in optical communication between satellites and ground stations, a selection of existing satellite lasercom systems is compiled. Most of the selected reference systems have some similarity with the lasercom system design that will be proposed in this work. This similarity is either in the performance that is achieved with the reference lasercom system, or in the size and power budget of the reference system. At the end of this chapter an overview of some key design characteristics of each reference lasercom system is compiled in order to facilitate a comparison between existing lasercom systems and the results from this work.

2.1. NFIRE-TerraSAR-X

The NFIRE (Near-Field Infrared Experiment) and TerraSAR-X satellites contain a lasercom module as secondary payload, to conduct experiments on optical communication between these two satellites and between the NFIRE satellite and a ground station. Information on this project is taken from [1] and [2], a rendered drawing of the Tesat lasercom module is given in Figure 1.

The NFIRE is a relatively large LEO satellite, and thus allows for a big and heavy lasercom module. The Tesat module that is mounted on NFIRE has a complex mechanical structure with gimbals and fine steering mirrors. This terminal also features a large aperture, which all together allows for a maximum datarate of $5.625 Gb/s$ in both directions with a large pointing freedom of the lasercom aperture with respect to the satellite body. This however comes at the cost of a maximum power consumption of $120 W$ and a terminal mass of $32 kg$.

A main goal of the NFIRE lasercom experiments with the ground station was verifying the reliability of optical communication links between a spacecraft and a ground station, and in particular the effect of atmospheric disturbances. From all the communication attempts that made, only few were successful. A major issue were poor atmospheric conditions such as clouds and fog. In the early tests it was also found that strong winds influenced the ground station. These issues were mitigated by placing the ground station in a protective dome.

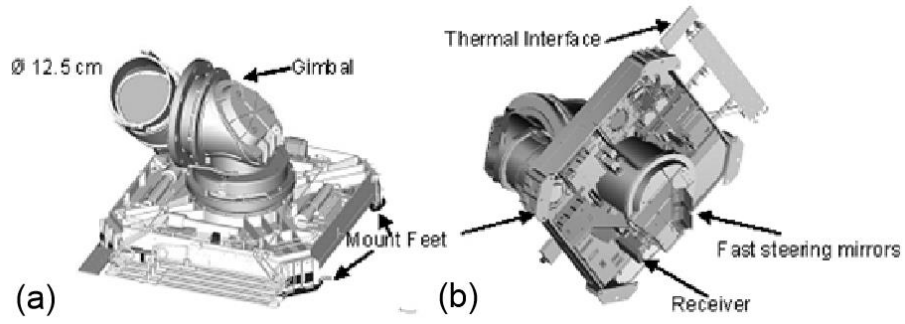

Figure 1: Tesat lasercom terminal as mounted on the NFIRE satellite [1].

2.2. SOTA

The SOTA (Small Optical TrAnsponder) is a lasercom terminal developed for LEO-to-ground optical communication. Information on this project is taken from [3], a block diagram of the final SOTA terminal is given in Figure 2. The SOTA payload is included on the SOCRATES satellite (Space Optical Communications Research Advanced Technology Satellite), an experimental satellite whose mission is to validate certain technologies. The SOCRATES is a relatively small satellite, with a mass of approximately $50kg$. With a mass of $5.9kg$ and a peak power consumption of $16W$, the SOTA has a SWaP footprint that more closely resembles CubeSat applications than the NFIRE terminal.

To allow for a multitude of experiments, amongst others on atmospheric effects, the SOTA contains four transmit laser at different wavelengths and power levels. Pointing of the full module is performed by gimbals and pointing of one of the lasers is done by a fine steering mirror, which is also capable of tracking an incoming beacon for highly accurate pointing of the laser beam. Nevertheless, the SOTA was designed for datarates of just $10Mb/s$. One of the main conclusions was that the received power from the SOTA was stronger than expected, which indicates that the sizing of the SOTA might have been too conservative.

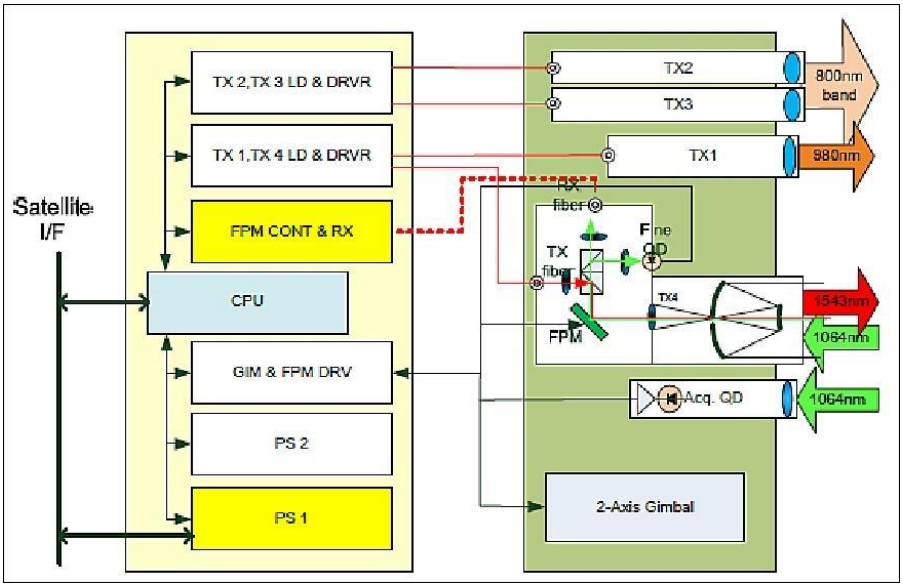

Figure 2: Final SOTA lasercom terminal block diagram [4]

2.3. VSOTA

The VSOTA (Very Small Optical TrAnsmitter) is lasercom terminal developed by the same team as the SOTA terminal. Information on this project is taken from [5] and [6]. The VSOTA is a simpler version of the SOTA, with downlink capability only. The VSOTA is also included in a 50kg-class satellite, the RISESAT, but takes up a smaller portion of the mass, size and power budgets. To accomplish this, the VSOTA terminal is mechanically fixed to the RISESAT bus: pointing of the laser beam is performed by pointing the complete satellite. The VSOTA contains two separate laser transmitters. The first one is a 980 nm transmitter with an optical power output of $270mW$ and a divergence angle of $3.5mrad$, the second one is a 1550 nm transmitter with an optical power of $40mW$ and a divergence angle of $1.3mrad$. An illustration of the VSOTA terminal is given in Figure 3.

Even though this terminal is significantly less complex than the SOTA terminal, its target datarate of $1Mb/s$ is not much lower than the maximum datarate of the SOTA. At the time of writing no experimental results of the performance of VSOTA in space are available. An interesting result the space qualification test campaign is that during a vibration test to simulate launch conditions an angular error of $0.8mrad$ was introduced in the module, which necessitates a calibration procedure in orbit.

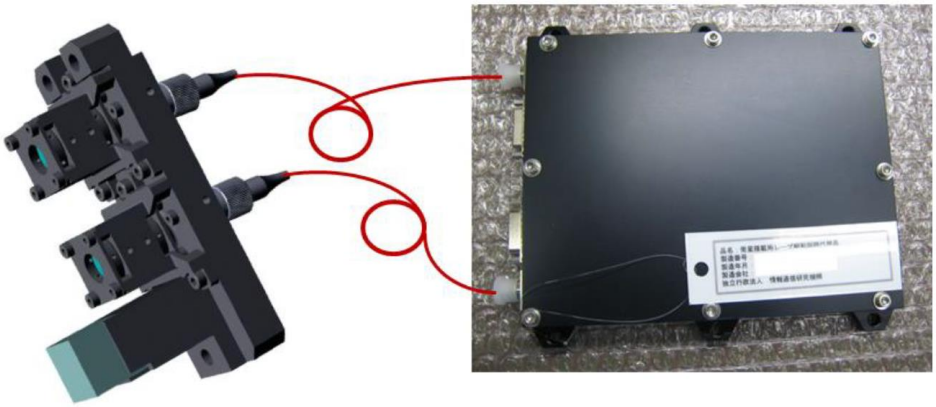

Figure 3: VSOTA terminal [6]

2.4. Aerocube-OCSD

The Aerocube is a small (1.5U) CubeSat with a mission to validate the performance of two optical experiments, of which one is a bidirectional lasercom link between the Aerocube and a ground station. Information on this project is taken from [7]. The Aerocube is a CubeSat with relatively standard specifications, such as a pointing accuracy of 0.1°. Even though there is a closed-loop pointing capability of 0.02° using an uplink beacon detector, the laser beam divergence is large at 0.3°. This necessitates the use of a high-power laser system to achieve the target datarate of $5Mb/s$. This is done by using a fiber-based optical power amplifier to achieve a nominal output power of $5W$, with $10W$ as the maximum optical output power of this laser system. The maximum heat dissipation of this powerful laser system is $40W$, which is a challenge in such a small CubeSat in terms of thermal design and electrical power requirements. These issues are solved by using a large battery power storage to accommodate the large peak power requirement and by applying a duty cycle limit of 3 minutes of active laser transmission time per orbit, to allow for the satellite to cool down.

During development of the Aerocube-OCSD it was discovered that the large optical isolator from the laser system, that had to be rated for the high power levels in the Aerocube laser system, produced a significant magnetic field that interfered with attitude determination and control, necessitating the use of Mu-metal shielding.

Due to a software error the ADCS and lasercom systems of the Aerocube failed, so no experimental data is available to validate its performance [8].

2.5. OSIRIS

The OSIRIS is a large project by DLR to develop optical communication for different applications, amongst which optical communication for satellites. Within the OSIRIS project,

two lasercom terminals for use in a 120kg-class satellite have been constructed. The first version is included in the 'Flying Laptop' from the University of Stuttgart, the second one is included on the BiROS satellite from DLR [9].

2.5.1. OSIRIS for 'Flying Laptop'

The OSIRIS terminal for the 'Flying Laptop' satellite is the simplest version of OSIRIS. It consists of two downlink lasers with no uplink capability. The primary laser can achieve a datarate of $200Mb/s$ at $1W$ optical power, for a total module power of $26W$ and mass of 1.3kg. Pointing of the laser beams is done by body pointing of the complete satellite. [9]

2.5.2. OSIRIS for BiROS

The OSIRIS terminal for the BiROS satellite is a more advanced version of OSIRIS that features an uplink channel that is also used for measuring the incidence angle of the received light for fine pointing the satellite. Pointing of the downlink laser beams is done by body pointing of the complete satellite [9]. For redundancy and for experimental reasons, the OSIRIS terminal for BiROS contains two laser sources and two collimators. The laser sources are a High Power Laser Diode (HPLD) and an Erbium Doped Fiber Amplifier (EDFA)-based laser. The HPLD has a lower optical power output and thus has a lower maximum datarate than the EDFA laser, but also consumes less power and might be more radiation tolerant. The EDFA-based laser has a higher optical output power and maximum datarate, higher power requirement and a lower projected lifetime in space. These laser sources are cross-coupled to two collimators: the first has a divergence angle of $1.2mrad$, which allows an optical link to be maintained without the closed-loop control provided by the uplink channel, but also lowers the maximum achievable datarate. The second collimator has a divergence of $0.2mrad$, which is sufficient when the uplink channel is used for fine pointing. Thermal- and vibration testing showed that no significant misalignment errors between the optical axes in the OSIRIS terminal should occur during launch and during operation in space, so no calibration procedure will be necessary in orbit [10].

The optical part of the OSIRIS for BiROS module is illustrated in Figure 4. The alignment cube that is utilised in the alignment of the several optical axes in this system is also visible. The laser sources and electronics are placed elsewhere in the satellite, light from the laser sources is brought to the optical bench through optical fibers.

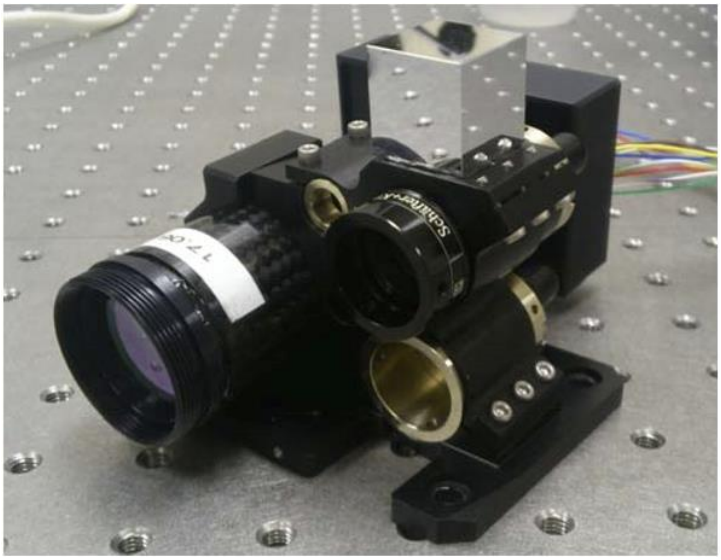

Figure 4: OSIRIS for BiROS optical bench [10].

2.6. NODE

The Nanosatellite Optical Downlink Experiment (NODE) is a research project from MIT. Information on this project is taken from [11]. The goal of this project is similar to this project: to develop a lasercom terminal for CubeSat applications. The fine-pointing of the downlink laser beam is performed by a MEMS fine-steering mirror, light from a beacon laser on the ground station is used to improve pointing accuracy. An overview of the NODE module is given in Figure 5.

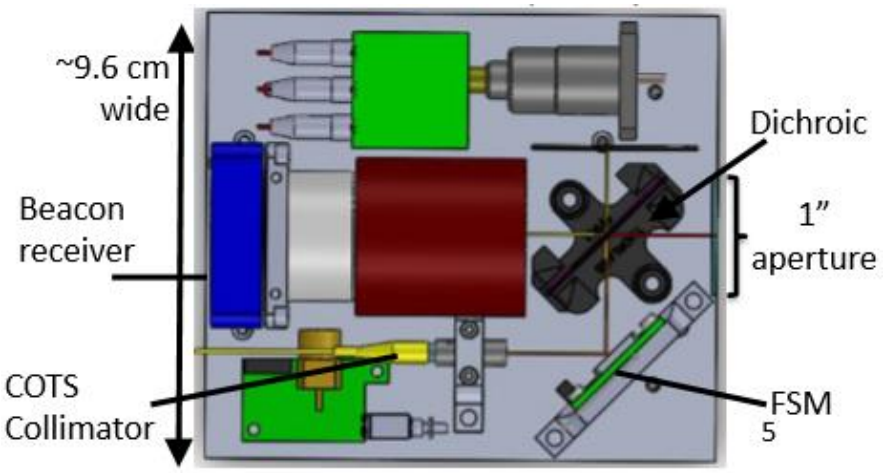

Figure 5: NODE space terminal schematic overview [11].

2.7. Sinclair Interplanetary

At the time of writing, the only published commercially developed lasercom terminal for CubeSats is the one developed by Sinclair Interplanetary. Information on this terminal is taken from [12]. This terminal consists of a downlink channel only, with a startracker and MEMS

gyroscopes included in the terminal for attitude determination. Pointing of the downlink laser beam is performed by a MEMS fine steering mirror (FSM). Closed-loop control of the FSM is performed by a secondary laser and a camera sensor that determines the pointing angle of the mirror.

The laser source for the downlink consists of a seed laser that is modulated with the data stream and a semiconductor optical amplifier, a Tapered Power Amplifier (TPA). This TPA is reported to have a significantly better efficiency than more commonly used fiber-based optical amplifiers. As a result, the projected performance of this module is $1W$ of optical output power at $10W$ total power consumption for the laser source and pointing mechanism combined. A schematic overview of this terminal is given in Figure 6.

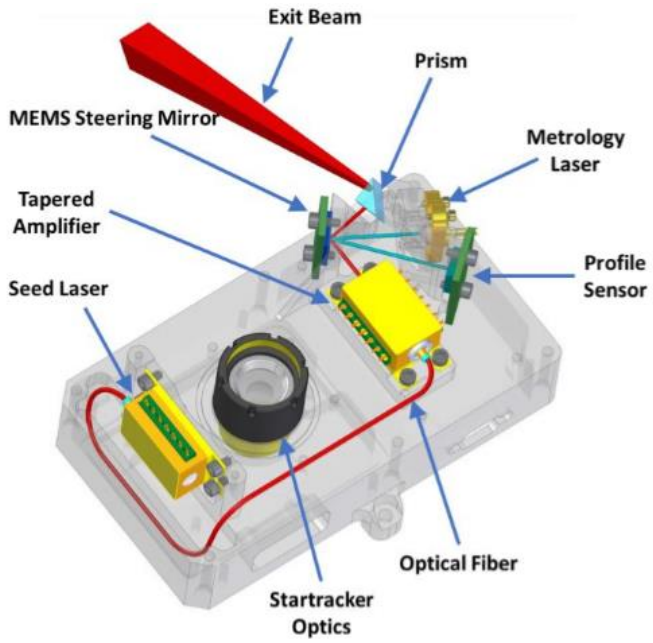

Figure 6: Sinclair Interplanetary lasercom terminal schematic overview [12].

2.8. Existing lasercom systems overview

The design specifications of the previously discussed existing lasercom systems are summarised in Table 1. In this table all known specifications for each system are collected. This information is taken from [2], [7], [11], [5], [6], [3], [9], [10], [11] and [12].

Table 1: Existing lasercom systems specifications overview

	NFIRE	SOTA ch. 1	SOTA ch. 4	VSOTA ch. 1	VSOTA ch. 2	Aerocube OCSD	OSIRIS BiROS	OSIRIS fl. laptop	MIT NODE	Sinclair interplanetary
Wavelength downlink	1064 nm	976 nm	1549 nm	980 nm	1540 nm	1064 nm	1550 nm		1550 nm	785 nm
Optical power downlink	0.7 W	200 mW	35 mW	540 mW	80 mW	5W	0.5W	1W	0.2W	1W
Datarate downlink	5.6 Gbps	1 Mbps	1 Mbps	10 Mbps	10 Mbps	5 Mbps	1 Gbps	200 Mbps	100 Mbps	1 Gbps
Downlink modulation	BPSK	OOK	OOK	NRZ OOK	NRZ OOK	OOK	IM/DD		16-PPM	OOK
Divergence down			223 μrad	3.3 $mrad$	1.2 $mrad$	5.2 $mrad$	200 μrad		1.3 $mrad$	0.17x1 $mrad$
Link distance		1000 km	1000 km	2000 km	2000 km	900 km				1000 km
Ground aperture	6.5 cm	1m	1m	1.5 m	1.5 m	30cm	60 cm		1 m	0.56 m
Pointing capability				1.7 $mrad$	0.7 $mrad$	350 μrad			350 μrad	
Photons/bit downlink						740				1000
Wavelength uplink	1064 nm	1064 nm	1064 nm	-	-	1550 nm	1560 nm	-	976 nm	-
Optical power uplink				-	-	10W		-	10 W	-
Datarate uplink	5.6 Gbps			-	-	10 kbps	1 Mbps	-		-
Divergence uplink				-	-			-	1 $mrad$	-
Uplink aperture	12.4 cm	45mm	45mm	-	-	18 mm		-	25.4 mm	-
Beacon angle accuracy (3σ)		50 μrad	50 μrad	-	-	350 μrad		-	98 μrad	-
Peak power	120 W	15.7W	12.6W	10 W	10 W	60 W	37W	26W	15 W	10W

3 lasercom system sizing

To achieve the goal of this work, proving that an optical communication terminal can be constructed which fits in the CubeSat formfactor and that is a commercially viable alternative to radio-based solutions, the first step is to size the complete lasercom system. In Figure 7 a basic overview is given of a bidirectional lasercom system, consisting of a lasercom satellite terminal within a CubeSat with an uplink receiver, a downlink transmitter and control electronics, and a ground station with a downlink receiver, an uplink transmitter and control electronics.

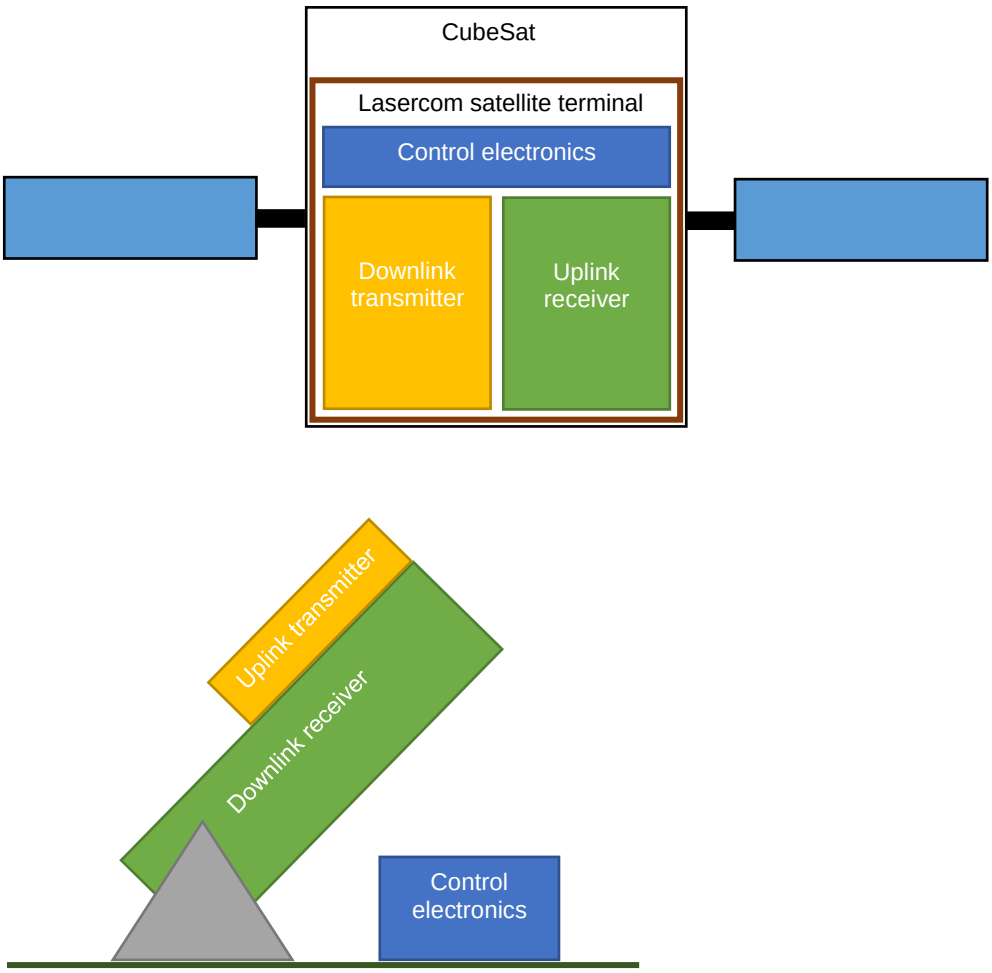

Figure 7: Lasercom basic system overview

To size this system, and to create a baseline design, first the requirements on the lasercom system must be established. This consists of the functional- and top-level requirements as established by Hyperion Technologies based on market situation and demand, and of the derived requirements that can be deduced from the functional- and top-level requirements. Based on these requirements a functional breakdown for the satellite terminal will be created, from which design options for each function can be established and one of these options will be selected for each functionality. With a design solution selected for each required functionality, a first-order sizing model for the lasercom system is constructed, based on which an optimal design for the lasercom system will be established that fits in the CubeSat formfactor, and is a commercially viable alternative to radio-based solutions.

3.1. System functional requirements

As a starting point for the analysis and the sizing of the CubeSat lasercom system, the initial functional requirements are used. These requirements are determined by Hyperion Technologies from the current market demand and competitive situation amongst other lasercom systems or alternative communication payloads for CubeSats, and describe the required functionality of the lasercom system. The lasercom system functional requirements are summed up in Table 2.

Table 2: CubeSat lasercom system functional requirements

Req. nr.	Description	Value	Unit
FR1	Amount of data transferred down per pass	≥100	$Gbit$
FR2	Amount of data transferred up per pass	≥20	$Mbit$
FR3	Amount of data buffered on the lasercom module	≥200	$Gbit$

Requirements FR1 and FR2 describe the amount of data that should be transferred by the lasercom system per pass over a ground station. The required data volume over the uplink per pass is significantly smaller than the required amount of data over the downlink, since the uplink is only expected to carry operational commands and configuration files. The data volume of 20 Mbit per pass does however also allow for relatively quick transfer of software files to update the software of parts of the CubeSat in orbit if necessary.

To relieve the satellite bus, a local buffer storage in the lasercom module must be present. In this way data can be transferred at high speed during up- and downlink communication, while the data that must be transmitted down from the satellite can be sent over the CubeSat bus at a much lower speed, spread out over a longer period of time. The amount of data that must be buffered is described by requirement FR3.

3.2. System top-level requirements

Next to the required functionality of the lasercom system, some initial constraints are put on its design. Since the lasercom system will be sold commercially, the goal of these requirements is to make sure that the final lasercom system can be easily integrated in a broad range of conventional CubeSat designs, to make the lasercom system an attractive design option. These requirements are determined by Hyperion Technologies B.V. to attractively place the lasercom system next to other lasercom and RF communication payloads in the market. The lasercom system top-level requirements are given in Table 3.

Table 3: CubeSat lasercom system top-level requirements

Req. nr.	Description	Value	Unit
TR1	Target peak power consumption, communicating mode	≤10	W
TR2	Buffering mode power consumption (receiving data at $20Mb/s$)	≤0.5	W
TR3	Outer dimensions of lasercom module	≤10x10x10	cm
TR4	Mass of the lasercom satellite terminal	≤1.5	kg
TR5	Production cost of lasercom module	≤50,000	€
TR6	Min. supported orbital height	≤300	km
TR7	Max. supported orbital height	≥800	km
TR8	Min. operational satellite terminal temperature	≤253	K
TR9	Max. operation satellite terminal temperature	≥313	K

Requirements TR1 and TR2 describe the maximum total power consumption of the lasercom terminal during bidirectional communication, TR1, and during idle operation, TR2. During idle operation the lasercom terminal receives data from the satellite bus that is buffered in the lasercom terminal, to enable fast data transfer during communicating mode. The value mentioned in requirement TR2 assumes that data is transferred over the satellite bus at $20Mb/s$, which is the average datarate if $100Gbit$ is transferred to the lasercom terminal in an orbit of 90 minutes.

Requirements TR3 and TR4 describe the guidelines for the size and mass of a 1U CubeSat module. For now a 1U form factor for the lasercom terminal is assumed, but this value is more of a commercial limitation than a technical limitation. There is no severe technical limitation that prevents the lasercom terminal from being larger, the main drawback of this would be that it would be more costly for a customer to integrate the lasercom terminal in their CubeSat. Conversely, a smaller form factor makes the lasercom terminal a more economical solution. Together with requirement TR5, this influences the total cost of the lasercom terminal to the customer.

Requirements TR6 and TR7 define the orbital heights for which the lasercom system will be designed. The lasercom system must support a broad range of CubeSat missions, preferably all mostly used orbits must be supported by the lasercom system to address the largest potential market for this system. The orbital height determines amongst others what maximum link distance has to be chosen to achieve a practical link time per ground station pass.

Requirements TR8 and TR9 give the allowed operational temperatures of the lasercom satellite terminal. A larger allowed operation temperature range eases the thermal of the host satellite, but increases the complexity of the lasercom satellite terminal design. As a reference for the allowed temperature range the Hyperion ST200 star tracker is used, since this component also contains both optics and electronics. The temperature range for this component is specified to be $-20℃$ to $40℃$, which is assumed to be a reasonable constraint on the host satellite.

A further ‘soft’ requirement is that it should be relatively easy to make changes to the lasercom terminal performance characteristics. Even when off-the-shelf CubeSat components are used, it is common for CubeSat developers to request, often small, modifications to these components to better fit their application. In the case of the lasercom terminal, this could exist of for example lowering the downlink data rate to reduce the peak power consumption during communicating mode. During the design process it is therefore worthwhile to find points where simple modifications to the design could be made to adjust the specifications of the lasercom terminal.

3.3. System derived requirements

From the lasercom system requirements laid out in Table 2 and Table 3 further design requirements can be derived. An important specification of a lasercom system is its datarate. While the fundamental functional requirement on a communications subsystem of a CubeSat is the amount of data it can transfer per orbit or per ground station pass, the specification in which customers will be most interested is the maximum datarate. From a commercial perspective, the data transferred per orbit or per ground station pass might not be the best metric of comparison between different communications subsystems. The total time it takes to transfer this data determines how long the customer must suspend its payload operations and also determines how many satellites one ground station can serve per unit of time. By looking at the maximum data rate, the customer can make a more complete trade-off between different communication subsystems. Next to this, there is also a marketing incentive for a high datarate, to place a product competitively compared to competitor communications subsystems.

Given that a satellite will rarely pass straight over a ground station and that some time will be required to establish a communication link, the total time required to transfer the data mentioned in requirement FR1 should be chosen conservatively. Next to this, as described in chapter 2, the most comparable competitor system from Sinclair Interplanetary aims at a data rate of $1\ Gb/s$. This gives a marketing incentive to achieve a similar data rate.

Assuming a data transfer time of 100 seconds per ground station pass, the data mentioned in requirement FR1 should be transferred at a rate of $1Gb/s$. Considering the same transfer time, the uplink data should be transferred at a rate of $200kb/s$. These values are summarised in Table 4.

Table 4: CubeSat lasercom system derived requirements

Req. nr.	Description	Value	Unit
DR1	Downlink data rate	≥1000	Mb/s
DR2	Uplink data rate	≥0.2	Mb/s

3.4. Satellite terminal functional breakdown

The functional requirements on the lasercom system describe the top-level functionality that the lasercom satellite terminal must perform. These functions can be further broken down to aid the selection of design solutions for each required functionality of the lasercom system. The functional breakdown structure (FBS) for the lasercom satellite terminal is given in Figure 8.

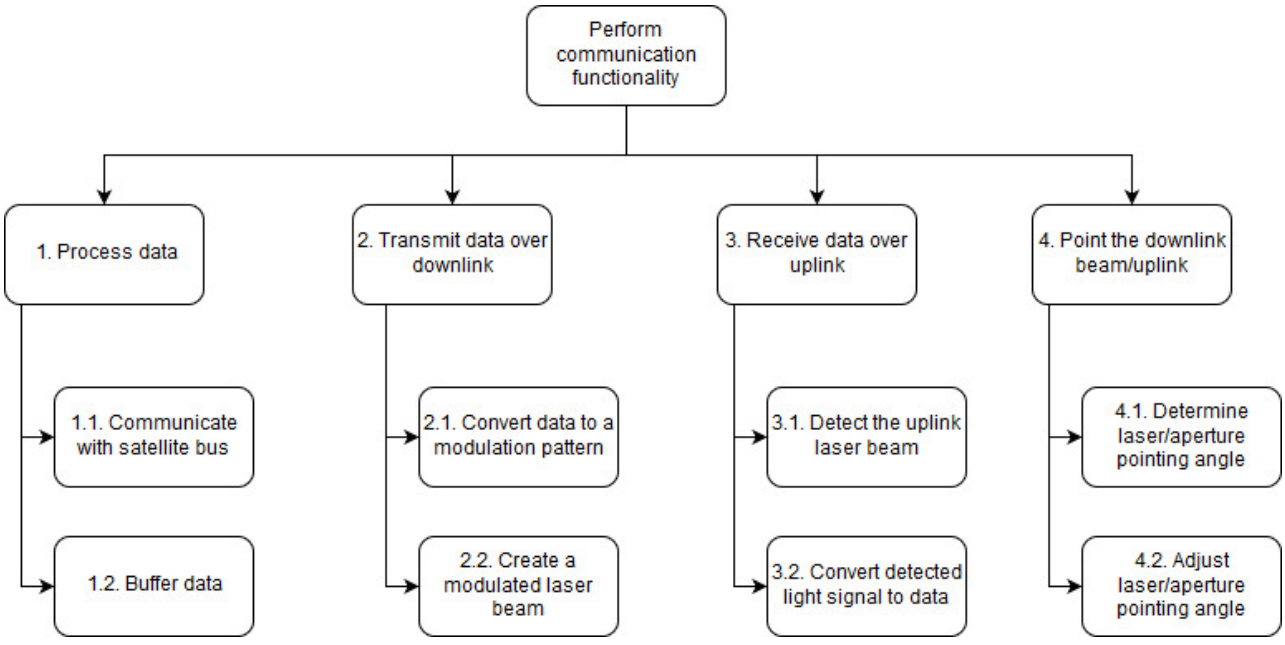

Figure 8: lasercom satellite terminal functional breakdown structure

While technically an FBS diagram must be valid regardless of the technical solution that is selected for any required functionality, in the FBS of Figure 8 it is already assumed that laser beams will be used as the medium over which the down- and uplink data is sent, as this is an implicit requirement for this project.

From the functional requirement that data must be buffered by the lasercom satellite terminal (FR3) function 1 follows, the processing of data by the lasercom terminal. This data processing

will consist of communicating with the satellite bus (1.1.) and buffering data before it is transmitted over the downlink or received from the uplink (1.2.).

From the requirement that data must be transmitted down by the lasercom terminal (FR1) function 2 follows. The first step in the process of sending data down is to convert the data that must be sent down in to a modulation pattern that contains this information (2.1.). The signal carrier, in this case a laser beam, is then modulated using this modulation pattern (2.2.).

Similarly, the requirement that data must be received from an uplink (FR2) implies that the light from the uplink laser beam must be detected by the lasercom terminal (3.1.). Since this modulated light contains the uplink data, the detected light signal must then be converted to the actual data (3.2.).

The last required functionality from the lasercom terminal is the ability to point the downlink laser beam and the uplink receiving aperture, function 4. To be able to do this, the lasercom terminal must first in some way determine the pointing angle of the laser beam and the aperture (4.1.). With this information, some form of actuation must be driven that adjusts the pointing angle of the downlink laser and the uplink aperture.

3.5. lasercom satellite terminal design options

The functional breakdown structure from Figure 8 contains all the functionality that the lasercom satellite terminal must be able to perform. For each required function, different technical solutions can be chosen that are capable of providing this functionality. To be able to select the best design solution for each function, a design options tree (DOT) is created for each function that contains all realistically possible design solutions for that function. For each DOT the different design options are discussed in order to rule out less favourable solutions.

3.5.1. Function 1.1, communicate with satellite bus design options tree

The lasercom terminal must communicate with the satellite bus to manage operations of the lasercom terminal, to for example initiate a communication pass over a ground station, and to communicate telemetry information and operating information to the on-board computer for housekeeping purposes. Next to this, the data that must be sent down and is received over the uplink should also be transferred over the satellite bus. The amount of data that is transferred over the satellite bus for housekeeping and to manage operations is limited and is, for CubeSat components, commonly transferred over an I^2C bus. Looking however at the amount of data that must be sent down during each pass, requirement FR1, the bus interface over which this data is sent to the lasercom terminal must still allow for a fast datarate. This data is generated during the course of one orbit, so assuming a reference orbital period of 90 minutes, this results in an average data rate over the satellite bus of $20Mb/s$. This already rules out many conventional CubeSat bus communication interfaces.

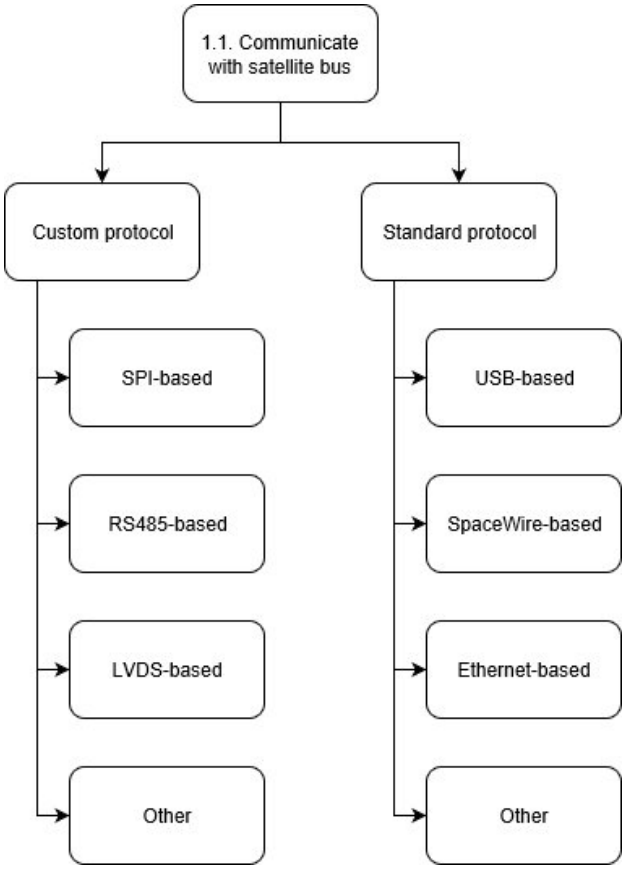

Figure 9: function 1.1, communicate with satellite bus design options tree

Some remaining suitable bus interfaces are illustrated in Figure 9 and can be subdivided in two categories, an interface using a custom protocol and an interface using a standard protocol. A custom protocol bus would consist of a standard interface type that is capable of transferring data at the required rate, such as SPI, RS485 or some form of LVDS. A custom protocol is then defined on how data should be transferred over this interface from the satellite bus to the lasercom terminal. With a standard physical interface a complete standardised interface is used, such as USB, SpaceWire or Ethernet. These standards describe both the electrical interface of an interface, as well as a multitude of protocols on how devices connected to this bus should communicate and transfer data between each other.

An advantage of a standardised electrical interface with a custom communication protocol is that this protocol can be tailored just for the lasercom terminal. In this way data can be transferred in the most efficient way, with a low protocol overhead and thus lower power consumption for this interface. The main disadvantage is that this custom protocol must be implemented in the firmware of the devices that are connected to it. This is not only a development step for the lasercom terminal, but also for each customer that wants to implement the lasercom terminal in their CubeSat. A custom protocol therefore increases the total costs of making a satellite with lasercom for the customer and increases the development time of such a satellite. Next to this, because of the fast datarate required on the satellite bus, it might prove difficult for the customer to implement this custom protocol on his own OBC or payload processor in a way that is capable of attaining the required datarate.

Using a standardised protocol on the other hand adds additional communication overhead to comply with the standard protocol, so the total power consumption involved in the bus interface is higher than with a custom protocol. Advantages of using a standard protocol are that many COTS embedded processors and controllers contain supporting hardware and have software libraries available for many standard interfaces, such as USB and Ethernet. The Hyperion OBC for example contains multiple USB interfaces. By making use of this COTS support for

standard protocols, the total cost of integrating the lasercom terminal in a CubeSat for a customer are lowered, the development time is shortened and the achievable data rate and power consumption are known accurately beforehand.

The additional power consumption for using a standard protocol is expected to be limited, and might actually be cancelled out by utilising the power-efficient hardware modules that are integrated in COTS embedded processors for these protocols. This, next to the reduced development effort required from the customer make a standard interface the preferred solution. From the three standards mentioned in Figure 9, Ethernet has the highest achievable data rate. This comes however at the cost of a higher power consumption and additional electronic complexity. Since this higher datarate is not necessary for the lasercom terminal, Ethernet is not the ideal choice. SpaceWire has reliability features that make it especially suitable for use in space applications, but COTS embedded processors do not contain hardware modules that support SpaceWire. SpaceWire is also uncommon in CubeSat satellites, making SpaceWire a less favourable choice. USB on the other hand seems to have an optimal set of specifications: it is a widely used bus with support built in in many COTS devices. The maximum datarate of USB of $480Mb/s$ is sufficient for the lasercom terminal and leaves some margin. Electrically, USB is relatively simple and energy efficient. From the design options mentioned in Figure 9, after removing all unfeasible and less favourable design options a USB-based solution remains as the most promising option.

3.5.2. Function 1.2, buffer data design options tree

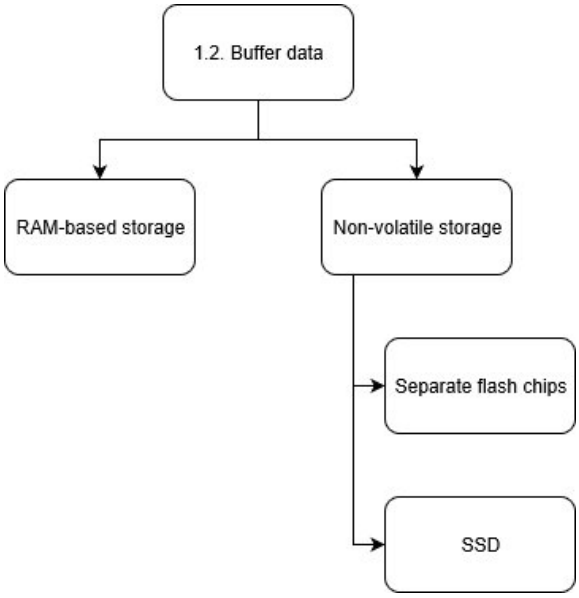

Figure 10: function 1.2, buffer data design options tree

Because of the large amount of data that must be sent down by the lasercom system during each pass, a local data storage must be included on the lasercom terminal to relieve the satellite bus. The DOT for this local data storage is given in Figure 10. The data buffer must support the same datarate as the downlink and must be capable of storing the complete data volume that must be sent down during a pass. This significantly limits the number of suitable storage technologies. There are, in short, two options for this data buffer: a RAM-based storage solution and a non-volatile storage solution.

For a RAM-based storage, DRAM is the only technology that combines a sufficient storage volume with sufficient speed. An issue with DRAM however is the power consumption. Looking at a reference calculation for DDR3 RAM, the average power consumption for 1 Gb of data storage is $436mW$ [13]. For the required storage volume of 200 Gb from requirement FR3, this would be an excessive power usage. The main focus for a RAM-based storage should

therefore be on reducing the power consumption. The lowest power DRAM-based storage is LPDDR RAM, that has been developed for mobile applications. With each newer generation of DDR RAM the power usage is decreased, so it is beneficial to select a recent LPDDR family. Using a calculation tool from a memory manufacturer, [14], it is calculated that at an average reading speed of 2Gbps an LPDDR3-based storage will consume $120mW$ per 16Gb. During an average writing speed of $30Mb/s$ the power consumption will be around $25mW$ per 16Gb LPDDR3 chip, and during completely idle operation the power consumption is $20mW$ per 16Gb chip. These values could be acceptable for the lasercom terminal. It is assumed that with LPDDR4 memory, these power consumptions will be even lower.

For a non-volatile storage solution, the required data volume and required read speeds strongly limit the suitable types of memory. Looking at the required buffer size for requirement FR3, together with the maximum read speed form requirement DR1, only SSD-based storage solutions are a feasible flash-based storage solution. While the maximum power consumption for an SSD is large, the idle power consumption is significantly lower than for a RAM-based solution [15], the achievable read- and write speeds and available storage volume are more than sufficient for this application. A great advantage is also that an SSD is a cheap, standardised component where little development effort is necessary to perform the required functionality. An unknown factor is the radiation tolerance of commercially available SSD drives.

Given that an SSD-based storage solution is a cheap, simple to develop solution with a lower power consumption for the storage volume and maximum datarate required for the lasercom system than a RAM-based solution, while also offering a significant margin in both maximum read speed and available storage volume, makes an SSD flash-based storage the most favourable design option for the lasercom system from the options mentioned in Figure 10.

3.5.3. Function 2.1, convert data to a modulation pattern design options tree

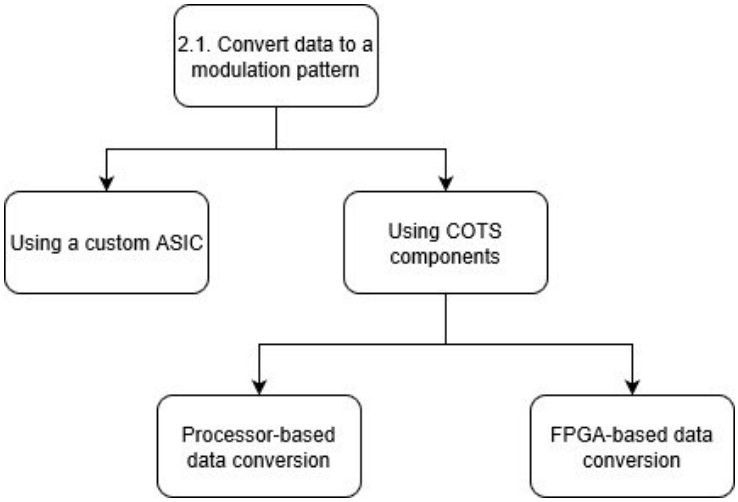

Figure 11: function 2.1, convert data to a modulation pattern design options tree

To transmit the data that is stored in the buffer in the lasercom terminal, it must first be transformed to a modulation pattern that drives the final pattern of the transmitted laser beam. The DOT for this function is given in Figure 11. While it is possible to design a custom ASIC that is capable of doing so at a high datarate with a low power consumption, the time and costs involved in developing a custom ASIC make this an unfavourable option for this application. Using commercially available components this modulation pattern can be generated directly by a processor in the lasercom terminal, which could mean that only a single processor has to be included which can be an energy efficient solution. However, with the required downlink

datarate of $1Gb/s$ from requirement DR1, it becomes impractical and perhaps unrealistic for commonly available embedded processors to perform any real-time manipulation on the downlink data stream to convert it to a modulation pattern. This can be mitigated by manipulating the data before it is stored in the buffer, and thus storing a modulation pattern in the buffer memory. This could however mean that, dependent on the modulation type, more buffer memory is used for the same data.

An FPGA does not have this issue. FPGAs also allow for customised error correction algorithms to be implemented to correct the data that is read from the buffer and to re-apply error correction data to the downlink data stream. Furthermore, FPGAs generally already contain high-speed serializers, where a processor would need an external serializer that converts the modulation pattern to an electrical signal. From the two options mentioned in Figure 11, an FPGA-based data conversion seems the most favourable option.

3.5.4. Function 2.2, create a modulated laser beam design options tree

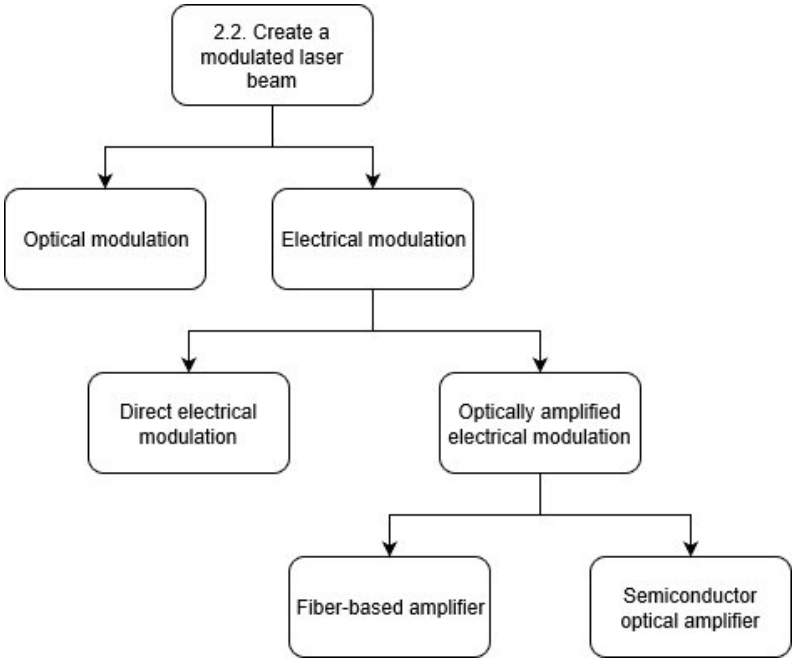

Figure 12: function 2.2, create a modulated laser beam design options tree

A modulated laser beam should be created using the modulation pattern generated from the buffered data,. This modulated beam can be created in two ways as illustrated in Figure 12: by optically modulating the laser beam, or by modulating the laser source electrically. This electrically modulated source can then directly generate the final laser beam, or it can generate a small signal light which is then amplified optically to arrive at a sufficiently strong modulated laser beam.

An optical modulator works by taking a continuous-power laser beam and passing or absorbing it as commanded by the modulation pattern. With direct electrical modulation on the other hand the current that is used to drive the laser source is directly influenced to create a modulated laser beam. The optical output power of a laser diode is directly related to the input drive current, so this is a relatively straightforward way of modulating the output power of a laser. This method induces no additional optical losses and actually reduces the total power consumption, since there is no or minimal current flowing through the laser diode when the laser beam is supposed to be off. A disadvantage of this method however is the fact that a laser diode has a maximum frequency at which its output power can be modulated. This frequency is coupled to the relaxation frequency, which describes the resonant frequency at which the laser output power will fluctuate when a current step is applied as input. Furthermore,

the turn-on delay between the moment a current step input is applied to the laser diode, and the moment that the output power from the laser diode starts to rise, is also dependent on the relaxation frequency [16]. Higher power laser diodes generally have a lower relaxation frequency, which results in a lower maximum modulation frequency. Generally speaking, this limits the use of direct electrical modulation to relatively low optical output powers.

A different architecture uses some form of optical amplification to amplify a weak modulated laser beam. This weak modulated laser beam can be generated preferably by direct electrical modulation of a small laser diode, which is commonly referred to as a seed laser. This allows for a simpler laser driver design and it allows for the laser diode, which has a high relaxation frequency due to its small size, to be modulated at a fast rate. To amplify this weak laser beam, two amplifier types are commonly used: fiber-based amplifiers and semiconductor-based amplifiers.

A fiber-based optical amplifier is made from a special doped fiber. This fiber contains ions that can be excited to a stable higher energy state by a specific wavelength of light. These ions will stay in this higher energy state until they are stimulated by a photon of a different specific wavelength of light, a longer wavelength than the excitation wavelength, after which they will release a photon of the same wavelength as this stimulating photon. The excitation of these ions is achieved by a continuous power laser, the pump laser. If the modulated light from the seed laser is injected in this doped fiber, the output light from this fiber will follow the same modulation profile, but with a larger optical power, thereby achieving optical amplification. A fiber-based optical amplifier is simple in construction and can be scaled easily, by simply making the total doped fiber length longer and by increasing the power from the pump laser. Disadvantages are however that due to the long required fiber length fiber-based amplifiers tend to be physically large. Furthermore, fiber-based optical amplifiers have a few additional sources of losses: the combiner, where light from the pump laser and from the seed laser is combined into the doped fiber introduces losses, the long light path through the doped fiber introduces fiber propagation losses and the fact that each short-wavelength pump photon can only generate at most one longer-wavelength amplified photon. Shorter wavelength photons contain more energy than longer wavelength photons, so this is an inherent energy loss. The combined result from these effects is that the total electrical-to-optical efficiency of a fiber-based optical amplifier is low. A proposed EDFA-based solution from photonics supplier Gooch & Housego requires a total electrical power input of $3.54W$ for an optical output power of $0.2W$[1].

A semiconductor optical amplifier (SOA) works in the same way as a regular laser diode. The main difference is that instead of having a reflective and a semi-reflective element at each end of the gain medium to create a laser cavity, a semiconductor optical amplifier consists of only a semiconductor gain medium. This means that the incoming light only passes the SOA once and is not reflected back and forth internally. The semiconductor gain medium is driven by a constant current source and amplifies the incoming light by stimulated emission, where the incoming light triggers the gain medium to release additional photons [17].

While semiconductor optical amplifiers are a promising technology, no references are known for the radiation tolerance of these devices and their suitability for use in a space environment. EDFA-based solution have been applied in space for a long time and are available from numerous suppliers. Nevertheless, both of these design options are deemed feasible for this lasercom system.

[1] Confidential communication with Gooch & Housego, 9-1-2018

3.5.5. Function 3.1, detect the uplink laser beam design options tree

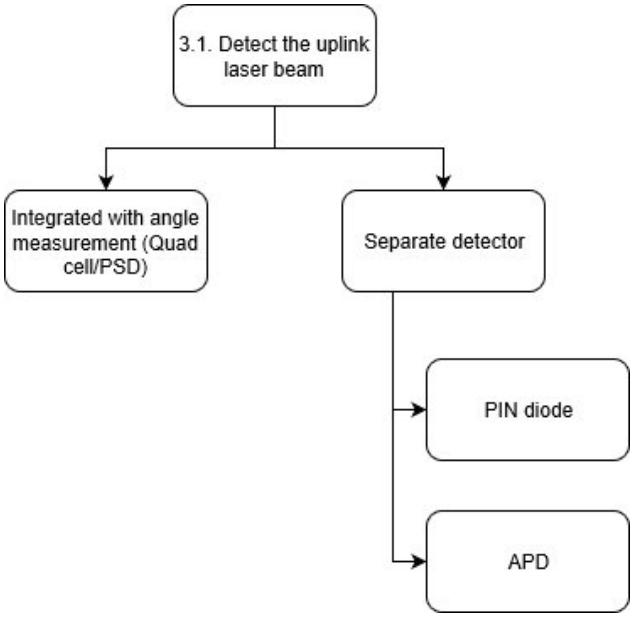

Figure 13: function 3.1, detect the uplink laser beam design options tree

To be able to extract data from the received uplink light, the collected light must be converted to an electrical signal by a detector. The different options for doing this are in essence all based on photodiode detectors, but they are different types of photodetectors with different merits. These options are given in Figure 13. Detecting of the uplink data can be combined with function 4.1, determine the laser/aperture pointing angle, for certain angle measurement solutions. Otherwise a separate detector can be utilised.

If a quad cell photodiode or a position sensitive detector (PSD) is used to measure the laser/aperture pointing angle, then the signals from the X- and Y outputs from these detectors can be summed to create an electrical signal from which the uplink data can be extracted. While this is an efficient solution, as all the collected uplink light can be converted to electrical signals by the same detector, it does imply that some further electrical processing is required to extract both the uplink data and the incoming light angle from the same sensor.

Alternatively, if the uplink light angle of incidence is used to determine the downlink laser and uplink aperture pointing angles, the collected uplink light can also be split in two beams, where one beam will be used for measuring the uplink light angle of incidence and the other beam will be sent to a separate detector that generates an electrical signal corresponding to the uplink light modulation. This separate detector can be a regular PIN photodiode or an avalanche photodiode (APD). An APD is capable of detecting weaker light signals, but also requires more power and is more expensive. A PIN photodiode is cheap and commonly available in different sizes and with different specifications.

From the design options mentioned in Figure 13 no option is clearly less feasible or favourable than the other options, so all mentioned options can be considered acceptable choices for this lasercom system.

3.5.6. Function 3.2, convert detected light signal to data design options tree

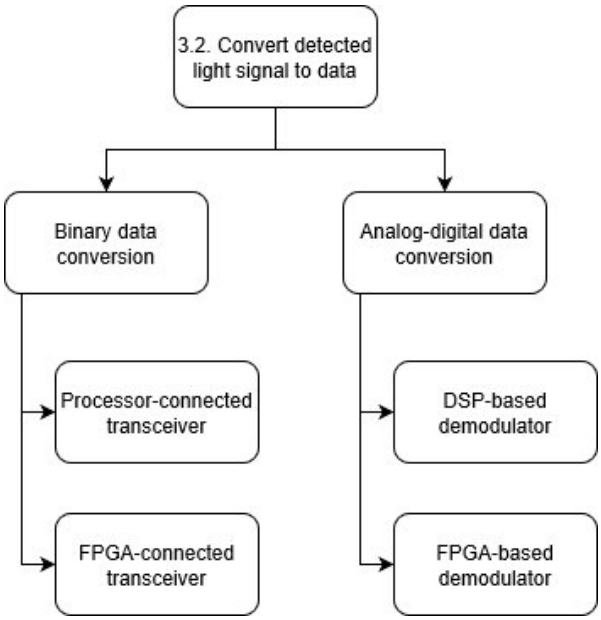

Figure 14: function 3.2, convert detected light signal to data design options tree

From the electrical signal that comes from the uplink detector, the uplink data stream can be extracted. The design solutions that can perform this function are given in Figure 14. This can be done by binary data conversion, where this electrical signal is treated as a stream of ones and zeroes, where a one is defined as uplink light is detected, and a zero is no uplink light is detected. The alternative is converting the detecting detected electrical signal to a digitised version of this electrical signal using an analog to digital converter (ADC), where digital processing on this digitised signal can be used to extract the uplink data stream. While an ADC solution allows for more complex modulation schemes to be used, such as multiple-level amplitude modulation, the energy and processing requirement for an ADC-based data conversion is significantly higher than a binary data conversion. Considering the relatively low required datarate for the uplink from requirement DR2, a binary data conversion is a more efficient and the favourable design option for this lasercom system.

This binary data extraction can be performed either by a binary converter connected to a processor, or by an FPGA connected binary converter. The required uplink datarate is relatively low, so it is possible for the uplink data to be further processed by a processor included in the lasercom terminal. Processing the uplink in an FPGA however offers the advantage that as there already is an FPGA in the lasercom terminal to generate the downlink laser laser modulation pattern, as describe in section 3.5.3, this same FPGA can also process the uplink data and store it in the lasercom terminal buffer storage. These two design options can however both be considered feasible.

3.5.7. Function 4.1, determine laser/ aperture pointing angle design options tree

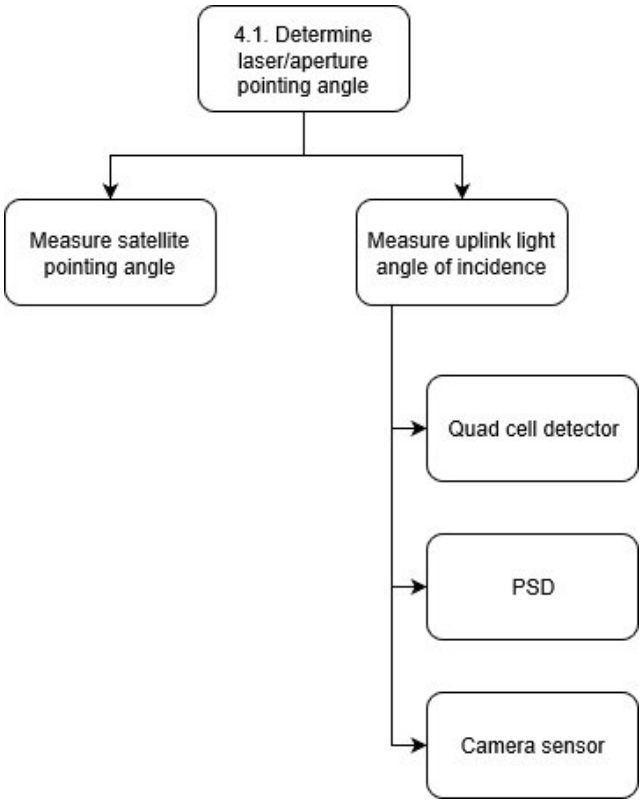

Figure 15: function 4.1, determine laser/aperture pointing angle design options tree

For free-space optical communication it is critical that the downlink laser beam and the uplink receiving aperture are pointed accurately towards the ground terminal. To be able to do this, the actual pointing angle or pointing angle deviation has to be measured. This can be done either by measuring the orientation of the complete satellite, or by measuring the angle of incidence of the uplink light, as illustrated in Figure 15. While measuring the orientation of the complete satellite is a functionality that is already performed by the ADCS, there will be additional errors in this angle determination from thermal and dynamic effects in the satellite. Furthermore, the update rate of the ADCS attitude determination is usually relatively low. It is therefore deemed advantageous to measure the uplink light incidence angle to determine the downlink laser and uplink aperture pointing angles.

The uplink light angle of incidence can be measured accurately by using a quad cell detector, a PSD sensor or a camera sensor. A quad cell consists of a circular photodiode that is divided in four segments. The photocurrent that is generated by each segment can be measured, the difference between these photocurrents then indicates the position of the focussed received light spot on the quad cell, which determines the angle of incidence of this received light. A PSD has a similar working principle, with 4 output currents where the difference between these currents determines the X- and Y position of the projected dot on the sensor, but where on a quad cell the projected dot has to cover all four quadrants to be able to determine the position of this dot and the relation between the current differences between the quadrants and the position of the dot is non-linear, for a PSD there is a linear relation between the current differences and the dot position over the complete sensor area. A quad cell also has an area in between the electrodes where incident light is not converted to current and is thus lost. A PSD does however have drawbacks compared to a quad cell detector. While a quad cell consists of four photodiodes that are essentially isolated from each other, a PSD consists of a photosensitive area and one or two resistive layers. These resistive layers add thermal noise, and connect the four electrodes of the PSD, which implies that the noise on each electrode will

influence the other electrodes as well [18]. PSD sensors are generally also much more expensive than quad cell detectors. Since for the lasercom system it is expected that the collected uplink light power will be very weak, a low-noise angle measurement sensor is deemed more important than a linear angle measurement response, which makes a PSD sensor an unsuitable design option.

A camera sensor can also be used to measure the uplink light angle of incidence, a camera sensor can be considered as a quad cell with significantly more photodetector cells. Because of the greater number of cells a camera sensor does not suffer from reduced accuracy away from the centre of the sensor as a quad cell does, but where a quad cell detector can detect light signals with a high bandwidth, just like regular photodiodes, a camera sensor is limited to a much lower framerate. This implies that with a camera sensor only DC-level light signals can be detected, while with a quad cell an AC-modulated signal can be detected.

Detecting an AC-modulated signal in the uplink receiver has some strong advantages. If a camera sensor is used to directly look at the received light intensity on each pixel, it is impossible to distinguish between light from the uplink beacon, the signal of interest, and background light and offset noise. Especially at low signal light levels, this can be problematic. If however a large-bandwidth detector is used that can handle much faster modulated light signals, it becomes possible to filter out all lower-frequency signals from background light and offset noise to make sure that only the signal of interest is amplified. By looking at the difference in amplitude of this amplified signal for each quadrant of the quad cell detector, the laser/aperture pointing angle can be determined with an improved signal to noise ratio. As described in section 3.5.5, for this lasercom system it is possible to combine the uplink data detection function with the angle measurement function. By modulating the uplink beacon light with the uplink data pattern, the combined system with a quad cell will have a simple method of transferring data over the uplink beacon, while at the same time offering improved accuracy on the determination of the laser/aperture pointing angle. It can thus be concluded that from the options mentioned in Figure 15, the camera sensor and the quad cell detector are the only feasible options, with the quad cell detector being the more favourable solution.

3.5.8. Function 4.2, adjust laser/aperture pointing angle design options tree

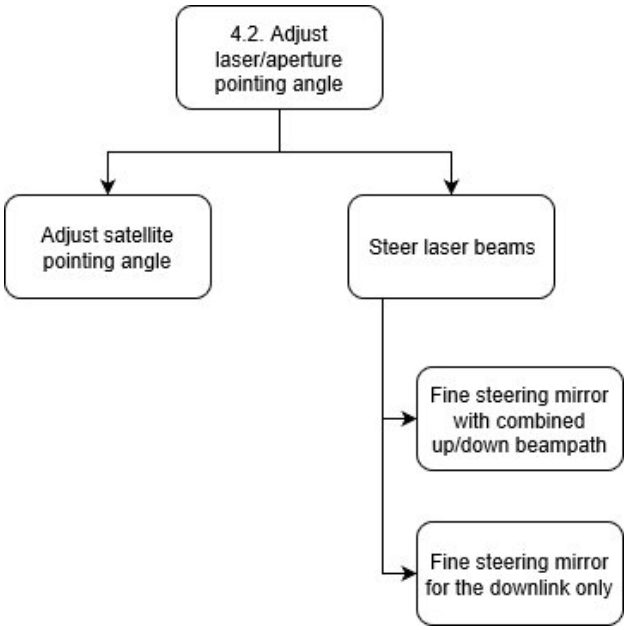

Figure 16: function 4.2, adjust laser/aperture pointing angle design options tree

To establish and maintain a communication link between the satellite and the ground station, the downlink laser beam and the uplink receiving aperture must be pointed towards the ground terminal. In general this can be done in two ways, as illustrated in Figure 16: by adjusting the pointing angle of the complete satellite, the so called 'body pointing' option, or by steering the up- and downlink laser beams independently from the rest of the satellite.

Adjusting the pointing angle of the complete satellite is the cheapest and simplest option to adjust the pointing angle of the laser beams. With this option all optical components can be mounted rigidly to the body of the satellite, and adjusting its own pointing angle is a functionality that almost all satellites already have. This is commonly done by the attitude determination and control system (ADCS). A disadvantage of using body pointing is that the laser beams cannot be pointed independently from the rest of the satellite. This will likely imply that while a lasercom communication link is active, the satellite will not be able to operate its payload as payloads often have to be pointed by body pointing as well.

By pointing the up- and downlink laser beams only instead of the satellite body, the lasercom satellite terminal becomes independent of the rest of the satellite for its pointing requirements. This allows the lasercom terminal to become more modular and allows the satellite to perform a different operation that requires body pointing while a lasercom communication link is active, as long as the angular range of the steering mechanism is sufficient. Fine steering mirrors can also be made highly accurate, an example is a fine steering mirror from TNO that has a jitter figure of $1\ \mu rad$ [19]. Major disadvantages of steering the laser beams with fine steering mirrors are their additional power consumption, size, mass, complexity and cost.

While there are significant differences between using body pointing and using a fine steering mirror, both of these design options can be considered feasible for this lasercom system.

3.6. Lasercom system modelling

To be able to optimise the design for the lasercom system, a model must first be made of the lasercom system to be able to predict the performance of a proposed design and to be able to predict whether a proposed design is capable of meeting the established requirements. Since the complexity of the lasercom system is limited compared to, for example, a complete aircraft or spacecraft, a first-order modelling method will be utilised. For this method first an overview is given of the selected design solutions for the lasercom satellite terminal along with a schematic overview of this satellite terminal, after which the relevant design variables are identified that together describe and constrain the complete design of the lasercom terminal, and with which a sufficiently accurate prediction of the final system performance can be performed. Based on these variables an analytical or computational model is made that captures all relevant physical effects and error sources, and uses these to make a prediction of the final lasercom system performance.

3.6.1. Lasercom satellite terminal selected design options

In section 3.5 an analysis is made of which design solutions are feasible for each required functionality of this lasercom system. While for most functionalities one most favourable or only one feasible design option is identified, for some functionalities more than one option remains.

To create a modulated laser beam, two feasible design solutions are identified: using a fiber-based amplifier and using a semiconductor optical amplifier. While semiconductor optical amplifiers are a promising technology, no references are known for the radiation tolerance of these devices and their suitability for use in a space environment. EDFA-based solutions have been applied in space for a long time and are available from numerous suppliers. Since the downlink source is such an important part of the lasercom satellite terminal, it is decided to

reduce the development risks by implementing an EDFA-based laser source for this lasercom system.

To detect the uplink laser beam and convert it into an electrical signal several design options are identified, by integrating this function with the angle measurement sensor or by using a separate PIN or APD detector. Since the collected light power from the uplink will likely be weak and since the required uplink data rate from requirement DR2 is not too high, it is deemed most efficient to integrate the detection of the uplink laser beam with an angle measurement sensor. At the required data rate electronic processing of the resulting electrical signals is still relatively straightforward and in this way the maximum amount of collected uplink light is converted to an electrical signal, while still taking advantage of the increased pointing accuracy from measuring the uplink light angle of incidence, as described in section 3.5.7.

For adjusting the downlink laser and uplink aperture pointing angles two feasible design options are identified, using body pointing of the complete satellite or using a fine steering mirror in the lasercom satellite terminal. While using a fine steering mirror could offer a superior pointing accuracy over satellite body pointing, it comes at a significant cost in other aspects. If body pointing offers sufficient pointing accuracy, it could enable a more optimal and more commercially viable system design than a system based on fine steering mirrors. The ADCS system from Hyperion is known to offer a jitter performance of approximately $10\ \mu rad^2$. While this is not as good as the performance of a fine steering mirror, the reference lasercom systems from Table 1 use downlink laser beam divergence angles that are much larger than this value. This leaves enough margin to be able to assume that the pointing angle adjustment performance of a body pointing method using the satellite ADCS will be sufficient to support the requirements of the lasercom system. This design option is therefore selected.

3.6.2. Lasercom satellite terminal block diagram

Using the selected design options from section 3.5 a block diagram can be drawn for the satellite terminal of the lasercom system to clarify the system design and to aid in the description of the lasercom system model. The satellite terminal block diagram is given in Figure 17.

[2] Internal, unpublished test results from Hyperion Technologies B.V.

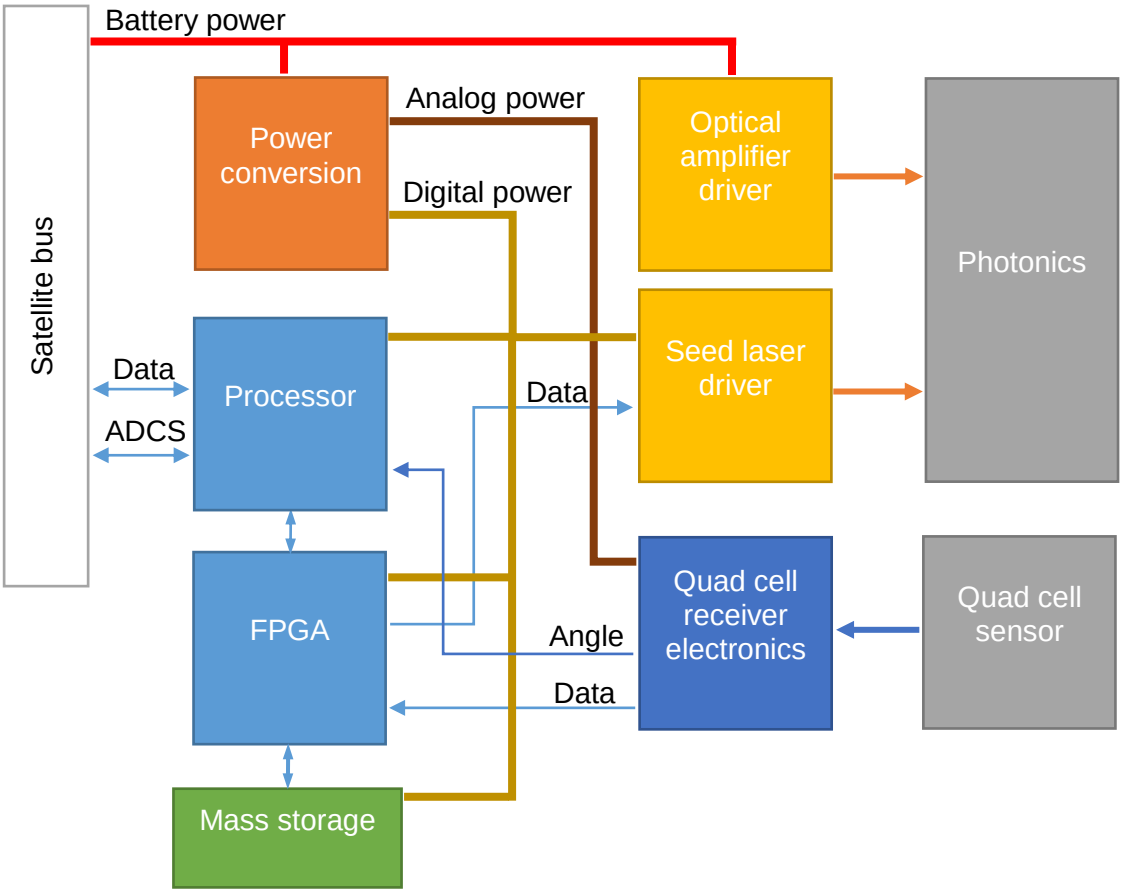

Figure 17: Lasercom satellite terminal block diagram

The satellite battery power is converted for the electronics in the lasercom terminal. Since the analog electronics have more stringent requirements on the noise level of their supply voltages, the analog power lines are indicated separate from the digital power lines. The optical amplifier driver should be powered directly from the satellite bus battery power to reduce power conversion losses, as discussed in section 4.5.

Communication with the satellite bus can be performed best by an on-board processor, as discussed in section 3.5.1. This processor will handle the data transfer between the lasercom terminal and the satellite bus for both the up- and the downlink. Next to this, the angle measurements from the quad cell receiver electronics are also passed along to the satellite ADCS by this processor. The FPGA will handle the buffering of data from the satellite that should be sent down during the next communication link, and the buffering of received data from the uplink. The buffered downlink data will be sent to the seed laser driver at a high rate when the communication link is active. Most, if not all error correction functionality on the buffered and received data will be handled by the FPGA as well in order to achieve a maximum throughput speed of this error correction mechanism.

As described in section 3.5.4, to create the modulated downlink laser light a setup will be used consisting of an electrically modulated, low-power seed laser and an optical amplifier, which increases the power of the optical signal from the seed using optical amplification. The seed laser and the optical amplifier are included in the Photonics block.

3.6.3. Lasercom system design variables identification

The architecture of the lasercom system has been established in sections 3.5 and 3.6.2. The detailed design of this architecture can be captured by a set of design variables, which together constrain this design. In this chapter, for each component of the lasercom system an argumentation is given for which set of design variables best captures the characteristics of this component. A summary of these variables and their symbols is given in Table 5.

CubeSat mission characteristics

The CubeSat mission characteristics are the specifications of the host CubeSat that will contain the lasercom terminal. Some of the characteristics of the envisioned host CubeSat missions influence the sizing of the lasercom system, the lasercom system should thus be sized such that it will fit in the broadest range of expected CubeSat missions. The most important mission characteristic is the orbital altitude, as this determines the satellite velocity and maximum link distance. The minimum and maximum satellite mass also play a role, as they determine the minimum and maximum moment of inertia of the satellite which determines with what factor torque from the reaction wheels in the ADCS is transformed in to rotational motion of the satellite.

Ground station receiver

The downlink receiver section of the ground station captures the downlink optical signal from the lasercom terminal, converts it to an electrical signal using a detector and extracts the transmitted data from this signal. The amount of light that is converted by the detector depends on the ground station aperture size and the optical losses in the ground station between the aperture and the detector. The performance of the detector and the signal interpretation in the ground station can be captured by a single variable, the number of photons that the ground station needs to capture per bit of information. This variable contains all noise in the detector and electronic circuitry of the ground station, without diving in to further detail of the specific implementation of this functionality. This number can also be easily compared between different optical receiver solutions.

Ground station beacon transmitter

The beacon transmitter on the ground station transmits the laser beam with which the satellite lasercom terminal can measure its pointing error. This beacon light is also modulated to serve as an uplink channel. Relevant design parameters for this transmitter are the transmitted optical power and the wavelength at which the beacon transmits. An effect that is related to the beacon transmitter is the angular error in the beacon light path due to atmospheric distortion. This distortion takes place mostly in the lower layers of the atmosphere due to their higher density, so while for the downlink light this has a negligible impact on the pointing angle of the laser light and thus on the location where the downlink light will arrive, for the uplink laser light there is a long propagation distance above these lower atmospheric layers, and any atmospheric angular deviation in the uplink beacon light can thus be directly added to the pointing error of the ground station. This angular error caused by the atmosphere can be described by a statistical distribution. It can therefore be considered a design variable, a larger design atmospheric angular error gives a higher reliability to the pointing of the lasercom system, at the cost of increased complexity or power consumption at a different place in the design. Since the beacon beam divergence will be quite wide, as will be described in section 3.7.5, and since it will be relatively straightforward to align the optical axes of the beacon transmitter and downlink receiver on the ground station, it is assumed that a misalignment between the beacon transmitter and the downlink receiver will be insignificant.

Ground station pointing mechanism

The pointing mechanism on the ground station predicts where the satellite is using its ephemeris data and points the ground station telescope accordingly. Once a link has been established, it is expected that the ground station will be able to correct its pointing angle using the angle of incidence of the downlink laser light from the CubeSat terminal. Relevant design variables for the ground station pointing mechanism are therefore the satellite orbital position prediction error, the closed-loop pointing error of the ground station once a link has been established and the minimum elevation angle of the satellite above the horizon before the ground station is capable of tracking it. This variable has an influence on the mechanical design of the ground station, but also on its optical design, to be able to deal with the stronger atmospheric distortions at lower elevation angles. On the other hand, a ground station with a lower minimum elevation allows for longer total link durations.

CubeSat ADCS characteristics

Since it is chosen in section 3.5.8 to use body pointing for the CubeSat lasercom terminal, the CubeSat ADCS plays an important role. Therefore, constraints have to be put on the performance of this ADCS. Using these constraints, the customer is then free to select any ADCS for use in their CubeSat that meets these requirements. For the initial pointing of the lasercom terminal before a link is established the ADCS must determine the CubeSat orbital position and attitude. The errors in this determination determine the open-loop pointing error of the CubeSat lasercom terminal. Once a link has been established, the ADCS can use information from the quad cell sensor to determine its pointing error to the ground station with much greater accuracy, at this moment the ADCS orbital position and attitude determination are no longer relevant. The attitude deviation caused by errors in the actuators of the ADCS are however still relevant, so this is also considered a design variable.

lasercom terminal downlink transmitter

The design variables for the downlink transmitter are similar to the design variables for the beacon transmitter, consisting of the optical output power and the downlink laser wavelength. However, for the satellite terminal the misalignment between the uplink receiver and downlink transmitter optical axes will be relevant, as the beam divergence of the downlink channel should be small and as it is close to impossible to align these optical axes after the satellite has been launched. For the downlink transmitter this is therefore considered a design variable.

lasercom terminal quad cell uplink receiver

Since both the beacon light incidence angle measurement and the uplink data reception are integrated in a single component, the quad cell receiver, this subsystem has to be modelled in greater detail to be able to capture all relevant effects. The first aspect of this subsystem is the optical design. This design can be described by the aperture size and the optical losses behind this aperture which together describe the light power that is projected on the quad cell. In a simplified description, the optical length between a focussing element and the quad cell determines the displacement of the projected light on the quad cell per deviation in the angle of incidence of the beacon light, as illustrated in Figure 18. The projected light dot has a finite diameter, which also has an influence on the precise response of the quad cell outputs to a displacement of this projected dot. Lastly, next to the beacon signal light, background light is also captured by the quad cell receiver. The amount of background light can be limited by using an optical filter that only passes a band close around the beacon wavelength. The total allowed background light power on the quad cell is therefore a design variable that describes the requirements on the optical filter.

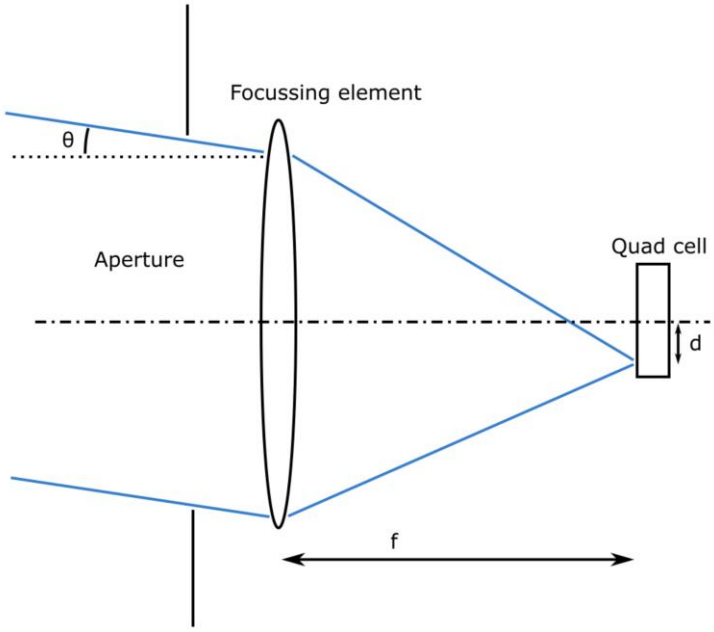

Figure 18: quadcell receiver optics geometry

Next, the characteristics of the quad cell also have to be described. In the computation of the response of the quad cell to a displacement of the projected dot the geometry of the quad cell itself plays a role. A quad cell commonly consists of a round photodiode, which has been cut in four segments, as illustrated in Figure 19. Relevant parameters are the quad cell diameter and the width of the cut in between the cells. Next to this a photodiode also has a certain sensitivity, the ratio of photocurrent that is generated by the photodiode per incident light power. The dark current of a photodiode is the current that flows through a photodiode without any light being present, which can be considered a fixed offset but also contributes to the shot noise. Lastly, the shunt resistance of a photodiode describes the thermal noise current generated by the photodiode itself.

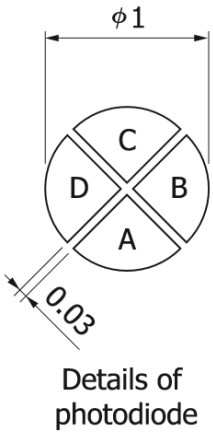

Figure 19: Quad cell photosensitive area geometry, taken from [20]

The amplification and readout electronics behind the quad cell need to be considered as well in the sizing of the lasercom system. For one, the total RMS output noise per quad cell channel determines the signal-to-noise ratio of the data conversion. The quad cell circuit bandwidth determines over which frequency range the noise of the quad cell itself should be integrated. To determine the angle measurement accuracy of the quad cell receiver, relevant parameters from the electronics are the portion of the noise level per quad cell channel that is seen by the angle measurement electronics, the maximum offset error between any two quad cell channels

and the maximum gain error between any two quad cell channels. The gain error is defined as the factor with which the measured photocurrent ratio between any two quad cell segments may deviate from the actual photocurrent ratio. Together, these design variables describe the performance of the quad cell receiver subsystem.

Link budget and atmospheric effects

The communication link budget and the influence of the atmosphere on this link can also be described by a few variables. Just like with the beacon light angular error due to atmospheric effects, these variables describe the margins that are incorporated in the lasercom system design, where higher margins lead to a higher statistical reliability of the system, at the cost of a more complex design. The link budget is completed by a loss term due to pointing errors, and a signal-to-noise margin for both the uplink and the downlink channels. The atmospheric effects on the link budget are described by a single atmospheric loss term which contains all atmospheric loss sources, such as wavefront errors (WFE), scintillation losses and absorption losses, since the modelling of atmospheric effects is out of scope for this research.

Table 5: lasercom system sizing design variables overview

Variable	Symbol	Units
Mission characteristics		
Orbital altitude	h_o	$[km]$
Min. spacecraft mass	$m_{SC,min}$	$[kg]$
Max. spacecraft mass	$m_{SC,max}$	$[kg]$
Ground station receiver		
Aperture diameter	d_{GS}	$[m]$
Ground station downlink optical losses	L_{GS}	$[dB]$
Detector photons/bit	N_S	$[-]$
Ground station beacon transmitter		
Optical output power	P_{up}	$[W]$
Wavelength	λ_{up}	$[nm]$
Atmospheric angular error	δ_{up}	$[rad]$
Ground station pointing mechanism		
Satellite orbital position prediction error	ϵ_{GS}	$[m]$
Closed-loop pointing error	δ_{GS}	$[rad]$
Satellite minimum elevation angle	α	$[deg]$
CubeSat ADCS characteristics		
Orbital position determination error	ϵ_{SC}	$[m]$
Open-loop attitude determination error	δ_{SC}	$[rad]$
lasercom terminal downlink specifications		
Optical output power	P_{down}	$[W]$
Wavelength	λ_{down}	$[nm]$
Misalignment between up/downlink channels	$\delta_{alignment}$	$[rad]$
lasercom terminal quad cell receiver		
Aperture diameter	d_{SC}	$[m]$
Terminal uplink optical losses	L_{SC}	$[dB]$
Projection optical length	l_{proj}	$[m]$
Projected light dot diameter	d_{dot}	$[m]$
Captured background light power	P_{bg}	$[W]$
Quad cell diameter	d_{QC}	$[mm]$
Spacing between quad cells	l_{QC}	$[mm]$
Quad cell sensitivity	R_λ	$[A/W]$
Quad cell dark current	I_d	$[A]$
Quad cell shunt resistance	R_{sh}	$[\Omega]$
Quad cell circuit bandwidth	BW_{QC}	$[Hz]$

Total RMS output noise per quad cell channel, input referred	I_{ch}	$[pA]$
Total RMS output noise per angle measurement channel, input referred	I_{meas}	$[pA]$
Max. gain error between any two channels	e_{gain}	$[\%]$
Max. offset error between any two channels, input referred	ϵ_{off}	$[pA]$
Link budget and atmospheric effects		
Pointing error loss	L_{point}	$[dB]$
Uplink link budget signal-to-noise margin	SNR_{up}	$[dB]$
Downlink link budget signal-to-noise margin	SNR_{down}	$[dB]$
Atmospheric losses	L_{atm}	$[dB]$

3.6.4. Pointing and acquisition process assumptions

In order to facilitate the calculation of some parameters, some assumptions are made on the acquisition process between the satellite and the ground station. It is assumed that on the CubeSat terminal, it will be necessary to keep the downlink laser divergence Θ_S small to reduce the power required by the downlink laser to achieve the same received optical power at the ground station receiver. It can thus be assumed that it will not be possible for the satellite to point its downlink beam accurately enough to hit the ground station before a link is established. For the ground station however, the limits on the beacon transmitted optical power are much less strict. This allows for a wider beacon divergence angle. The beacon divergence is therefore assumed to be driven by the errors in predicting the position of the satellite and pointing the ground station beacon transmitter and receiver telescope to this position: the beacon divergence angle Θ_B should be large enough that in a worst-case error in the initial pointing of the ground station, the satellite should still be able to receive the beacon signal to correct its own pointing. This assumed process is illustrated in Figure 20.

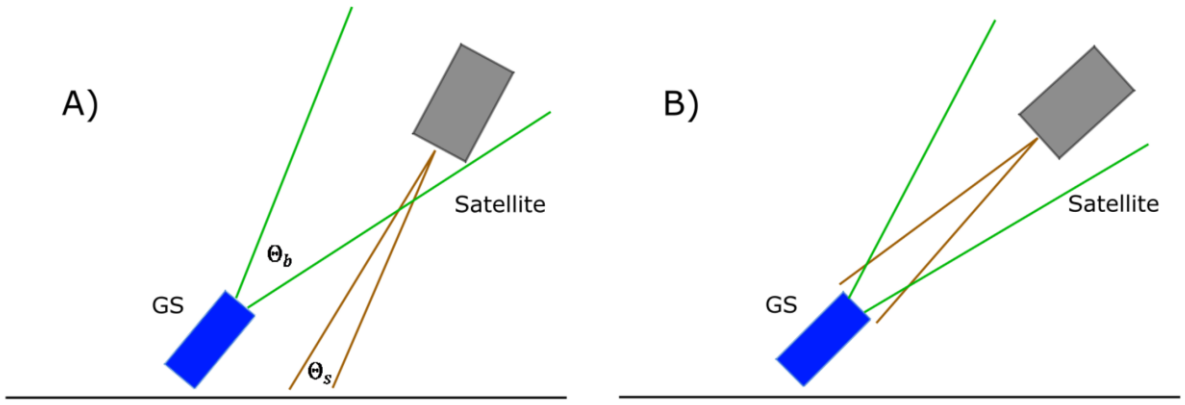

Figure 20: acquisition process assumption. A) during acquisition the ground station beacon should be visible for the satellite terminal. B) once the satellite has corrected its pointing using the ground station beacon a link can be established.

3.6.5. Lasercom system first-order sizing model

To be able to optimise the design of the lasercom system, a model of this system has to be constructed first that is capable of predicting the relevant performance metrics of a given design. For the lasercom system a first-order design methodology is chosen, where analytical and simple numerical relations and models are used to calculate the achievable bitrates, and thus data transferred per ground station overpass, from a given set of design variables. A rough prediction of the power consumption of the CubeSat terminal is also performed, in order to verify that the selected set of design variables meets the requirements established in sections 3.1-3.3. This covers requirements FR1, FR2, TR1, TR2, DR1 and DR2. Requirement

FR3, the amount of data stored in the CubeSat terminal, and requirements TR6 and TR7, the minimum and maximum supported orbital altitudes, are used as inputs in the sizing process.

This leaves requirements TR3, the CubeSat terminal size, TR4, the CubeSat terminal mass and TR5, the CubeSat terminal cost as requirements that are not verified by the model. Since lasercom terminals are such a recent development, no exhaustive database of reference lasercom terminals can be compiled with which a sufficiently accurate prediction can be performed on these aspects. Since the final results on these characteristics are therefore so much dependent on the detailed design of the CubeSat lasercom terminal, it is decided that the most efficient course of action is not to try to model these aspects during the sizing phase, as these models will likely be highly inaccurate and could thus do more harm than good, but instead assumptions will be used in the sizing phase in order to select a set of design variables that is likely to meet these requirements. During the detailed design phase these estimates will then have to be updated regularly and if the predicted design characteristics no longer meet the set requirements, a design iteration might be required in order to arrive at a design that meets all requirements.

The analytical and numerical relations that are used to size the lasercom system will be explained in the order in which these calculations are performed, where first a few intermediate calculations are explained. After this the overall link equations are given in order to arrive at the predicted datarates, data volumes transferred per ground station pass and power consumptions.

Mission characteristics

- Minimum satellite moment of inertia around long axis I_{sat}: in order to calculate the worst-case angular jitter in the satellite caused by the reaction wheels in the ADCS, the minimum satellite moment of inertia is required. The reaction wheel jitter is given as a disturbance torque, and the satellite moment of inertia determines the angular displacement that this jitter causes. The lower the moment of inertia, the larger the angular displacement, so the worst-case scenario is calculated by assuming the smallest satellite for which the lasercom system is foreseen, which is a 6U CubeSat, using the minimum satellite mass design variable, and calculating the moment of inertia around the longest axis of the satellite. The mass of the satellite is assumed to be evenly distributed over the volume of a 6U CubeSat, with dimensions of 10x20x30 cm. The moment of inertia of a rectangular prism with uniform mass is given as:

$$I = \frac{m(a^2 + b^2)}{12} \tag{1}$$

  Where, for the moment of inertia around the long axis of the CubeSat, a and b are the two smallest dimensions of the CubeSat, $0.1m$ and $0.2m$.

- Maximum link distance R_{max}: the maximum distance between the ground station and the satellite over which a link can be established. In the calculation of this variable it is assumed that the minimum satellite elevation angle α, together with the satellite orbital altitude, determines what the maximum link distance with which the rest of the sizing calculations are performed. The maximum link distance is calculated using orbital geometry, taken from [21], with:

$$R_{max} = -R_e\, sin(\alpha) + \sqrt{(R_e)^2\, sin^2(\alpha) + 2h_o R_e + h_o^2} \tag{2}$$

  Where R_e is the earth radius of $6371km$.

- Maximum satellite time within range T_{max}: in order to estimate whether a given set of design variables allows for a sufficient transfer time per ground station pass, the maximum satellite time within range is calculated. This is the time during which the satellite is above the minimum elevation angle of the ground station, the maximum time is achieved when the satellite passes directly above the ground station. In the simplest sense, this time can be written as:

$$T_{max} = T_o \cdot \frac{\lambda_{view}}{360} \tag{3}$$

Where T_o is the orbital period of the satellite and λ_{view} is the earth angle range in which the satellite is in view of the ground station. The orbital period for a circular orbit is given as:

$$T_o = 2\pi \sqrt{\frac{r^3}{\mu}} \tag{4}$$

Where μ is the earth gravitation parameter. The earth angle range over which the satellite is within view of the ground station can be calculated using simple geometry, illustrated in Figure 21. The earth angle range where the satellite is within view of the ground station can be observed to be twice the maximum earth angle λ_{max}. This angle can be calculated using the triangle earth centre – satellite – imaginary point above the ground station. The short side of this triangle is $R_{max}\cos(\alpha)$, the leg earth centre – satellite is $R_e + h_o$. The earth angle range within view can then be calculated using:

$$\lambda_{view} = 2 \cdot sin^{-1}\left(\frac{R_{max}\, cos(\alpha)}{R_e + h_o}\right) \tag{5}$$

The equation for T_{max} can now be rewritten to be:

$$T_{max} = 2\pi \sqrt{\frac{(R_e + h_o)^3}{\mu}} \cdot \frac{sin^{-1}\left(\frac{R_{max}\, cos(\alpha)}{R_e + h_o}\right)}{180} \tag{6}$$

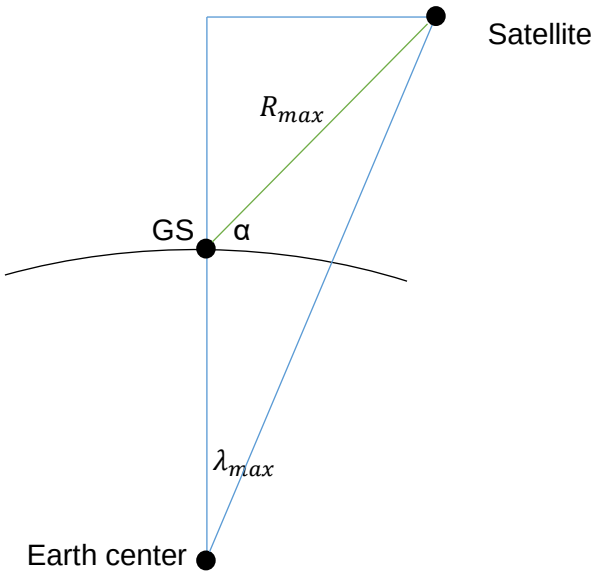

Figure 21: maximum satellite time within range geometry

Ground station specifications

- Full-angle beacon divergence angle Θ_b: the beacon divergence angle is defined as the angle between the two edges of the cone of light from the beacon, where the optical power has decreased by $3dB$ w.r.t. the power at the centre of this cone, also called the full-width half-maximum (FWHM) angle. As described in section 3.6.4, the beacon divergence angle should be large enough to be observable by the satellite, even at the largest initial pointing error of the satellite. The beacon divergence angle is thus calculated by multiplying the maximum initial pointing error of the ground station by two, since the divergence is defined as a full angle. During the initial pointing of the ground station, the ground station will have to predict where the satellite is in its orbit using ephemeris data. The angular pointing error that this causes is given by:

$$\delta_{predict} = tan^{-1}\left(\frac{\epsilon_{GS}}{R_{max}}\right) \quad (7)$$

  Further error factors in the initial pointing are the ground station closed loop pointing error δ_{GS} and the beacon angular error due to atmospheric effects δ_{up}. The equation for Θ_b then becomes:

$$\Theta_b = 2\,tan^{-1}\left(\frac{\epsilon_{GS}}{R_{max}}\right) + 2\delta_{GS} + 2\delta_{up} \quad (8)$$

ADCS specifications

- ADCS actuation error δ_{act}: the ADCS actuation error is the pointing angle deviation of the satellite caused by control errors and mechanical imperfections in the reaction wheels of the ADCS. For the calculation of this variable an internal model by Hyperion is used that has been constructed to estimate the pointing jitter caused by the RW400

reaction wheels. These wheels are designed by Hyperion for use in 6U and larger satellites, and are thus a good reference for reaction wheels that will be used in an ADCS that is coupled to the lasercom terminal. This model is based on a pointing jitter value that is normalised to the moment of inertia of the satellite, it should be noted that this is a highly simplified model as to date, no reaction wheel jitter measurement has been accurate enough to fully determine this actuation error. This model, as used internally by Hyperion, is given to be:

$$\delta_{act} = \frac{7.5 \cdot 10^{-8}}{I_{sat}} \tag{9}$$

Which gives δ_{act} as a 3 sigma value in radians.

Satellite terminal uplink specifications

- Captured beacon light power $P_{up,rec}$: the optical power that enters the satellite terminal uplink receiver depends on the receiver aperture size, transmitted beacon optical power, atmospheric loss, pointing loss and the uplink signal-to-noise margin. Since the beacon divergence angle Θ_B is small, small angle assumptions can be made. First, the total optical power from the beacon that is available at the position of the satellite is calculated (in dBW) with:

$$P_{up,sat} = 10\,log(P_{up}) - L_{atm} - L_{point} - SNR_{up} \tag{10}$$

With the small angle assumption, this power is assumed to be divided over a circular area. This area is calculated with:

$$A = \left(\frac{\Theta_b}{2} \cdot R_{max}\right)^2 \tag{11}$$

Since the pointing loss term takes into account that the optical power of the beacon is not evenly divided over this area and describes what the average power level is at the part of the circle that the satellite aperture receives, the total captured beacon light power is simply the ratio of the aperture diameter to the circular area A times the optical power $P_{up,sat}$ converted to Watt:

$$P_{up,rec} = \frac{d_{SC}^2}{(\Theta_b \cdot R_{max})^2} \cdot 10^{\frac{10\,log(P_{up}) - L_{atm} - L_{point} - SNR_{up}}{10}} \tag{12}$$

- Captured light detector noise per cell I_{det}: in a photodiode there are two noise sources, shot noise and Johnson noise [22]. Due to the quantum nature of photons, there is a statistical fluctuation in the photocurrent that is generated in a photodiode. This fluctuation is called the shot noise. The equation for shot noise is:

$$I_{sh} = \sqrt{2q(I_p + I_d) \cdot BW_{QC}} \tag{13}$$

Where q is the electron charge of $1.6 \cdot 10^{-19} C$ and Δf is bandwidth over which the shot noise is integrated. I_p is the photocurrent generated by the photodiode, and I_d is the dark current of the photodiode. The photocurrent I_p generated in one cell of the quad cell is assumed to be generated by one quarter of the optical power incident on the quad cell. This can be written as:

$$I_p = \frac{10^{\frac{10\,log(P_{up,rec})-L_{SC}}{10}} + 10^{\frac{10\,log(P_{bg})-L_{SC}}{10}}}{4} \cdot R_\lambda \tag{14}$$

The Johnson noise is calculated using:

$$I_{jn} = \sqrt{\frac{4k_B T \cdot BW_{QC}}{R_{sh}}} \tag{15}$$

Where k_B is the Boltzmann constant of $1.38 \cdot 10^{-23}\ J/K$ and T is the temperature of the photodiode. In order to calculate using worst-case conditions, for this temperature the maximum allowed operational temperature of $313K$ from requirement TR9 is used. The captured light detector noise per cell can now be calculated using:

$$I_{det} = \sqrt{I_{sh}^2 + I_p^2} \tag{16}$$

- Worst case convertible light power $P_{up,wc}$: the quad cell sensor contains an empty space in between the individual cells of the quad cell. When the uplink beacon light is projected perfectly in the centre of the quad cell, which happens when the beacon light angle of incidence is 0° w.r.t. the optical axis, a significant portion of this light will be projected on this empty spacing and thus will not contribute to the total generated photocurrent. This situation is illustrated in Figure 22. The worst case convertible light power can be written as:

$$P_{up,wc} = \frac{A_{active}}{A_{total}} \cdot 10^{\frac{10\,log(P_{up,rec})-L_{SC}}{10}} \tag{17}$$

Where A_{total} is the total area of the projected dot, given by:

$$A_{total} = \pi \left(\frac{d_{dot}}{2}\right)^2 \tag{18}$$

And A_{active} is the area of the projected dot that is projected onto the quad cell segments, which can be calculated making use of the fact that A_{active} can be cut in 8 identical parts due to symmetry:

$$A_{active} = 8\left(\frac{1}{8} \cdot A_{total} - \frac{sin^{-1}\left(\frac{l_{QC}}{d_{QC}}\right)}{2\pi} \cdot A_{total} - \frac{1}{2} d_{QC}\, cos\left(sin^{-1}\left(\frac{l_{QC}}{2d_{QC}}\right)\right) \cdot \frac{1}{2} l_{QC} \cdot \frac{1}{2}\right) \tag{19}$$

For the sake of clarity no simplifications have been performed on this equation.

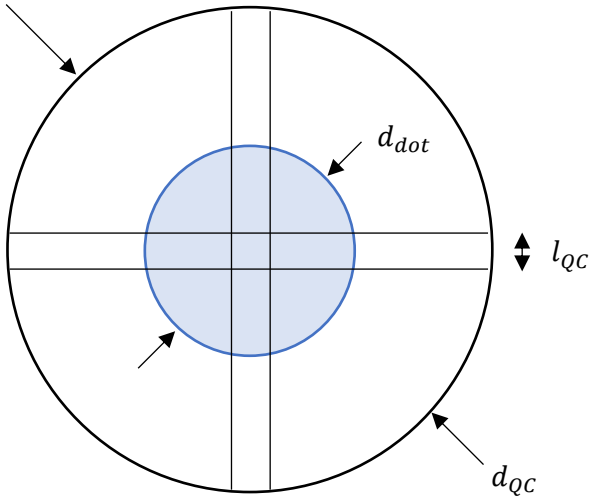

Figure 22: worst case convertible light power situation

- Quad cell angle measurement total current error (3 sigma) budget ϵ_{angle}: in order to determine how accurately the quad cell receiver circuit can determine the angle of incidence of the beacon light on the satellite terminal, first the total current error budget in the combination of the quad cell photodiode and the electrical readout circuit has to be determined. In the computation of the x- and y positions of the projected dot on the quad cell, for each axis the quad cell segments are summed in combinations of two. In other words, to compute the x position of the projected dot the difference in photocurrent between the sum of the two left segments and the sum of the two right segments is used. For the y axis the difference in photocurrent between the sum of the two upper segments and the sum of the two lower segments is used. The relevant error budget can thus be defined as the maximum deviation in the output signal between any sum of two quad cell channels and the sum of the other two quad cell channels when an equal light input is applied to each cell. This value is given in the form of the corresponding input photocurrent for this error in the output signal. The angle measurement error budget can be written as:

$$\epsilon_{angle} = 2\epsilon_{gain} + 2\epsilon_{off} + \sqrt{2} \cdot \epsilon_{noise,3\sigma} \tag{20}$$

Where ϵ_{gain} and ϵ_{off} are assumed to add linearly. The 3-σ error due to amplifier and detector noise is also added to arrive at a 3-σ certainty for the total error budget, the noise from the two segments adds as a square root sum. The worst-case angle measurement accuracy is achieved when the total light power captured by the quad cell receiver is minimal. All calculations are therefore performed assuming that the total power on the quad cell is equal to the worst case convertible light power $p_{up,wc}$. In this situation the optical power on each quad cell segment is 1/4th of the total optical power, so the gain error can be written as:

$$\epsilon_{gain} = e_{gain} \cdot \frac{1}{4} \cdot P_{up,wc} \tag{21}$$

The complete equation for ϵ_{angle} can be written as:

$$\epsilon_{angle} = 2 \cdot e_{gain} \cdot \frac{1}{4} \cdot P_{up,wc} + 2\epsilon_{off} + 3 \cdot \sqrt{2 \cdot I_{meas}^2} \tag{22}$$

- Uplink incoming angle range Θ_{up}: in order to size the range of angles over which the quad cell sensor should operate, also called the Field of View (FoV), the range of uplink light angles of incidence that is expected during operation is calculated. The maximum uplink angle of incidence is encountered when the pointing error of the satellite terminal to the ground station is maximal. This situation is encountered during the acquisition process, where the pointing accuracy of the satellite terminal depends on the accuracy of the host satellite ADCS and the satellite terminal is looking for the beacon uplink signal. The maximum uplink angle of incidence can thus be assumed to be equal to the error in the ADCS's ability to track a ground target. This error consists of the open-loop attitude determination error and the angular error caused by the ADCS orbital position determination error. This can be written as:

$$\Theta_{up} = \delta_{sc} + tan^{-1}\left(\frac{\epsilon_{sc}}{R_{max}}\right) \tag{23}$$

- Maximum uplink projection optical length $l_{proj,max}$: the displacement of the projected received uplink light on the quad cell sensor depends on the optical path length between the focussing element in the uplink receiver optics in the satellite terminal and the diameter of the quad cell sensor. It is assumed that the maximum allowed displacement of the projected dot on the quad cell is achieved when the centre of this projected dot reaches the edge of the quad cell. In this situation slightly less than half of the captured light is projected onto the quad cell segments, similar to the amount of light that is received by two cells of the quad cell when the projected dot is perfectly in the centre of the quad cell. In reality, when the centre of the projected dot is projected slightly beyond the edge of the quad cell, some light will still fall on one or two quad cell segments and the quad cell angle measurement circuit can still determine in which direction the satellite should rotate to correct this pointing error, but the further the projected dot moves beyond the edge of the quad cell, the lower the difference between the still-illuminated and the dark segments becomes and thus the higher the risk that the angle measurement circuitry fails in determining the right direction for correcting this pointing error. It is assumed that taking the situation where the centre of the projected dot falls on the edge of the quad cell sensor as the maximum displacement of the projected dot leaves a safe margin to prevent the satellite from correcting its pointing angle in the wrong direction.

  The displacement from the optical axis of the projected image behind focussing optics due to the angle of incidence of light from a source at an infinite distance is given by:

$$d = f\Theta \tag{24}$$

  Where Θ is the angle of incidence of the received light in radians and f is the focal length of the focussing optics. Assuming that the quad cell sensor will be placed close to the focal point of the focussing optics, this equation can be used to write:

$$l_{proj,max} = \frac{\frac{1}{2}d_{QC}}{\Theta_{up}} \tag{25}$$

  This value can be used as a check on the selected value for the projection optical length design variable l_{proj}, since if a larger optical length is selected, in a worst case scenario during acquisition the received beacon uplink light could be projected beyond the edge of the quad cell sensor.
- Angle of incidence per dot displacement R_Θ: to convert the displacement of the projected dot as measured by the quad cell to the angle of incidence of the received

beacon light equation (24) is used. To determine the angle of incidence in radians per meter of dot displacement, this equation can simply be written as:

$$R_\theta = \frac{1}{l_{proj}} \tag{26}$$

- Minimum detectable current difference ΔI_{det}: the minimum measurable difference in photocurrent between any sum of two cells and the sum of the other two cells of the quad cell depends on the total error budget for the quad cell receiver circuit ϵ_{angle}. Since this value describes with 3-σ certainty what the deviation between any combination of two cells is, the minimum photocurrent difference between any combination of two cells where the quad cell receiver circuit can tell with 3-σ certainty which of the two sums has the largest photocurrent (and thus, in which direction the pointing angle should be corrected), is twice the error current ϵ_{angle}. This value can thus be considered the 3-σ accuracy of the quad cell receiver circuit, assuming that no measures are taken to reduce the impact of offset errors.
- Angle measurement accuracy δ_{QC}: using the minimum detectable current difference I_Δ and the angle of incidence per dot displacement R_Θ the angle measurement accuracy of the quad cell receiver can be determined. First, the 3-σ photocurrent measurement accuracy of the quad cell receiver circuit is assumed to be equal to the minimum detectable current difference. The 3-σ angle measurement accuracy is then found by finding the projected dot displacement which gives this current difference between two sums of two cells, and then using the angle of incidence per dot displacement R_Θ to convert this displacement measurement accuracy to an angle measurement accuracy. To accurately determine this projected dot displacement a simple iterative numerical model is constructed. The basis of this model is that the projected dot initially is placed on the centre of the quad cell. The dot is then moved across one axis to the left with a finite step size, and after each step the illuminated area of the two leftmost and two rightmost segments is calculated. The corresponding photocurrent for both sums of segments is computed, and once the difference between these two currents is larger than the minimum detectable current difference I_Δ the total distance that the projected dot has been moved is returned. First, the received uplink light is assumed to be distributed evenly over the area of the projected dot. The irradiance of the projected dot is thus determined with:

$$H = \frac{10^{\frac{10\,log(P_{up,rec}) - L_{SC}}{10}}}{\pi\left(\frac{d_{QC}}{2}\right)^2} \tag{27}$$

To find the illuminated area of both quad cell segments, an integration method is used. The geometry of this method is illustrated in Figure 23.

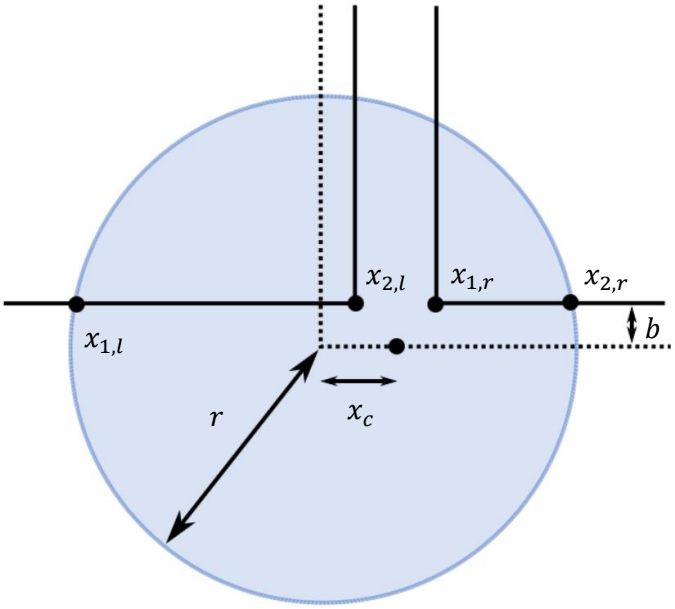

Figure 23: quad cell illuminated area per segment geometry

Since the dot is only displaced along the x-axis with distance x_c, due to symmetry the areas of the two upper segments are equal to the areas of the two lower segments. Variable r is equal to $\frac{d_{dot}}{2}$ and variable b is equal to $\frac{l_{QC}}{2}$. The areas for both segments are found with:

$$A_1 = \int_{x_{1,l}}^{x_{2,l}} \sqrt{r^2 - x^2} - b \, dx \tag{28}$$

And

$$A_2 = \int_{x_{1,r}}^{x_{2,r}} \sqrt{r^2 - x^2} - b \, dx \tag{29}$$

The photocurrents in the sum of the two leftmost segments and the sum of the two rightmost segments are then given by:

$$I_l = 2 \cdot A_1 \cdot H \cdot R_\lambda \tag{30}$$

And

$$I_r = 2 \cdot A_2 \cdot H \cdot R_\lambda \tag{31}$$

The algorithm for finding δ_{QC} can now be written in pseudocode as:

$x_c = 0$
$Repeat$:

$x_c = x_c + stepsize$
$x_{1,l} = -\sqrt{r^2 - b^2}$
$x_{2,l} = x_c - b$
$x_{1,r} = x_c + b$
$x_{2,r} = \sqrt{r^2 - b^2}$

$$A_1 = \int_{x_{1,l}}^{x_{2,l}} \sqrt{r^2 - x^2} - b \, dx$$
$$A_2 = \int_{x_{1,r}}^{x_{2,r}} \sqrt{r^2 - x^2} - b \, dx$$
$$\Delta I = 2 \cdot A_1 \cdot H \cdot R_\lambda - 2 \cdot A_2 \cdot H \cdot R_\lambda$$

$$Until\ \Delta I\ is\ equal\ to\ or\ larger\ then\ \Delta I_{det}$$
$$\delta_{QC} = x_c$$

For the variable $stepsize$ a small value van be used to achieve sufficient computational accuracy.

- Uplink data Signal-to-Noise ratio $SNR_{data,up}$: since for the quad cell uplink receiver the actual noise sources in the system are modelled, the signal-to-noise ratio for decoding the uplink channel data can be calculated directly from the ratio of the photocurrent due to the received uplink beacon light and the input-referred noise from the quad cell detector and amplifier circuitry. Since this ratio is a ratio of currents the SNR equation for a ratio of amplitudes must be used, since SNR is usually defined as a ratio of powers:

$$SNR_{dB} = 20\, log\left(\frac{A_{signal}}{A_{noise}}\right) \tag{32}$$

Which gives for $SNR_{data,up}$, in the worst case situation of the minimum convertible light power $P_{up,wc}$:

$$SNR_{data,up} = 20\, log\left(\frac{R_\lambda \cdot P_{up,wc}}{\sqrt{4I_{ch}^2 + 4I_{det}^2}}\right) \tag{33}$$

This value can be used to verify whether the link budget for the uplink data channel can be closed. If $SNR_{data,up}$ is negative, measures have to be taken to close the budget.

Downlink channel characteristics

- Full-angle downlink light divergence angle Θ_d: the downlink divergence angle is defined as the angle between the two edges of the cone of light from the downlink laser, where the optical power has decreased by $3dB$ w.r.t. the power at the centre of this cone. Just as with the uplink beacon divergence angle Θ_b, the width of this cone is chosen such that in worst-case satellite pointing conditions the ground station will be at the edge of this cone. In this way the pointing loss can be guaranteed to be less than $3dB$ (3-σ). Terms that contribute to the pointing error of the satellite once a link has been established (see Figure 20B) are the actuation angular error of the satellite δ_{act}, the misalignment between the optical axes of the up-and downlink channels $\delta_{alignment}$ and the angle measurement accuracy from the quad cell sensor δ_{QC}. Since the error term δ_{QC} consists largely of linearly-adding terms, it is assumed that δ_{QC} adds linearly to the pointing error of the satellite. $\delta_{alignment}$ adds linearly as well, which gives for the downlink divergence angle:

$$\Theta_d = 2\left(\delta_{QC} + \delta_{alignment} + \delta_{act}\right) \quad (34)$$

- Ground station detector optical power $P_{down,det}$: the optical power that is captured by the ground station and is received by the detector in the ground station. This number thus includes the optical losses in the ground station L_{GS}. Just as with the captured beacon light power $P_{up,rec}$, the received optical power is assumed to be equal to the total downlink optical power minus all loss terms times the ratio of the ground station aperture area to the total illuminated area. This can be written as:

$$P_{down,det} = \frac{d_{GS}^2}{(\Theta_d \cdot R_{max})^2} \cdot 10^{\frac{10\,log(P_{down}) - L_{atm} - L_{point} - L_{GS} - SNR_{down}}{10}} \quad (35)$$

- Downlink bitrate $R_{b,down}$: the ground station detector sensitivity and noise performance are modelled using a single variable, the ground station detector photons per bit N_s. To determine the maximum allowable bitrate over the downlink channel the optical power on the ground station detector $P_{down,det}$ must be converted to a photon flux. Using photon per bit number N_s this photon flux can be converted to a bitrate using:

$$R_{b,down} = \frac{P_{down,det} \cdot \lambda_{down}}{N_s \cdot h \cdot c} \quad (36)$$

  Where h is Planck's constant and c is the speed of light.

Satellite terminal power consumption

The modelling of the satellite terminal power consumption will be done on the basis of the lasercom satellite terminal block diagram of Figure 17. For each component a description is given on how the power consumption of this component is modelled. For each component two power consumption values are calculated: the power consumption during communication as used for requirement TR1 and the power consumption during low-speed data buffering as used for requirement TR2.

- Power conversion: the power consumption of the power conversion circuitry will be modelled by assuming a conversion efficiency for the power supplied to the other components. For the digital power conversion the design can be optimised for conversion efficiency. This helps reducing the power consumption in buffering mode, as all components that are active in this mode use the digital power. For the digital power a conversion efficiency of 90% is assumed. The analog power supply has to be optimised for a low supply voltage noise as well. It is assumed that a combination of DC-DC power conversion and linear voltage regulators will be used to reduce power losses while still keeping supply voltage noise low. For the analog power supply a conversion efficiency of 80% is assumed.

- Optical amplifier driver: since the optical amplifier driver will essentially be a DC-DC power converter, this converter will be modelled based on a conversion efficiency as well. This component is only active during communication and in this mode it is assumed that the power required by the optical amplifier will be supplied by the driver with an efficiency of 90%.

- Seed laser driver: The seed laser driver is more complex, since it must modulate the seed laser at high rates. To predict the power consumption of the seed laser driver, a reference driver suitable for optical communication is selected to base the power model on. The DR-DG-10-MO-NRZ from iXblue is a low-power driver designed for the electrical modulation of an optical signal [23]. For this device a power dissipation $3W$

is specified for an output power of $0.72W$. The conversion efficiency for this driver is thus assumed to be 20%.

- Photonics: to estimate the efficiency and the required seed laser power level for the photonics module, reference components are used. A good reference EDFA-based optical amplifier is the HYDRA from Gooch & Housego [24], since it is designed for use in space. This amplifier requires $3.1W$ for an output power of $0.13W$, but it should be noted that this includes the optical amplifier driver. It can thus be assumed that the electrical-to-optical efficiency of this optical amplifier of 4.2% includes the 90% efficiency of the optical amplifier driver. The required input seed laser power for this amplifier is $1mW$. Using information from a reference seed laser from Gooch & Housego [25], the efficiency and power consumption of the seed laser can be estimated. This seed laser achieves an optical output of $18mW$ for an input power of $200mW$, which gives an efficiency of 9%. Together with the efficiency of the seed laser driver and the power conversion for the digital circuitry, the total efficiency for the seed laser can be written as: $\eta_{seed} = 0.09 \cdot 0.2 \cdot 0.9 = 0.016$. Assuming that the ratio between the seed laser power level and the optical amplifier output power is constant, which for the selected reference EDFA is 0.0076, the power consumption for the seed laser during communication, including all intermediate power conversions and drivers, can be estimated with $P_{seed} = \frac{P_{down} \cdot 0.0076}{0.09 \cdot 0.2 \cdot 0.9}$. The power consumption for the optical amplifier during communication, including the efficiency of the optical amplifier driver, can be estimated with $P_{OA} = \frac{P_{down}}{0.042}$.

- Quad cell receiver electronics: while the power consumption of the quad cell receiver electronics could depend on the selected bandwidth, noise level and error targets, this influence depends greatly on the detailed design of the quad cell receiver electronics. It is therefore assumed that the power consumption for the quad cell receiver electronics is fixed. To determine a suitable power consumption for the quad cell receiver electronics a reference device is used from Thorlabs [26]. This quad cell receiver module has a power consumption of $350mW$. It should be noted that this design likely isn't optimised for a low power usage. The quad cell receiver electronics will only be active during communication. Including the analog power conversion efficiency, the total power for the quad cell receiver is assumed to be $0.44W$.

- Processor: Hyperion Technologies has heritage in embedded computing platforms for CubeSats in the form of the Hyperion OBC [27]. This platform is a high-performance embedded computing platform, with a typical power consumption of $0.55W$. It is assumed that the computing power of this module will be more than sufficient for performing all tasks that are not already handled by the FPGA in communication mode. This power consumption, including the digital power conversion efficiency of 90% giving $0.61W$, is therefore assumed to be a reasonable estimate of the processor power consumption during communication. During buffering mode, at the assumed buffering data rate of $20Mbps$ from requirement TR2, The total required computational power for handling and forwarding this slow data stream to the FPGA will be low. The Hyperion OBC has a low-power sleep mode, so its idle power consumption can be assumed to be negligible. A reasonable assumption for the average power consumption of the OBC in this mode is 20% of the typical power consumption, or $0.12W$.

- FPGA: The tasks of the FPGA include passing along data between the mass storage, the on-board processor, the downlink transmitter channel and the uplink receiver channel. Next to this, if necessary, the FPGA will run the error correction algorithms on this data. The power consumption of the FPGA will highly depend on the up- and

downlink datarates from requirements DR1 and DR2 and the precise characteristics of the applied error correction algorithms. To at least get an estimate of the FPGA power consumption, a reference calculation has been performed using the power estimator for an FPGA that would be suitable for use in the lasercom satellite terminal, The Polarfire from Microsemi. This FPGA family has been optimised for low power consumption while still offering considerable performance. Using the power estimator [28] a scenario is analysed where 75% of the resources of a mid-sized FPGA is used, along with a high-speed transceiver interface for interfacing to the downlink seed laser driver and a PCIe interface for interfacing with the mass storage. The estimated power consumption in this scenario is $1.8W$ active power, which can be used as an estimated FPGA power consumption during communication. Including the digital power conversion efficiency this gives a power consumption of $2W$. Just as for the processor, during buffering a 20% active ratio is assumed. The computed idle power consumption of this scenario is $0.1W$, so assuming that during buffering mode the FPGA will be active for 20% of the time and in idle for 80% of the time, the buffering mode power consumption including the digital power conversion efficiency is estimated at $0.48W$.

- Mass storage: since SSDs are a standardised component, the differences in functionality and power consumption between different SSDs are small. A reference SSD from Samsung can therefore be used for estimating the mass storage power consumption [15]. The idle power consumption of this SSD is specified to be $40mW$. The power consumption during read operations, at a maximum rate of $3500MB/s$, is specified at $5.1W$. The power consumption during write operations, at a maximum rate of $2100MB/s$, is specified at $4.7W$. These values are all valid for the smallest SSD in this family, with a capacity of $512GB$. During buffering at the assumed buffering data rate of $20Mbps$ from requirement TR2, the SSD has to be active for at least 0.12% of the time to handle this data stream. Including overhead, it is assumed that the SSD will consume $4.7W$ for 0.24% of the time during buffering, with $40mW$ for the rest of the time. Including the digital power conversion efficiency, this gives an average power consumption of $57mW$ for the mass storage during buffering mode.

  During communication with a continuous read rate of $1Gbps$ the SSD has to be active for at least 3.6% of the time. Including overhead, it is assumed that the SSD will be active and will consume $5.1W$ for 7.2% of the time during communication, with $40mW$ for the rest of the time. This gives an average power consumption of $0.45W$ for the mass storage during communication mode.

Using these assumptions and estimations the total power consumption of the satellite lasercom terminal can be compiled. This total power consumption is given in Table 6. During buffering the total power consumption is estimated at $0.66W$. During communication the total power consumption is largely dependent on the required optical power for the downlink, due to the low efficiencies of both the photonics components and their drivers.

Table 6: satellite lasercom terminal power consumption estimation, including power conversion efficiencies

Component	Power consumption buffering	Power consumption communication
Photonics (incl. drivers)	-	$\frac{P_{down}}{0.042} + \frac{P_{down} \cdot 0.0076}{0.09 \cdot 0.2 \cdot 0.9}$
Quad cell receiver electronics	-	$0.44W$
Processor	$0.12W$	$0.61W$
FPGA	$0.48W$	$2W$
Mass storage	$57mW$	$0.45W$

3.7. lasercom system baseline design

In section 3.6 a first-order model is constructed with which a baseline design for the lasercom system can be established. This model is based on a number of design variables that together describe and constrain the design for the lasercom system. By selecting an appropriate set of design variables for this lasercom system, together called the design vector, it can be shown that a lasercom system that fits within the constraints of the CubeSat form factor can be constructed. In the following sections this design vector will be established based on the requirements on the lasercom system, based on input from Hyperion Technologies, based on input from TNO and based on several design choices.

3.7.1. Design variables from system requirements

Some of the variables mentioned in Table 5 can be determined from the requirements imposed on the lasercom system, as described in section 3.1-3.3. For the orbital altitude h_o the worst-case condition is imposed by the maximum orbital altitude. This altitude is prescribed by requirement TR7 to be $800km$. Since requirements TR3 and TR4 describe a lasercom terminal with a size of 1U, one standardised CubeSat unit, it would be unrealistic to expect the lasercom terminal to be used on a 3U CubeSat since this would leave limited space for a payload and other satellite components. The next standard CubeSat size is a 6U satellite, where a communications module of 1U would be an acceptable solution. Taking the standard CubeSat component mass of $1.5kg$ per U into account, the minimum spacecraft mass $m_{SC,min}$ is determined to be $9kg$.

The uplink datarate of $200kb/s$ from requirement DR2 determines the quad cell receiver circuit bandwidth BW_{QC}. For a non-return-to-zero on-off keying modulated signal, the required bandwidth for the quad cell receiver is half the datarate, which in this case corresponds to a bandwidth of $100kHz$.

3.7.2. Design variables established by Hyperion Technologies

Existing technologies and marketing considerations also prescribe optimal values for some design variables. Some other CubeSat components sold by Hyperion are designed for use in CubeSats with sizes up to 12U, such as the ADCS400. For this reason the lasercom system will be designed for this form factor as well. The maximum spacecraft mass is therefore determined to be $18kg$. The ADCS orbital position determination error ϵ_{SC} and the ADCS open-loop attitude determination error δ_{SC} are also prescribed by Hyperion Technologies to be $150\ \mu rad$ and $10m$ respectively.

3.7.3. Design variables established by TNO

Since TNO is responsible for the optical design and atmospheric models for the lasercom system, several design variables are determined by the results of their work. Since the ground station is part of the optical design by TNO, most variables related to the ground station are established by TNO. The ground station aperture diameter d_{GS} is given to be $0.6m$, the optical losses in the ground station L_{GS} are given to be $3.75dB$ and the required detector photons/bit N_S is given to be 1400 for a bit error rate (BER) of 10^{-6}.

The beacon transmitter on the ground station is given to be a $15W$ source for P_{up} at a λ_{up} of $1590nm$. The atmospheric angular error in the uplink channel δ_{up} is determined to be $130\mu rad$. The orbital position prediction error in the ground station ϵ_{SC} will be $10m$ and the closed-loop pointing error in the ground station δ_{GS} will be $45\mu rad$.

Several variables related to the satellite terminal are determined by design work from TNO as well. The downlink laser source as sourced by TNO is specified to offer optimum performance at an optical output power P_{down} of $0.14W$ with a wavelength λ_{down} of $1550nm$. The misalignment between the up- and downlink channels $\delta_{alignment}$ is specified to be $10\mu rad$. The aperture diameter for the uplink receiver d_{SC} will be $14mm$ and the total optical length l_{proj} after the focussing element in the lasercom terminal is specified to be $200mm$. Optical losses in the uplink receiver L_{SC} are specified to be $3dB$. The estimated captured background light power P_{bg} is $10nW$. Lastly, atmospheric losses L_{atm} are determined to add up to $2.44dB$. With these design variable values, TNO is capable of designing an optical segment for the satellite terminal that takes up an acceptable part of the 1U size and weight constraint, for an acceptable portion of the production cost from requirement TR5.

3.7.4. Design variables established in this work

Apart from the design variables that are prescribed by existing technology and external influence, some design variables are free to be established in this work. The first one is the satellite minimum elevation angle α. While the pointing mechanism of the ground station will allow for low minimum elevation angles, at an orbital altitude of $800km$ this will give a prohibitively large maximum link distance R_{max}. For requirement DR1 a total data transfer time of 100 seconds is assumed to transfer the required data volume of $100Gbit$ from requirement FR1. Considering that this data transfer must also be achieved if the satellite does not pass directly over the ground station, and that time has to be reserved for the link acquisition process, the maximum satellite time within range T_{max} should end up to be much larger than 100 seconds. Using the equations from section 3.6.5 a minimum satellite elevation angle of $50°$ is selected, as this gives a convenient maximum link distance of slightly more than $1000km$ and a maximum satellite time within range of 546 seconds.

The design variables related to the satellite terminal quad cell receiver are also still open. To establish values for the quad cell sensor diameter d_{QC}, spacing between the quad cell cells l_{QC}, the quad cell sensitivity R_λ, quad cell dark current I_d and quad cell shunt resistance R_{sh} a reference quad cell sensor has to be selected. Not many quad cell sensors that are sensitive at $1590nm$ are commercially available, but one that combines a low sensor noise with a small spacing between the quad cell cells and an acceptable total sensor diameter is the G6849-01 from Hamamatsu. This sensor has a diameter of $1mm$, a cell spacing of $0.03mm$, a sensitivity at $1590nm$ of 0.95, a dark current of $180pA$ and a shunt resistance of $50M\Omega$ [20]. In order to be able to measure the position of the projected dot on the quad cell, all four cells must be illuminated in order to determine the ratio of photocurrents between all cells as described in section 4.6. With a sensor diameter of $1mm$ the most efficient choice for a projected dot diameter d_{dot} is $0.5mm$, since with this diameter the maximum allowable dot displacement where still all four cells are illuminated is achieved with the projected dot still falling completely within the diameter of the quad cell sensor.

The quad cell amplifier offset and gain errors are based on the results from the experimental tests described in chapter 0, along with the noise levels at the full amplifier bandwidth and as seen by the angle measurement calculations. The gain error e_{gain} is determined to be 0.01, the input-referenced maximum offset error between two cells ϵ_{off} is $10pA$, the input-referenced RMS noise per quad cell channel I_{ch} at the full bandwidth BW_{QC} is $95pA$ and the input referenced RMS noise per angle measurement channel I_{meas} at the angle measurement bandwidth of $10Hz$ is determined to be $1pA$.

The pointing error loss L_{point} is already defined by the assumptions behind the sizing model described in section 3.6.5. The uplink and downlink light divergence angles are sized such that with a worst-case pointing error both the uplink receiver and the downlink receiver will be at the edge of the uplink and downlink light beams respectively. The edge of these light beams

is defined as the half-maximum power of that beam, which implies that in a worst-case pointing condition the pointing error loss will be $3dB$.

Lastly, the up- and downlink signal to noise margins SNR_{up} and SNR_{down} are adjusted to arrive at an achievable bitrate of $1Gb/s$ for the downlink according to the model described in section 3.6.5. Positive values for both signal to noise margins indicate that the baseline design can meet the established requirements with a certain room for error. If a margin of $3dB$ is selected for SNR_{up}, then according to the model described in section 3.6.5 a margin of $2.7dB$ will remain for SNR_{down} for a datarate of $1Gb/s$. This leaves sufficient margin in both the up- and downlink budgets for unknowns and uncertainties in the model and the slight difference between the two budgets implies that the error rate in the downlink channel will go up, before the received power on the quad cell will be too low for sufficient pointing accuracy in the situation of a drop in signal strength.

3.7.5. lasercom baseline design modelled performance

In Table 7 an overview is given of the selected design variable values, along with the computed intermediate results according to the model described in section 3.6.5 and the resulting downlink bitrate and estimated lasercom terminal power consumption in Table 8.

Table 7: selected design variable values for the baseline lasercom system design

Variable	Symbol	Value	Units
Mission characteristics			
Orbital altitude	h_o	800	$[km]$
Min. spacecraft mass	$m_{SC,min}$	9	$[kg]$
Max. spacecraft mass	$m_{SC,max}$	18	$[kg]$
Ground station receiver			
Aperture diameter	d_{GS}	0.6	$[m]$
Ground station downlink optical losses	L_{GS}	3.75	$[dB]$
Detector photons/bit	N_S	1400	$[-]$
Ground station beacon transmitter			
Optical output power	P_{up}	15	$[W]$
Wavelength	λ_{up}	1590	$[nm]$
Atmospheric angular error	δ_{up}	130	$[\mu rad]$
Ground station pointing mechanism			
Satellite orbital position prediction error	ϵ_{GS}	10	$[m]$
Closed-loop pointing error	δ_{GS}	45	$[\mu rad]$
Satellite minimum elevation angle	α	50	$[deg]$
CubeSat ADCS characteristics			
Orbital position determination error	ϵ_{SC}	10	$[m]$
Open-loop attitude determination error	δ_{SC}	150	$[\mu rad]$
lasercom terminal downlink specifications			
Optical output power	P_{down}	0.14	$[W]$
Wavelength	λ_{down}	1550	$[nm]$
Misalignment between up/downlink channels	$\delta_{alignment}$	10	$[\mu rad]$
lasercom terminal quad cell receiver			
Aperture diameter	d_{SC}	14	$[mm]$
Terminal uplink optical losses	L_{SC}	3	$[dB]$
Projection optical length	l_{proj}	200	$[mm]$
Projected light dot diameter	d_{dot}	0.5	$[mm]$
Captured background light power	P_{bg}	10	$[nW]$
Quad cell diameter	d_{QC}	1	$[mm]$
Spacing between quad cells	l_{QC}	0.03	$[mm]$

Quad cell sensitivity	R_λ	0.95	$[A/W]$
Quad cell dark current	I_d	180	$[pA]$
Quad cell shunt resistance	R_{sh}	50	$[M\Omega]$
Quad cell circuit bandwidth	BW_{QC}	100	$[kHz]$
Total RMS output noise per quad cell channel, input referred	I_{ch}	95	$[pA]$
Total RMS output noise per angle measurement channel, input referred	I_{meas}	1	$[pA]$
Max. gain error between any two channels	e_{gain}	1	$[\%]$
Max. offset error between any two channels, input referred	ϵ_{off}	10	$[pA]$
Link budget and atmospheric effects			
Pointing error loss	L_{point}	3	$[dB]$
Uplink link budget signal-to-noise margin	SNR_{up}	3	$[dB]$
Downlink link budget signal-to-noise margin	SNR_{down}	2.7	$[dB]$
Atmospheric losses	L_{atm}	2.44	$[dB]$

Table 8: computed system performance using the design variable values from Table 7 and the model described in section 3.6.5.

Variable	Symbol	Value	Units
Minimum satellite moment of inertia	I_{Sat}	0.0375	$[kg/m^2]$
Maximum link distance	R_{max}	1006	$[km]$
Maximum satellite time within range	T_{max}	546	$[s]$
Full-angle beacon divergence angle	Θ_b	370	$[\mu rad]$
ADCS actuation error	δ_{act}	2	$[\mu rad]$
Captured beacon light power	$P_{up,rec}$	3.04	$[nW]$
Captured light detector RMS noise per cell	I_{det}	9.2	$[pA]$
Worst case convertible light power	$P_{up,wc}$	1.3	$[nW]$
Quad cell angle measurement total current error (3σ)	ϵ_{angle}	30.6	$[pA]$
Uplink incoming angle range	Θ_{up}	160	$[\mu rad]$
Maximum uplink projection optical length	$l_{proj,max}$	3.13	$[m]$
Angle of incidence per dot displacement	R_Θ	5.0	$[\frac{mrad}{mm}]$
Minimum detectable current difference	ΔI_{det}	61	$[pA]$
Angle measurement accuracy	δ_{QC}	55	$[\mu rad]$
Uplink data signal-to-noise ratio	$SNR_{data,up}$	16.4	$[dB]$
Full-angle downlink light divergence angle	Θ_d	134	$[\mu rad]$
Ground station detector optical power	$P_{down,det}$	179	$[nW]$
Downlink bitrate	$R_{b,down}$	1.0	$[Gb/s]$
Satellite terminal buffering power consumption	P_{buf}	0.66	$[W]$
Satellite terminal communication power consumption	P_{com}	8.4	$[W]$

4 Detailed electronic design

The design variable values established in chapter 0 describe a lasercom system design that should be able to meet the requirements described in sections 3.1-3.3. However, due to the low fidelity of the modelling method used to predict the performance of this lasercom system, a more detailed analysis is required to support the proposition that a lasercom system can be designed that is capable of meeting the established requirements. In Table 9 an overview is given of some aspects of the lasercom system, along with an indication whether these aspects are proven in practice and commonly used.

Table 9: lasercom system technology state-of-art overview

Aspect	Proven?	Commonly used?
Mechanical design of CubeSat components containing optical instruments	✓	✓
Optical design of CubeSat components	✓	~
Application of EDFA-based photonics in a CubeSat	✓	
Application of embedded processors and FPGAs in a CubeSat	✓	✓
Application of SSDs in a CubeSat	✓	
Application of laser drivers in a CubeSat	✓	
Application of power electronics and power convertors in a CubeSat	✓	✓
Design of a quad cell receiver circuit with the specifications outlined in chapter 0		

The mechanical design of CubeSat components containing optical instruments, and the design of these instruments is nowadays common technology, applied in for example earth or space observation mission and within Hyperion applied in the design of the star tracker and the imager. It should however be noted that these optical designs are usually relatively simple, designs using multiple optical elements as will be necessary for this lasercom system can hardly be called commonly used. EDFA-based photonics have been applied in CubeSats as well, some of the reference systems mentioned in chapter 2 make use of EDFA-based designs, of which the MIT NODE project is a notable example [11]. These CubeSats containing EDFAs are however all research satellites and technology demonstrators, so this technology cannot yet be considered commonly used.

Embedded processors and FPGAs are commonly used in CubeSat components, amongst others in the products sold by Hyperion. It is known that COTS SSDs are being applied in CubeSats [29], but details on their performance or lifetime in orbit are unknown. Laser drivers have been applied in the same missions as where EDFAs have been applied from chapter 2. Almost all CubeSat components require some form of power conversion on board, and almost every CubeSat contains at least some power electronics to manage the charging and discharging of the on-board batteries. Quad cell circuits have been applied in lasercom systems, amongst others in some of the missions mentioned in chapter 2, namely SOTA [3], OSIRIS for BiROS [10] and the Aerocube OCSD [7] but SOTA and OSIRIS are lasercom terminals for larger satellites and the Aerocube OCSD angle measurement accuracy does not meet the quad cell circuit specifications for this lasercom system as determined in chapter 0. This is therefore deemed an unproven technology.

Looking at Table 9, it can be concluded that most uncertainties in the proposed lasercom system design exist in the electronic design of the satellite terminal. To support the validity of the results of chapter 2, the electronic design of the satellite terminal will be investigated in further detail by creating an implementation of the design proposed in chapter 2. For each component of the electronic design as illustrated in Figure 17 a practical implementation will be described, along with the predicted performance and power consumption of this component.

4.1. Processor

The main tasks of the processor on the satellite lasercom terminal, as described in chapter 0 include:

- Forwarding downlink data from the satellite bus to the mass storage, through the FPGA.
- Forwarding received data from the uplink to the satellite bus
- Managing the communication link: arranging retransmission of failed data blocks, monitoring the link status and adjusting parameters such as downlink laser power and quad cell receiver gain accordingly.
- Forwarding quad cell angle measurement results to the satellite ADCS
- Housekeeping, monitoring system status and forwarding telemetry information to the satellite bus

To perform these functions the processor will require the following features:

- A high speed communication interface to the satellite bus. As described in section 3.5.1, a USB bus will be used for this interface.
- A high speed interface to the FPGA. Since an FPGA can support close to any interface standard, the most convenient one available on the selected processor can be used.
- Sufficient computational power and speed to handle high datarates over the USB interface.
- Additional low-speed satellite bus interfaces to be compatible with different architectures and standards, such as I^2C, RS485 and CAN.
- Low-speed communication interface to receive angle measurement results from the quad cell receiver electronics
- Sufficient RAM memory to buffer data locally, if necessary. It could be power efficient to let the FPGA and mass storage sleep for as long as possible, and let the data coming from the satellite bus to be transmitted on the downlink first be buffered on the processor. In this way the power-hungry FPGA and mass storage only have to be woken up for short data bursts during buffering mode. If it turns out that it is more energy efficient to directly forward all received data, this RAM memory can be removed in a later stage.

From the list of required features it is clear that the processor must mainly be capable of moving data at high rates: no complex computational functionality is required from the lasercom terminal processor. A processor that suits these requirements is the Atmel SAM E70 family [30]. This processor has built-in support for different high-speed interfaces such as USB 2.0, Quad SPI, SDIO, Ethernet and ISI, and also multiple slower communication interfaces such as CAN, I^2C, UART and RS-485. To enable fast data transfers this processor contains a Direct Memory Access (DMA) controller and to allow for the buffering of data on the processor, the built-in SDRAM controller can be used.

In the datasheet for this processor [30] it is described that to enable USB operation, the supply voltages must be $3.3V$. A disadvantage of this is that all IO pins of this processor will then also run at $3.3V$, which means that a $3.3V$ SDRAM chip has to be used instead of a lower-power $1.8V$ SDRAM chip. An example of such a device is the IS42SM16800H [31]. The active power consumption of this device is $165mW$, which is already more than the estimated power consumption during buffering from section 3.7.5. It is therefore assumed that all data that is received over USB can be transferred directly to the FPGA and the mass storage.

To connect this processor to the FPGA the Quad SPI (QSPI) interface can be used. This is a fast and simple interface, which on this processor supports a maximum transfer rate of $300Mb/s$ over four channels, using the maximum supported clock rate of $75MHz$. This is lower than the maximum supported data rate of USB of $480Mb/s$, which does mean that the maximum supported buffering speed will be limited by the QSPI interface. However, given that the average buffering datarate is assumed to be $20Mb/s$ per requirement TR2, this leaves sufficient margin for transferring buffer data to the lasercom terminal in bursts.

A schematic overview of the processor segment and its connections in the lasercom satellite terminal is given in Figure 24. Some simple connections to the seed laser driver and the optical amplifier driver are also included, in order to enable the photonics module, monitor its status and control its output power.

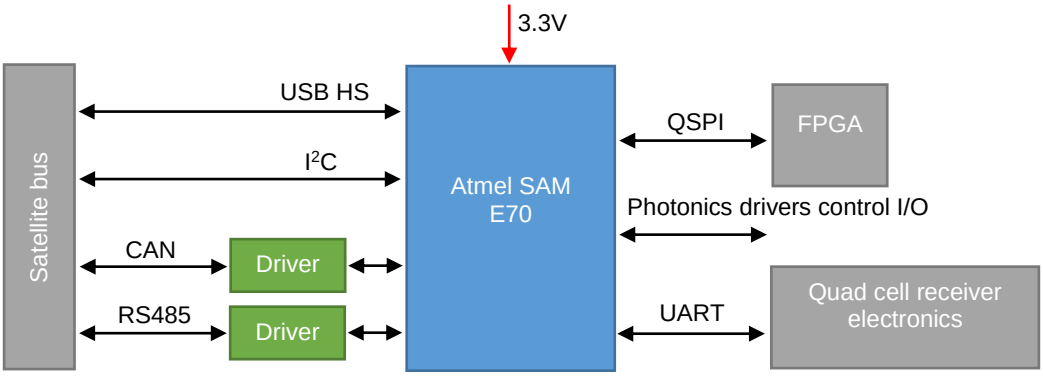

Figure 24: satellite terminal processor segment schematic overview

The power consumption of a processor module depends on the software implementation of its functionality. Since the software design for the lasercom satellite terminal is out of scope for this work, assumptions will be made on how much time the processor spends in different power consumption modes. The processor has a $3.3V$ input voltage, but uses an internal voltage regulator to supply $1.2V$ to the processor core and a few other internal components. This voltage regulator is a linear voltage regulator, so all current consumption on the $1.2V$ lines can be added to the current consumption on the $3.3V$ line. During buffering it is assumed that data will arrive at the lasercom terminal in bursts, with an average data transfer rate of $20Mb/s$. The burst data rate is assumed to be slightly below the maximum supported datarate of $300Mb/s$ to account for inefficiencies and overhead. Assuming a burst datarate of $270Mb/s$, the processor will be receiving data for 11% of the time and sit idle for 89% of the time. The current consumptions of the different components of the processor are, as determined using the processor datasheet [30]:

- Core: Assuming that the processor will run at the maximum clock rate during communication, the core current consumption will be 90mA during data transfer. During idle time, the processor is assumed to enter wait mode. This is a lower-power state from which the processor can wake up quickly. In this mode the total current consumption of the processor core is $0.5mA$

- USB module: The USB module will have to be active continuously to maintain a connection to the satellite bus. All USB components together consume $52mA$ during data reception, and $28mA$ when the bus is idle
- QSPI communication: the current consumption from QSPI communication comes from the IO pins which are driven at high rates and from the internal QSPI module. Assuming that the five QSPI pins (four data pins and one clock pin) toggle continuously at a speed of $75MHz$, the total current consumption from the pins is $22.9mA$. The current consumption of the internal QSPI controller is almost negligible at $0.3mA$. During idle time the QSPI module can be switched off completely.
- Low-speed bus interface: different low-speed bus interfaces will be available on the lasercom satellite terminal in order to be compatible with different CubeSat platforms. From the three available interface types (I^2C, RS485 and CAN), CAN is the most energy-consuming standard. It is assumed that the CAN module in the processor should be active at all times in order to respond to requests and commands from the satellite bus. This current consumption is $1.4mA$. An external driver will also be required in order to interface the processor to the CAN bus. The standard CAN driver used within Hyperion has a power consumption of $11.6mW$ while listening, and $181.5mW$ during transmission. The CAN bus however is a relatively fast bus at $5Mb/s$ and since the lasercom satellite terminal will only transmit housekeeping and telemetry information over this bus which consists of small amounts of data, the average power consumption due to CAN transmission is negligible.

Since all operating currents can be added if the internal $1.2V$ regulator is used, the power consumption of the processor is calculated by multiplying all currents with the operating voltage of $3.3V$. The power consumption of the processor during downlink communication is calculated by assuming that the processor will be active for the full duration of the communication link, along with the QSPI module. The USB module is assumed to be idle, as no new downlink data is generated during downlink communication. The power consumption of the low-speed UART connection to the quad cell receiver electronics is ignored. The CAN bus is assumed to be active and listening at all times. The calculated power consumption of the processor in different situations is summarised in Table 10.

Table 10: Processor power consumption summary

Component	Idle mode	USB reception	Downlink mode
Processor core	$2mW$	$297mW$	$297mW$
USB module	$92mW$	$172mW$	$172mW$
QSPI communication	$0mW$	$77mW$	$77mW$
Low-speed interface	$16mW$	$16mW$	$16mW$
Total	$110mW$	$562mW$	$562mW$

Using the estimated division between processor idle time and USB reception time of 11% and 89%, the average processor power consumption during buffering mode is calculated to be $160mW$. This number can however be reduced with $16mW$ by using the I^2C interface as a low-speed satellite bus interface, as this bus is much less energy consuming.

4.2. FPGA

The main tasks of the FPGA on the satellite lasercom terminal, as described in chapter 0 include:

- Storing data coming from the processor in the mass storage.

- Upon request, sending data received by the uplink from the mass storage to the processor.
- Transmitting buffered data from the mass storage by converting it to a modulation pattern for the downlink seed laser.
- Storing received uplink data in the mass storage.
- Run error correction algorithms on the data read from the mass storage and on the data received from the uplink to detect and correct data corruption.
- Apply error correction information on the data written to the mass storage and on the data sent to the downlink to allow for error correction algorithms to detect and correct data corruption on these data streams.

To perform these functions, the FPGA will require the following features:

- A high-speed transceiver to interface the FPGA with the downlink seed laser driver, which supports a datarate of at least $1Gb/s$.
- A high-speed interface that supports interfacing to SSDs.
- Sufficient resources to both control the transfer of data between the mass storage and the processor, uplink and downlink, and to apply error correction algorithms on this data at the highest datarate that the FPGA must be capable of handling. This will be the $1Gb/s$ of the downlink channel.
- A low active and idle power consumption
- The FPGA must be capable of surviving in a harsh space environment.

While it is not within the scope of this work to design and implement the coding and error correction schemes for the lasercom system, an analysis has to be made on possible coding and error correction schemes in order to design a system that is capable of executing these schemes. In order to determine a suitable error correction scheme for the data transmitted over the downlink and the uplink, the proposed coding and modulation standard for optical communication systems in space, as compiled by the CCSDS, can be used. This standard proposes the use of convolutional encoding schemes to allow for error detection and correction on the received data stream [32]. While this is an efficient coding scheme that is simple to implement, decoding of a convolutional code takes a significant computational effort [33]. It is therefore best to apply a convolutional code to the up- and downlink only. Due to the low speed of the uplink, the impact on power consumption due to the decoding of this stream should be minimal.

The buffer data stored in the mass storage will also require some error correcting code to mitigate data corruption due to, for example, radiation effects. Since the storage volume of an SSD is large compared to the minimum required storage volume as described in section 3.1, an efficient choice is to apply an error correcting code that is highly efficient in terms of computational power required for encoding and decoding, and if necessary less efficient in terms of data volume. A commonly used coding scheme is called Single Error Correction, Double Error Detection (SECDED), which is an implementation of Hamming code [34]. This is a simple scheme that allows for efficient encoding and decoding on an FPGA.

An important requirement is that the data flowing through the FPGA has to be encoded or decoded and corrected at the same rate at which this data is presented or requested in order to not create a bottleneck. A SECDED encoder/decoder can be implemented as a parallel operation to allow for a high datarate while still requiring little resources [34]. A convolutional encoder is usually implemented as a serial operation with a low computational cost, but this limits the maximum datarate of this encoder to below the maximum clock speed of the FPGA, which does not allow for data rates of $1Gb/s$. To achieve these datarates a parallel, and if necessary pipelined architecture can be employed for this encoder. In this way data rates of $6.61Gb/s$ have been achieved on an FPGA from 2004 [35]. To achieve $1Gb/s$, approximately

300 logic cells will be required using this architecture, which is still a low number for current-day FPGAs.

The fact that the selected FPGA must survive the harsh environment in space greatly limits the choice for a suitable FPGA, since most FPGAs are SRAM based, and are thus sensitive to Single Event Upsets (SEU). These SEUs cause errors in the configuration of the FPGA which leads to functional interruptions and data loss. A recent family of FPGAs that does not suffer of these issues is the PolarFire family by Microsemi [36]. This FPGA family is flash-based, which gives this FPGA a low idle and active power consumption and immunity to SEU, according to the manufacturer. At the time of writing there is no documentation available to support this claim. Information on total dose effects on the PolarFire FPGAs are also not available. A radiation test will thus be required to verify that these FPGAs are sufficiently immune to SEU- and total dose effects.

Next to this, the PolarFire family of FPGAs offers fast transceiver channels of up to $12.7Gb/s$, 100000 to 500000 logic cells and an integrated PCI Express controller. The datarate supported by the transceivers and the large number of logic cells leaves sufficient margin for future developments on laser communication at Hyperion Technologies. The PCI Express controller is a useful feature, since modern SSDs support the NVMe interface, which is a standardised communication protocol for SSDs that operates on a PCI Express connection [37]. Using the integrated PCI Express controller, the FPGA can interface to an NVMe SSD efficiently with reduced development effort.

Electrically, the SSD interface is relatively straightforward. Laptop-size NVMe SSDs use an M.2 connector which requires four transceiver connections to the FPGA for the PCI Express protocol, a $100MHz$ clock input, a $3.3V$ power input and some low-speed IOs for management purposes [38]. The $100MHz$ clock can also be used as reference clock for the other interfaces of the FPGA, such as the QSPI interface to the processor, an UART interface to receive data from the uplink channel and a transceiver interface to the downlink seed laser driver.

A more complex circuit around an FPGA is usually the power conversion circuit. An FPGA requires different voltages, and each power supply must be capable of supplying the FPGA with large peak powers. At the time of writing no power supply requirements specification is available for the PolarFire family of FPGAs, but using the available documentation for the evaluation kit for this FPGA a design for the power circuitry can be made. The schematics of the evaluation kit contain a power supply design with a voltage and current specification for each rail [39]. It should be noted that that design is sized to supply all peripherals on that board as well. The required supply rails for the FPGA are:

- VDD25: $2.5V, 5A$
- VDD18: $1.8V, 5A$
- VCORE: $1V, 10A$
- VDDA: $1V, 5A$

The specified current limits are high, and are expected to be significantly higher than the power supply current limits that will be required by the lasercom satellite terminal. However, since no further information is available on the power supply requirements of the PolarFire FPGAs, a design has to be made using for these four specified rails. Due to the large peak current consumptions, it is decided to create the FPGA supply voltages directly from the satellite battery voltage instead of from the lasercom terminal digital voltage rail to limit power losses from cascaded power converters.

In order to achieve high power conversion efficiencies, synchronous DC-DC converters are selected. To create all four required voltage rails, two different DC-DC converters are selected. The first one is the MAX17558 from Maxim Integrated Products. This DC-DC converter can supply high output currents in an efficient way due to its two-phase architecture, while still

offering good efficiencies at low loads. This makes this DC-DC converter ideal for supplying both the VDDA and the VCORE rail. The maximum input voltage for this converter is $60V$, but its peak efficiency is achieved at the commonly used battery voltage of $12V$. At an output voltage of $3.3V$ this peak efficiency is given to be 93%, for an output voltage of $1V$ this efficiency will be slightly lower [40]. For the other two $5A$ rails, VDD25 and VDD18, the MAX17232 is selected. This is a similar DC-DC converter as the MAX17558 with a slightly better efficiency, but with a higher minimum output voltage which makes it unsuitable for the $1V$ rails [41].

The MAX17558 and the MAX17232 are both BiCMOS based ICs. While DC-DC converters are usually a risky component to use in space application since the power MOSFETs used in these converters degrade under radiation, up to a point where the DC-DC converter can no longer operate, BiCMOS based devices are known to be highly tolerant to radiation damage [42]. It is therefore expected that these components will be able to pass a radiation test.

A schematic overview of the FPGA segment of the lasercom satellite terminal is given in Figure 25. Since the power consumption of the FPGA depends on the FPGA configuration design, no better power consumption prediction for the FPGA than the values given in section 3.7.5 can be determined. However, including the fact that the power conversion of the power supplies for the FPGA is slightly higher than expected, the FPGA power consumption of $1.8W$ in communication mode and $0.43W$ in buffering mode gives a total power consumption of $1.94W$ and $0.46W$

4.3. Mass storage

In section 3.5.2 it is determined that an SSD will be the optimal choice for the mass storage of the lasercom satellite terminal, and in section 4.2 it is described that a modern NVMe SSD can be interfaced relatively easily to the selected FPGA. The smallest SSDs with an NVMe interface are M.2-format SSDs, designed for use in laptops. This standardised slot only requires a $3.3V$ power input, and can thus be supplied directly by the digital power converter on the lasercom satellite terminal. Since both the electrical interface to an M.2 connector and the software interface to an NVMe SSD are standardised, any M.2 NVMe SSD can be used in the lasercom satellite terminal, increasing the flexibility of the design.

SSDs are not commonly used in small satellite missions, and few radiation test reports on SSDs are available. These reports however indicate mixing results between SSDs from different manufacturers, with some achieving decent radiation performance [43]. A radiation test certainly has to be performed with suitable M.2 NVMe SSDs to find a type with acceptable radiation tolerance.

A reference M.2 NVMe SSD from Samsung has a maximum power consumption of $5.1W$ [15]. For the design of the power conversion circuitry, this value should be included in the sizing of the digital power conversion circuit. The power consumption of the SSD during buffering and during communication will however be lower, since the maximum read speed is specified to be $3500MB/s$. Since the actual power consumption of the SSD depends on the FPGA configuration design, no better power consumption prediction than the values given in section 3.7.5 can be determined.

The SSD mass storage and its connections is included in the schematic overview for the FPGA segment of the lasercom satellite terminal in Figure 25.

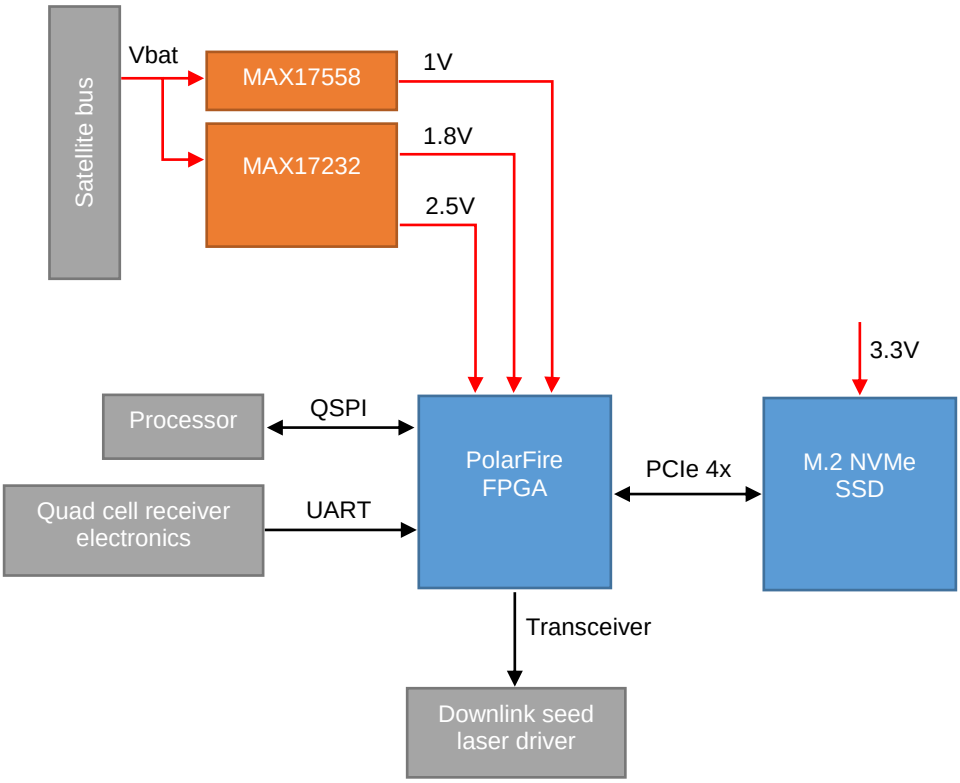

Figure 25: satellite terminal FPGA and SSD segment schematic overview

4.4. Seed laser driver

The seed laser driver converts the electrical signal from the FPGA transceiver to a modulated current pattern. This modulated current is supplied to the seed laser in order to create a modulated optical signal. The seed laser will be a low-power laser diode, supplied for this project by photonics supplier Gooch & Housego. In order to properly drive and modulate a laser diode, its behaviour has to be understood.

A laser diode is not a linear device. For low diode currents the photon output is mainly generated by spontaneous emission. This gives a low optical output power which barely rises with input current. Only above a certain threshold current, stimulated emission starts taking place in the laser diode and the optical output increases rapidly with increasing input current [16]. In order to create a modulated optical output signal, the laser diode current should be modulated between a value at or below the threshold current for no optical output power, and a current level higher than this to create the desired optical output power level. This is illustrated in a simplified manner in Figure 27.

Next to this, an increase in input current does not immediately cause an increase in optical output power. Within a laser diode the diode current create charge carriers, which in turn form photons in the laser diode due to either spontaneous emission or stimulated emission. The photons present in the laser diode cavity however also form new charge carriers in the laser diode. A laser diode is thus governed by two differential rate equations, one for the conversion of charge carriers to photons and one for the conversion of photons to charge carriers [16]. In practice, the result is that laser diodes usually behave as underdamped oscillating systems, as illustrated in Figure 26. In this figure two effects resulting from the two rate equations system can be observed: the turn-on delay t_s and the relaxation frequency f_r. The turn-on delay depends on the design of the laser diode but also on where on the curve of Figure 27 the current levels I_{off} and I_{on} lie: the further I_{off} is below the threshold current I_s, the longer the turn-on delay will be [16].

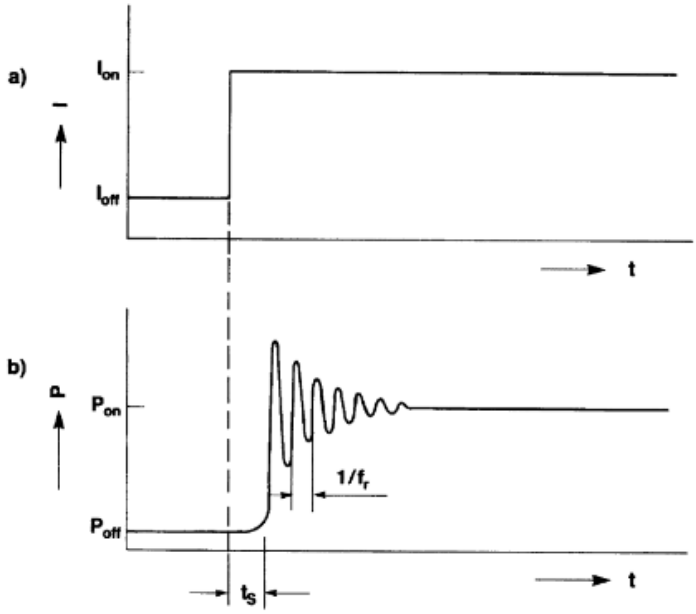

Figure 26: interaction between a) laser diode current and b) laser diode optical output power, from [16]

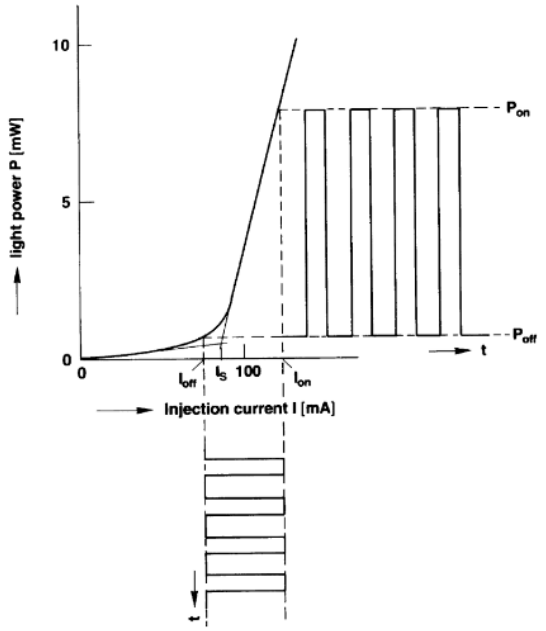

Figure 27: simplified laser diode modulation, from [16]

To properly driver the seed laser at high speeds, the requirements on the seed laser driver are:

- The seed laser driver must drive the laser diode between the threshold current I_s and the required maximum current I_{on} in order to reduce the turn-on delay.
- The transition time of the driver between these two current levels should be low.
- The seed laser that Gooch & Housego will incorporate in the photonics for the satellite lasercom terminal is specified to have an impedance of 50Ω[3], so the seed laser driver should be capable of driving a load with this impedance.
- Using the results from section 3.6.5, the laser driver should be capable of supplying the laser diode with at least an electrical power of $17mW$.

While a seed laser driver based on a standard RF power amplifier would be capable of meeting these requirements, a more efficient solution is to use a dedicated laser diode driver as used in the telecommunication industry. The required output impedance of 50Ω limits the number of commercially available laser driver, but the MAX3795 meets the requirements of the lasercom satellite terminal well. This laser driver is capable of supplying up to $15mA$ bias current and $15mA$ modulation current to a 50Ω load, which for a laser diode forward voltage of $2.3V$ gives a maximum total seed laser power of $80mW$. The maximum total power consumption for this driver, including the power supplied to the seed laser, is specified to be $333mW$ [44].

Next to this this driver integrates a seed laser output power monitor input, which can be used to automatically adjust the bias current level to be equal to the laser diode threshold current I_s. The transition time of the driver between the low and high output current levels is short, and the turn-on delay of the laser diode can be further reduced by this driver by using the optional

[3] Confidential communication with Gooch & Housego, 9-1-2018

peaking current, which supplies some additional current to the laser diode at a level transition. The data input to this laser driver can be connected directly to the FPGA transceiver output.

Just like the DC-DC converters for the FPGA power supplies, the MAX3795 is based on a BiCMOS process. It is therefore assumed that this component will be able to pass a radiation test.

A schematic overview of the seed laser driver segment of the satellite terminal is given in Figure 28.

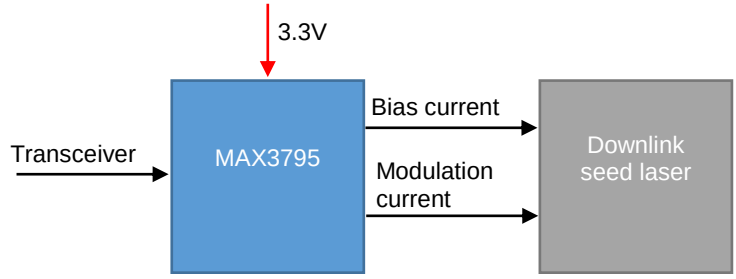

Figure 28: seed laser driver schematic overview

4.5. Optical amplifier driver

The optical amplifier is a high-power laser diode that must be driven by a constant current. As determined in section 3.6.5, the total input power to the optical amplifier will be $4.4W$. Assuming a common diode forward voltage of $2.3V$, the optical amplifier current will be $1.9A$. To allow for uncertainties in the optical amplifier forward voltage and to allow for an increase in optical amplifier current to mitigate the effects of aging, the optical amplifier driver will be sized for $2.5A$. The optical amplifier current level should be adjustable as well to be able to select the optimal drive current. Since this is such a significant power consumption, the most efficient option is to supply the optical amplifier directly from the satellite battery voltage. This does mean that the optical amplifier driver should support a wider range of input voltages, but it prevents a design with cascaded power converters and thus reduces power losses considerably.

DC-DC converters are not commonly designed for constant current applications, but one DC-DC converter that allows for an efficient constant-current design is the LM5117 from Texas Instruments. The current output from this converter can be adjusted using an analog voltage. With an input voltage of $12V$ and an output voltage of $2.3V$, the efficiency of this converter is approximately 91% [45].

It is not known on what technology this controller is based, or how it responds to radiation. Since this is a DC-DC controller, the power MOSFETs are external to this IC, power MOSFETs can thus be selected that are known to be radiation tolerant which at least reduces the technical risks involved in using this controller. It will however be necessary to perform radiation testing on this component to verify its behaviour under radiation.

A schematic overview of the optical amplifier driver segment is given in Figure 29.

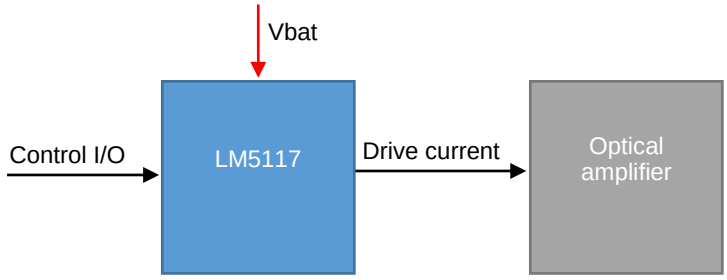

Figure 29: optical amplifier driver schematic overview

4.6. Quad cell receiver

The quad cell receiver measures, based on the photocurrents collected by the quad cell sensor, what the angle of incidence is of the received uplink beacon light. Next to this the quad cell receiver circuit must convert the received modulated photocurrent signals to a data stream. The requirements on the quad cell receiver are mainly driven by the results from chapter 0:

- The quad cell sensor must have a diameter of $1mm$
- The quad cell receiver electronics must be designed for a quad cell sensor with a dark current of $180pA$ and a shunt resistance of $50M\Omega$.
- The quad cell receiver electronics must be able to perform their functions with a background light level of $10nW$.
- The quad cell receiver electronics must have a bandwidth of at least $100kHz$ in order to receive OOK-modulated data at $200kb/s$.
- The quad cell receiver electronics must have a maximum input-referred output noise per channel of $95pA$ at this bandwidth.
- The input-referenced noise per channel as used for the calculation of the angle of incidence must be $1pA$ or less.
- The maximum gain error between any two channels must be less than 1%.
- The maximum offset error between any two channels must be less than $10pA$.

The photocurrent generated by the quad cell sensor consists roughly of two contributions, the almost constant contributions from the dark current of the quad cell sensor and the background light, and the high-frequency component of the modulated uplink signal. The detection of the modulated uplink signal can therefore be done in a relatively simple way, by performing a high-pass filtering operation on the received photocurrents. In this way only the modulation signal remains. The high-passed signals from each quadrant can now be added so that the quad cell receiver electronics can demodulate the uplink data stream irrespective of which portion of the received uplink light falls on which quadrant.

The quad cell receiver measures the angle of incidence of the received uplink beacon light by determining the displacement of the projected dot, as described in section 3.6.3. A displacement of the projected dot causes a change in the total amount of light received by each quadrant: if the projected dot moves to the left, the two leftmost quadrants will receive more light and thus generate a larger photocurrent and if the projected dot moves down, the two lower quad cell quadrants will generate a larger photocurrent. Using the definitions from Figure 30 and theory taken from [46], the position of the projected dot relative to the centre of the quad cell sensor can be written as:

$$x_{dot} = \frac{(I_2 + I_4) - (I_1 + I_3)}{I_1 + I_2 + I_3 + I_4} \tag{37}$$

$$y_{dot} = \frac{(I_1 + I_2) - (I_3 + I_4)}{I_1 + I_2 + I_3 + I_4} \tag{38}$$

The quad cell receiver electronics therefore must determine the photocurrent in each quadrant in order to calculate the projected dot position. The contribution of background light however could cause a significant error in determining this position: if some quadrants receive more background light than other quadrants, which is likely given that the background light can come from all directions and is not necessarily uniform, this will contribute directly to an error in the calculated projected dot position.

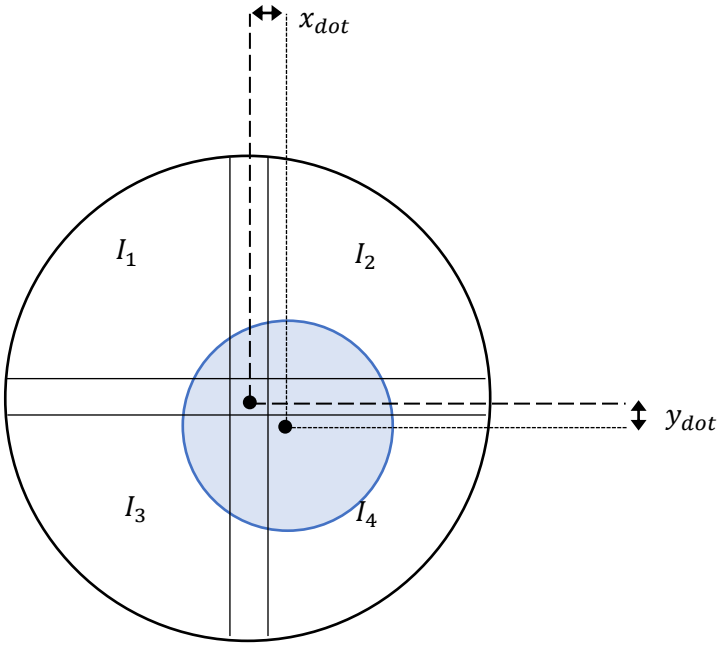

Figure 30: Geometry and definitions for the determination of the projected dot position on the quad cell sensor

The fact that the uplink beacon light is modulated can be used to mitigate this issue. The high-pass filtered signal as is used for the demodulation of the beacon signal can also be used to determine the photocurrent due to just the beacon light in each quadrant, since the amplitude of the high-pass filtered signal for each quadrant depends on the total beacon light power in that quadrant. In the example of Figure 30, the amplitude of the high-pass filtered photocurrent from segment I_4 will be larger than the amplitude from segment I_1. The process of determining the amplitude of each high-pass filtered signal can be done using the classic methods of AM-demodulation as illustrated in Figure 31.

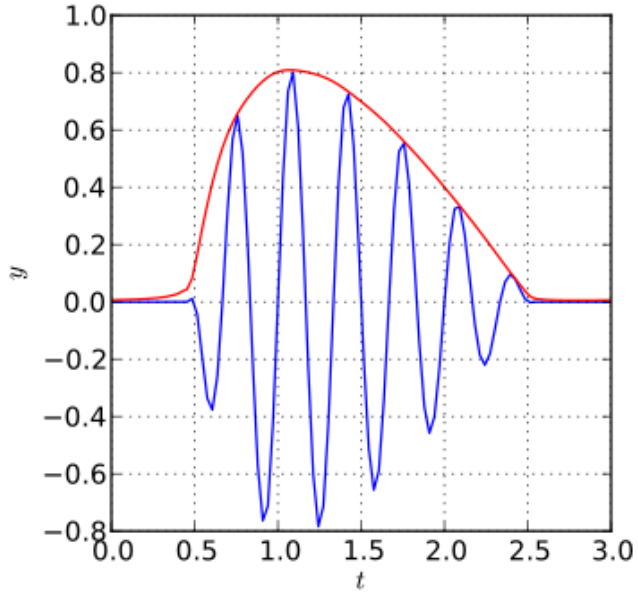

Figure 31: Principle of AM demodulation, from [47]

The maximum frequency present in this signal is equal to half the uplink bitrate of $200kb/s$. If a data pattern of "1010" would be transmitted, where a "1" is represented by the beacon light source being on and a "0" with the beacon light source off, as is used in On Off Keying (OOK) modulation, if this data stream is transmitted at $200kb/s$, the resulting optical modulation pattern will be a square wave with a frequency of $100kHz$. Data patterns with equal consecutive bits, such as "1100", will also give lower-frequency components in the data signal. The cut-off frequency of the high pass filter that is applied on the signal from each quadrant must be lower than the lowest frequency present in the modulated beacon light signal, in order not to degrade this signal. In a random data pattern, any length of equal consecutive bits can be encountered which would give the uplink beacon signal an infinitely low minimum frequency component. The minimum frequency component present in the beacon signal can be constrained by using a coding technique, such as 8B/10B coding. If a data stream is encoded using this technique, every 8 bits will be represented by 10 bits. This 10-bit word is guaranteed to have no more than 5 equal consecutive bits [48], which constrains the minimum frequency component present in this signal to 1/5th of the highest frequency present in the beacon signal. For the quad cell receiver electronics, this means that the high-pass filter must have a cut-off frequency below $20kHz$.

The photocurrents generated by the quad cell sensor are very small, as determined in section 3.7.5. While usually the goal of an electronic amplifier stage is to amplify a signal as much as possible up to the required bandwidth with as little noise as possible, for the quad cell receiver electronics it is also essential that the errors in the measured signal amplitudes between all quadrants are minimal. To achieve this, the following design goals for the quad cell receiver electronics can be identified:

- To amplify the quad cell sensor photocurrents with little added noise.
- To minimise the difference in gains between all channels.
- To minimise the offsets between all channels
- To minimise the difference in signal distortion between all channels to give an equal waveform shape for all channels, or to minimise the dependency of the AM-demodulation circuit on the precise waveform shape.

To amplify small current signals transimpedance amplifiers are commonly used. These amplifiers convert a current signal at the input to an amplified voltage signal at the output.

While different amplifying components can be used, an opamp-based circuit has the advantage that its gain is determined solely by the selected feedback resistance value, while generally also offering a low power consumption. A basic opamp-based transimpedance circuit is illustrated in Figure 32.

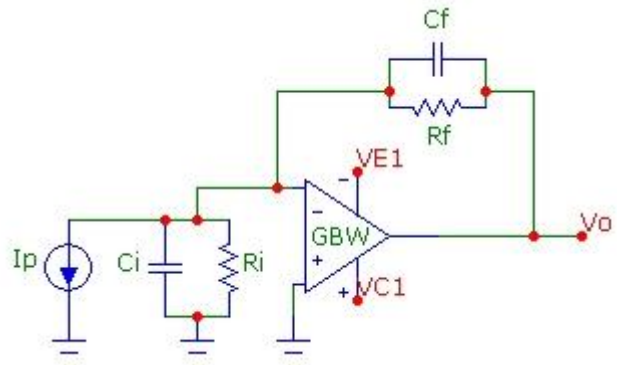

Figure 32: basic opamp-based transimpedance circuit, taken from [49]

The selection of the opamp used in the transimpedance stage is an important consideration, since the performance of the transimpedance amplifier (TIA) mainly depends on the opamp performance characteristics. The major noise contributions in a TIA are the feedback resistor thermal noise, since this is usually a large resistor, the opamp voltage noise e_n and the opamp current noise i_n [49]. The feedback resistor contributes noise according to the well-known Johnson noise equation:

$$V_n^{out} = \sqrt{4k_B T R \Delta F} \tag{39}$$

Where k_B is Boltzmann's constant, T is the temperature of the resistor, R is its resistance and ΔF is the bandwidth over which this noise is integrated. For the feedback resistor in the TIA circuit this bandwidth is equal to the bandwidth of the TIA. Since the gain of an opamp-based TIA depends linearly on the value of R_f,

$$V_O = I_p R_f \tag{40}$$

And the noise contribution of the feedback resistor depends on the value of R_f by a power of ½, increasing the value of R_f gives a better signal-to-noise ratio. The maximum gain that an opamp-based TIA can support is however limited by the Gain Bandwidth product (GBW) of the selected opamp [49]. An opamp must therefore be selected with a high GBW, a low voltage noise, and a low current noise. This opamp should also be capable of surviving in space.

The best performing opamp for this usecase is determined to be the AD8655 from Analog Devices. This opamp is found to offer the lowest combination of voltage noise and current noise at a voltage noise of $2.7nV/\sqrt{Hz}$ and no measureable current noise, while still achieving a GBW of $28MHz$ at a current consumption of $4.5mA$ [50]. The radiation performance of this component is unknown, but a similar component, the AD8661, has been radiation tested. For this component it was found that after 13krads(SI) functional failure occurred [51]. A radiation test of the AD8655 will be necessary to determine whether it is capable of surviving in space.

It is described in [49] that a TIA circuit noise consists mainly of the voltage noise from the opamp, which is strongest in the output signal around the corner frequency of the TIA, f_{3dB}. After the TIA stage, the signal level will still be too low for further processing, so an additional voltage amplifier stage will be necessary to amplify the measured signal to sufficient levels. This voltage amplifier can be constructed to low-pass filter the amplified signal at the same

time to reduce the influence of the TIA noise above the signal frequency of interest, which is $100kHz$ in this case.

A voltage amplifier with low-pass filtering capabilities can be constructed using an opamp in the Sallen-Key topology, as described in [52]. To perform this function the same opamp as for the TIA can be used, the AD8655.

Because one of the design goals for the quad cell receiver electronics is to minimise the offsets between all channels, the high-pass filtering operation can be constructed using a DC-nulling circuit. Such a circuit works as an integrator to accurately correct a voltage level, until the DC component of the signal is equal to a reference voltage. This principle is illustrated in Figure 33, where an opamp-based integrator, U2, is used to create the reference voltage for the feedback network of the voltage amplifier U1. The integrator will adjust its output voltage until the DC-component of the output signal is equal to reference voltage Vref. The integrator opamp U2 does not have to be fast, but it must have a negligible offset voltage. For this function the AD8628 from Analog Devices is selected. This device features an offset voltage of $1\mu V$, an offset voltage drift of $0.002\mu V/℃$ and a current consumption of $1mA$ [53]. A space variant of this device exists, the AD8629S, which is known to be radiation-tolerant, so it is assumed that the regular AD8628 will be able to pass a radiation test.

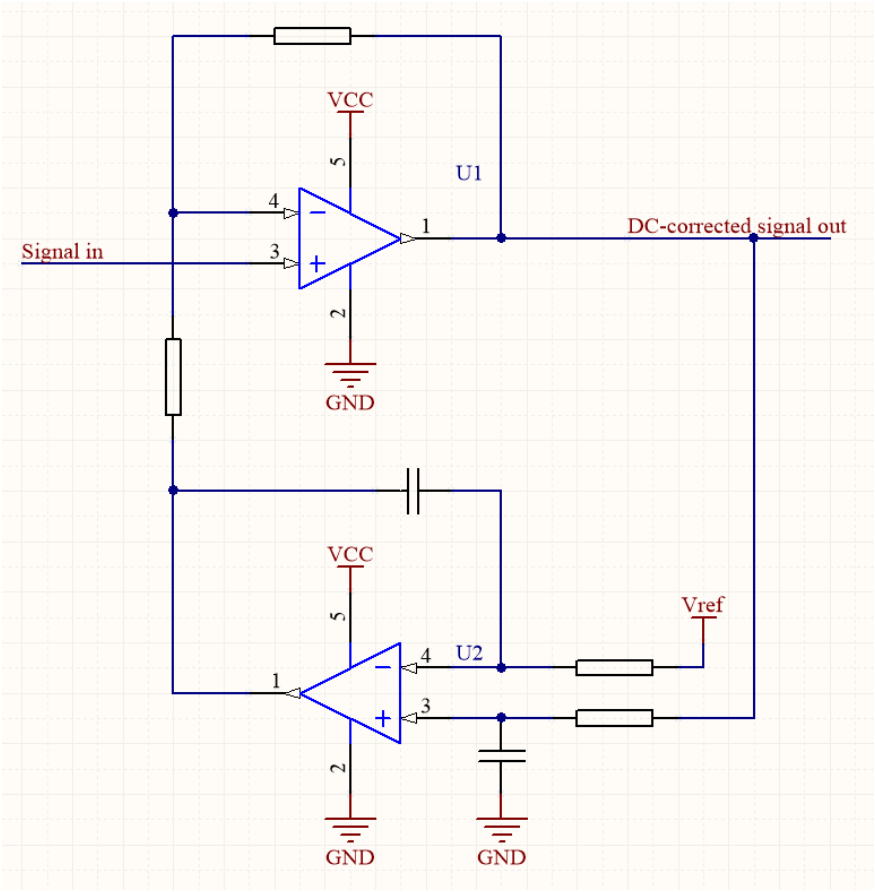

Figure 33: DC-nulling configuration using opamp U2 as integrator

After the photocurrent signals from the quad cell sensor have been amplified, low-pass filtered, and low-frequency components and offsets have been removed from these signals, what remains is the uplink data signal. Since this data signal will be divided over the four quadrants, all four amplified and filtered signals have to be summed to arrive at a single uplink data signal. This can be performed by an opamp-based summing amplifier, as illustrated in Figure 34. For the opamp the same AD8628 can be used as for the DC-nulling circuit, since this opamp is

fast enough to operate as a summing amplifier in this application, while its power consumption is much lower than that of the AD8655 used in the rest of the quad cell receiver circuit.

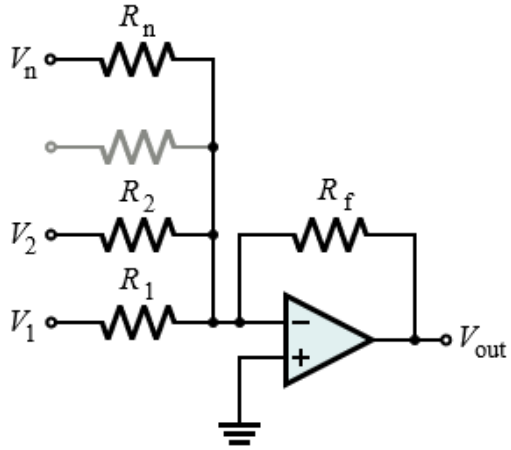

Figure 34: opamp-based summing amplifier, from [54]

The next step is to perform AM-demodulation on the amplified and filtered signals to determine the signal amplitude from each quadrant. While in classic AM-radios this is done using a diode and a capacitor, the difference in forward voltage of the diode in each channel will cause an offset error between the channels for the determination of the signal amplitude in each quadrant. This is therefore a less favourable solution. Two different methods for determining the amplitude of the amplified signal can be used:

- An opamp-based envelope detector circuit. In terms of functionality this circuit is similar to the classic combination of diode and capacitor, but an opamp is used to emulate a perfect diode with no forward voltage, thereby mitigating the disadvantage of that solution. This circuit is illustrated in Figure 35.
- A rectifier circuit. This circuit converts an AC voltage to a DC voltage. Usually this is done to convert an AC power input to a DC power level, but the same method can be used to measure the amplitude of a signal, since this DC voltage level depends on the AC signal amplitude. While a regular rectifier circuit based on diodes is again sensitive to the precise diode characteristics, an opamp-based rectifier circuit can be constructed that does not suffer from this disadvantage. The rectified signal can then be filtered by a low-pass filter stage to arrive at an AM-demodulated signal. This circuit is illustrated in Figure 36.

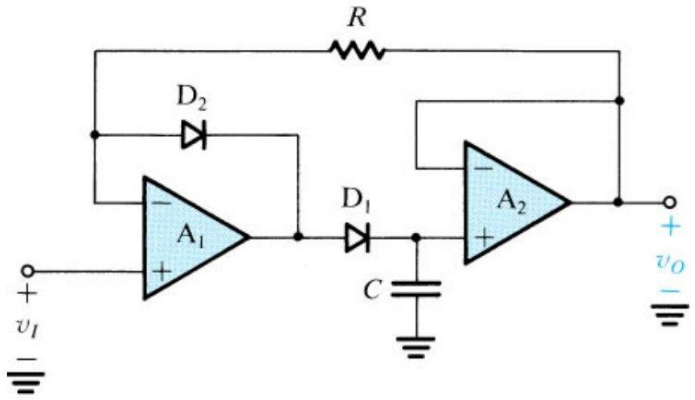

Figure 35: opamp-based envelope detector, from [55]

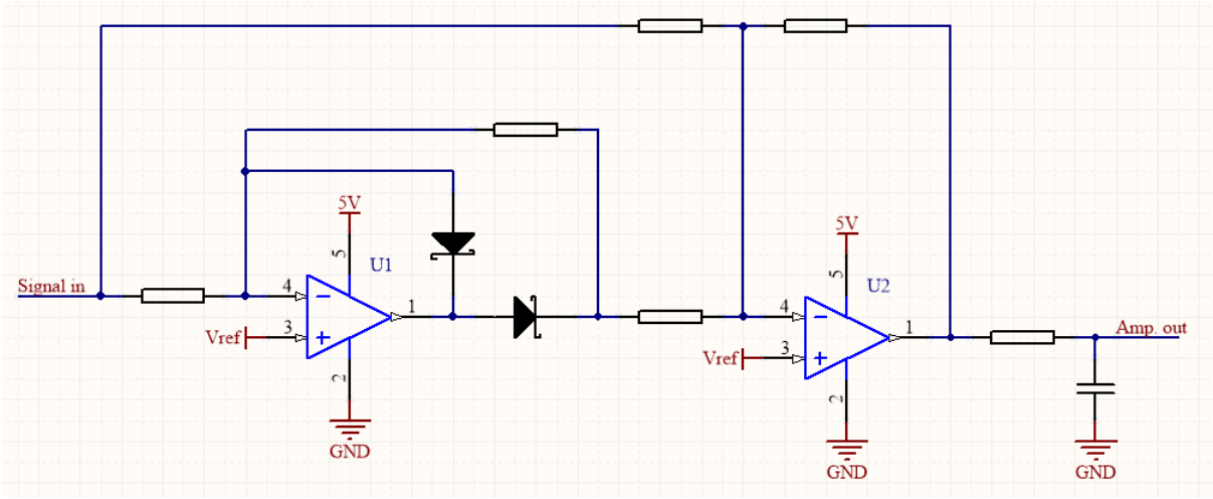

Figure 36: opamp-based rectifier with low-pass filtered output signal

It can be observed in Figure 35 and Figure 36 that those circuits are quite comparable. An important difference however is that the opamp-based envelope detector must be able to drive its output past the diode forward voltage quickly without overshooting too much in order to charge capacitor C precisely to the voltage level present at the input in case this voltage is higher than the voltage across capacitor C. This requires a fast opamp for opamp A1. In an opamp-based rectifier opamp U1 does not have to quickly charge a capacitor, this opamp will follow the input voltage as long as the input voltage is lower than the reference voltage, which means that this opamp only has to be fast enough to follow the input signal, which for the quad cell receiver is a signal of $100kHz$. The faster an opamp is, generally the larger its power consumption is. For this reason the opamp-based rectifier circuit is assumed to be the best choice for the quad cell receiver circuit, built with the same AD8655 opamps as used in the TIA and the filter stage.

The computation of the projected dot position using equations (37) and (38), and the corresponding received beacon light angle of incidence, can be performed best by a low-power microcontroller. Many microcontrollers with high-performance ADC converters also exist, which is useful for converting the output signal from the AM demodulator to a digital value for each channel and performing all necessary computations in a single chip, after which the angle measurement result can be forwarded to the main processor in the lasercom satellite terminal. The microcontroller that is selected for this task is the ATxmega64A4U from Atmel.

The AD8655 and the AD8628 can both operate on supply voltages from $2.7V$ to $5V$. Since the ADC noise and offset errors for the ATxmega64A4U are specified irrespective of the used reference voltage and supply voltage [56], the best ADC conversion signal-to-noise ratio is achieved when a large amplitude signal is supplied to the ADC. The maximum signal voltage from the opamp stages is possible when these stages are supplied with $5V$, which gives a maximum output signal amplitude of $2.5V$ around a center voltage of $2.5V$. If the rectifier circuit then outputs the values of this signal below the reference voltage of $2.5V$, as the circuit in Figure 36 is configured to do, the input voltage to the ADC will be between $0V - 2.5V$. This fits well with the digital supply voltage of $3.3V$ for this microcontroller.

Since the proposed quad cell receiver circuit is not a standard circuit, its precise performance and power consumption cannot be determined from literature alone. Based on the selected active components, with four AD8655 opamps and one AD8628 per channel running on $5V$, and an ATxmega64A4U microcontroller running at $3.3V$, an estimation of the power consumption of the quad cell receiver can be made. This estimation is given in Table 11, the mentioned current consumptions are the typical current consumptions at these conditions taken from [53], [50] and [56]. An overview of the quad cell receiver circuit is given in Figure 37.

Table 11: quad cell receiver electronics power consumption estimation

Component	Operating voltage	Operating current	Quantity	Power consumption
AD8655	$5V$	$4.5mA$	17	$382.5mW$
AD8628	$5V$	$1mA$	4	$20mW$
ATxmega64A4U	$3.3V$	$12mA$	1	$40mW$
				$442.5mW$

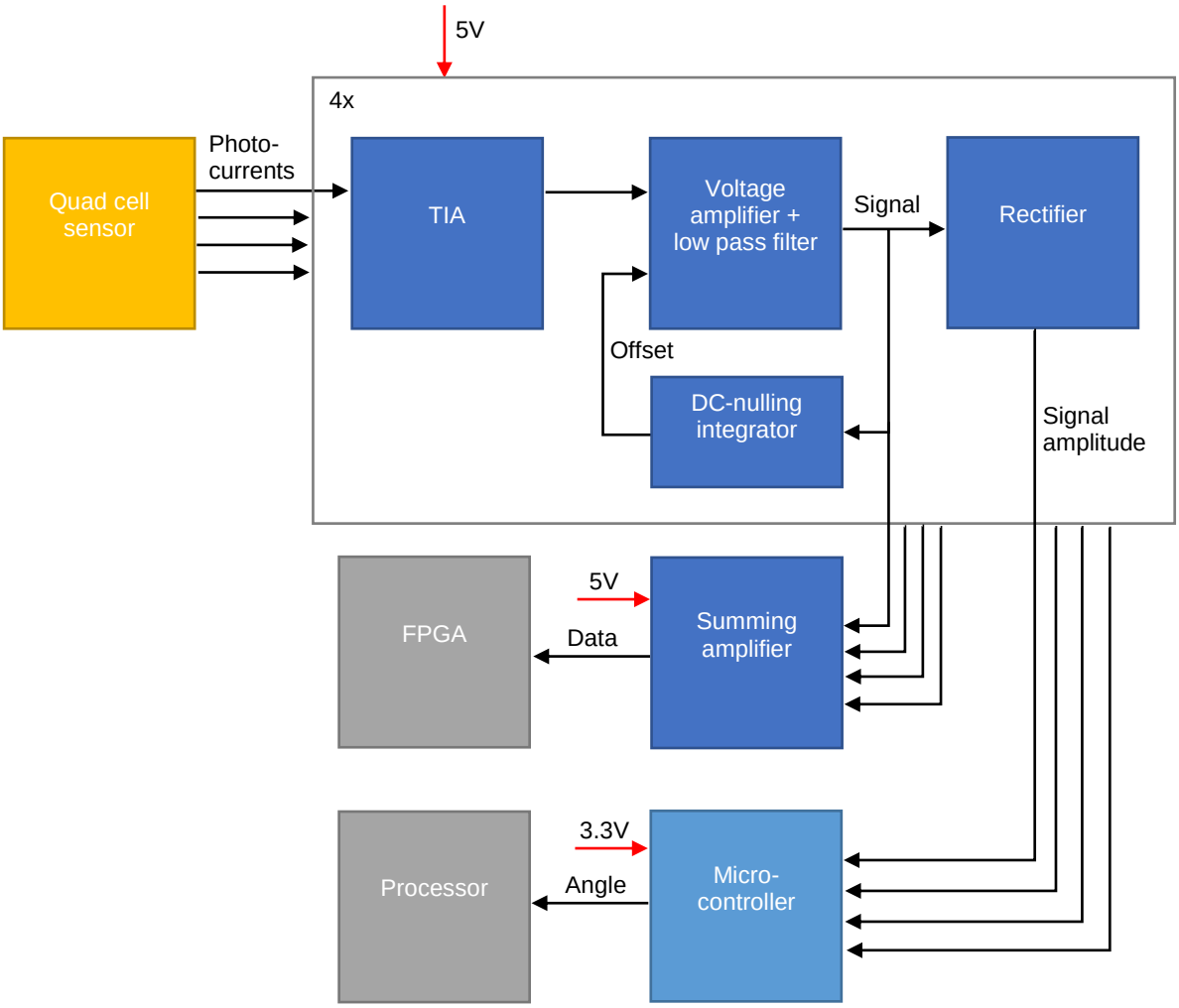

Figure 37: quad cell receiver electronics schematic overview

4.7. Power conversion

The power conversion circuit should convert the battery voltage from the CubeSat bus to usable voltage levels for the other electronic components. Two voltage levels are required: $3.3V$ for the digital circuits, and a low-noise $5V$ for the analog electronics in the quad cell receiver. The maximum current usage on the digital supply line is found by adding the maximum operational current consumption of each component on the $3.3V$ line and consists of:

- Processor (incl. CAN transceiver): $280mA$
- SSD: $1.8A$
- Seed laser driver: $101mA$

- Quad cell receiver digital electronics: $12mA$

The sum of these values gives a maximum current consumption of $2.19A$ on the $3.3V$ line. To maintain sufficient margin in the design of the digital power conversion circuit to allow for transients and component aging, the maximum current rating for the digital power conversion circuit is set at $2.5A$.

The analog voltage line is only used by the quad cell receiver electronics. The current consumption on this line is determined to be $80.5mA$, including a margin the analog power conversion circuit current rating should be set at $100mA$. Since an important requirement is that the voltage on this line must contain little noise, a Low Dropout Regulator (LDO) must be used to create this $5V$ line. Unfortunately, an LDO requires an input voltage that is higher than its output voltage, and the only voltage rail in the lasercom satellite terminal that is higher than $5V$ is the battery voltage line. LDOs that are optimised for low output noise usually have a low maximum input voltage which is lower than common CubeSat battery voltages. A different architecture is therefore proposed, where first a DC-DC converter is used to convert the battery voltage to an intermediate voltage, after which an LDO will create the low-noise $5V$ line.

To create both the $3.3V$ and the intermediate voltage the same DC-DC converter as used for powering the FPGA can be used, the MAX17232, since this is a dual-output converter. As an LDO the MAX8902 can be used. This device has a low quiescent current consumption of $80\mu A$, its output voltage noise is specified as $16\mu V_{rms}$ and in contrast to many other low-noise LDOs, it is capable of supplying an output voltage of $5V$ [57]. The maximum input voltage of this device is specified to be $5.5V$, so by giving it an input voltage of $5.3V$, a safe margin is maintained from its maximum input voltage rating, while still offering sufficient voltage difference for this LDO to meet its noise rejection specifications. Since all current drawn at the input of the LDO is equal to the current drawn by the load connected to the LDO, where the difference in power due to the difference in voltage is dissipated by the LDO.

The efficiency of the LDO can therefore be written as $\eta_{LDO} = \frac{V_{out}}{V_{in}}$, where the current consumption due to the small LDO quiescent current consumption is ignored. For this design this gives an LDO efficiency of 94%. The efficiency of the MAX17232 depends on the specific operating conditions such as input voltage and output current, but for an input voltage of $14V$ which is representative of a common battery voltage level, the conversion efficiency is specified to be 90% for a wide range of output currents [41]. For the analog voltage line the efficiencies of the DC-DC converter and the LDO have to be multiplied to give a total conversion efficiency of 85%.

Just as is described for the MAX17232 in section 4.2, the MAX8902 is a BiCMOS-based IC. It is therefore assumed that this component will be able to pass a radiation test.

A schematic overview of the power conversion segment of the lasercom satellite terminal is given in Figure 38.

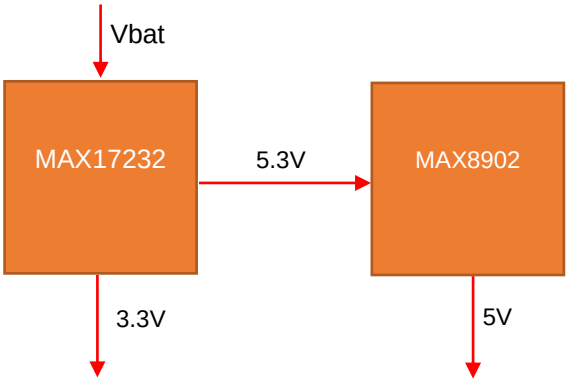

Figure 38: power conversion electronics schematic overview

4.8. Detailed design performance overview

In the previous sections a detailed design is proposed for each segment of the lasercom satellite terminal as illustrated in Figure 17. With these designs, a system can be constructed that achieves the desired performance as determined and calculated in section 3.7.5. Now that a detailed design has been established, a more accurate estimation of the power consumption of the lasercom satellite terminal can be made. In the same way as with Table 6, an overview of the power consumption of all components of the lasercom satellite terminal is given in Table 12. The power consumptions mentioned in this include:

- A 90% power conversion efficiency for the digital voltage line
- An 85% power conversion efficiency for the analog voltage line
- A 93% power conversion efficiency for the FPGA voltage lines
- A 91% power conversion efficiency for the optical amplifier driver

The power consumption for the optical amplifier driver is based on the required optical output power as determined in section 3.7.3. Although the power consumptions given in Table 12 are more accurate than the estimations from Table 6, some uncertainties remain. A major uncertainty is the actual power consumption of the combination of FPGA and SSD, since the power consumption for these two components depends greatly on the specific FPGA configuration design, which is not within the scope of this project. Another, smaller, uncertainty is the power consumption for the processor since this depends on the specific implementation of the software design for this processor.

Table 12: Detailed electronic design power consumption overview

Component	Power consumption buffering	Power consumption communication
Photonics (incl. drivers)	-	$5.17W$
Quad cell receiver electronics	-	$0.52W$
Processor	$0.18W$	$0.62W$
FPGA	$0.46W$	$1.94W$
Mass storage	$0.06W$	$0.44W$
	$0.7W$	$8.69W$

5 Experimental validation of the quad cell receiver

In the introduction of chapter 0 an overview is given of the current state of art on the use of the proposed technologies for the lasercom system in a CubeSat. It was concluded that the greatest uncertainties lie in the application of an SSD in a CubeSat and in the design of a quad cell receiver circuit with specifications as outlined in chapter 0. It is described in section 4.3 that almost no radiation data is available on commercially available SSDs, which is necessary to determine their suitability for use in a CubeSat. The technical characteristics of an SSD are however well known since these are specified by their manufacturers. The quad cell receiver circuit on the other hand has to be designed specifically for the lasercom satellite terminal in order to meet the requirements on this circuit as established in section 3.7.5. Up to a certain level, the circuit design presented in section 4.6 can be modelled analytically or computationally to determine whether these requirements are met, but since this circuit is not prohibitively expensive to build and test, it is decided that an experimental validation is the best way to determine the actual performance of the proposed circuit design.

In this chapter the detailed design as described in section 4.6 will be worked out in further detail in order to construct a prototype. A test plan for this prototype is presented, along with the experimental results obtained in these experiments.

5.1. Prototype circuit construction

Based on the results from section 4.6 a prototype for the quad cell receiver circuit is constructed. For each stage of the quad cell receiver circuit a description is given on how this circuit is implemented in order to meet the requirements on the quad cell receiver as determined in section 3.7.5. To summarise, these requirements are:

- The quad cell sensor must have a diameter of $1mm$
- The quad cell receiver electronics must be designed for a quad cell sensor with a dark current of $180pA$ and a shunt resistance of $50M\Omega$.
- The quad cell receiver electronics must be able to perform their functions with a background light level of $10nW$.
- The quad cell receiver electronics must have a bandwidth of at least $100kHz$ in order to receive OOK-modulated data at $200kb/s$.
- The quad cell receiver electronics must have a maximum input-referred output noise per channel of $95pA$ at this bandwidth.
- The input-referenced noise per channel as used for the calculation of the angle of incidence must be $1pA$ or less.
- The maximum gain error between any two channels must be less than 1%.
- The maximum offset error between any two channels must be less than $10pA$.

5.1.1. Quad cell sensor

Since the beacon will emit light at a wavelength of $1550nm$ as described in section 3.7.3, a quad cell sensor must be selected that is capable of detecting light at this wavelength. These sensors are not commonly available and probably expensive. To determine the performance of the quad cell receiver circuit with respect to the requirements mentioned above however, it is not necessary to use an actual quad cell sensor. Four separate photodiodes with similar characteristics as a quad cell sensor can be used as well. A commercially available InGaAs quad cell sensor that is sensitive at $1550nm$ with a diameter of $1mm$ is the G6849-01 from Hamamatsu [20]. The terminal capacitance of this quad cell sensor is specified to be $30pF$ per quadrant but this capacitance can be decreased considerably by applying a reverse voltage over this quad cell sensor. At a reverse voltage of $1V$ the terminal capacitance is reduced to $15pF$, at a reverse voltage of $3V$ a terminal capacitance of $12pF$ remains. For each quadrant a photodiode with a similar capacitance is used in the experimental setup.

5.1.2. TIA stage

As described in section 4.6, a TIA stage based on the AD8655 opamp will be constructed. This circuit is illustrated in Figure 39. The cathodes of the four photodiodes that together emulate the quad cell sensor are connected to the $5V$ supply line through a low-pass filter with a low $-3dB$ frequency of $48Hz$ as calculated using the standard RC filter equation,

$$f_{-3dB} = \frac{1}{2\pi RC} \tag{41}$$

This should provide enough attenuation of any noise present on the $5V$ supply line to be negligible in the pass-band of the filtering stage. In order to create a reverse voltage across the photodiode, a reference voltage is supplied at the non-inverting input of the AD8655 opamp. It should however be noted that the output swing of the TIA is limited by this reference voltage: if no photocurrent flows through the photodiode, the output voltage of the TIA will be equal to the reference voltage. Since a TIA is an inverting amplifier, the output voltage of the TIA, assuming DC currents and voltages, can be written as:

$$U_{out} = V_{ref} - I_{photo}R_f \tag{42}$$

Where in reality the lower supply voltage of the opamp determines the minimum U_{out} value. For this reason a reverse voltage of $1V$ is selected, as it is determined that for the selected quad cell sensor this voltage gives a significant reduction in photodiode capacitance, whereas higher reverse voltages give a limited decrease in capacitance with a further reduction in output voltage swing. The reference voltage is therefore selected at $4V$.

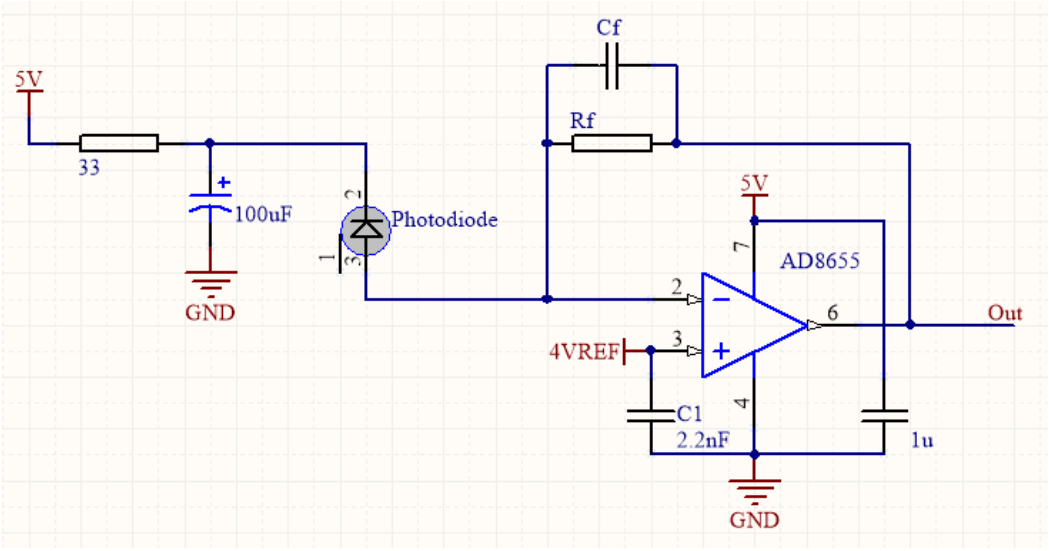

Figure 39: TIA stage circuit design

It is described in section 4.6 that the maximum performance of this TIA stage is achieved for the highest feedback resistance R_f for which the TIA is still capable of reaching the required bandwidth. Since, in order to accurately determine the amplitude of the received beacon signal for each quadrant, it is beneficial that the same signal amplitude is visible at the output of the amplifier stages irrespective of the input signal waveform, the required amplifier bandwidth should be set well above the highest signal frequency of $100kHz$ in order to minimise attenuation and distortion at the highest signal frequency. In [49] an analytical method for determining the optimal values for R_f and C_f is proposed, but this method assumes an ideal opamp and in the datasheet of the AD8655 nonlinear effects can be observed around the unity gain bandwidth of this opamp [50]. For this reason the highest value for R_f for which this TIA can accurately pass the amplitude of a $100kHz$ square wave with no overshoot will be determined using a simple SPICE analysis, under the assumption that the SPICE model for the AD8655 will be more accurate than a simple analytical analysis.

Using the SPICE simulation tool ADIsimPE the circuit in Figure 39 is simulated. For the photodiode a total shunt capacitance of $20pF$ is assumed to include parasitic capacitance in the physical construction of this circuit. The desired output waveform of Figure 40 contains the responses of the TIA output signal for square waves of $50kHz$ and $100kHz$. It can be observed that the amplitude of the output signal at an input signal of $100kHz$ is negligibly lower than that for a $50kHz$ input signal, thereby facilitating the AM-demodulation of the received beacon signal. This response is achieved for an R_f value of $2M\Omega$ and a C_f value of $0.7pF$. The integrated output noise is simulated to be $120\mu V$ RMS. This value of R_f gives a TIA gain of $2 \cdot 10^6$, the maximum input photocurrent per channel before the TIA saturates is therefore $2\mu A$. This is well above the expected background light levels and expected beacon light photocurrent, so output saturation should not be an issue.

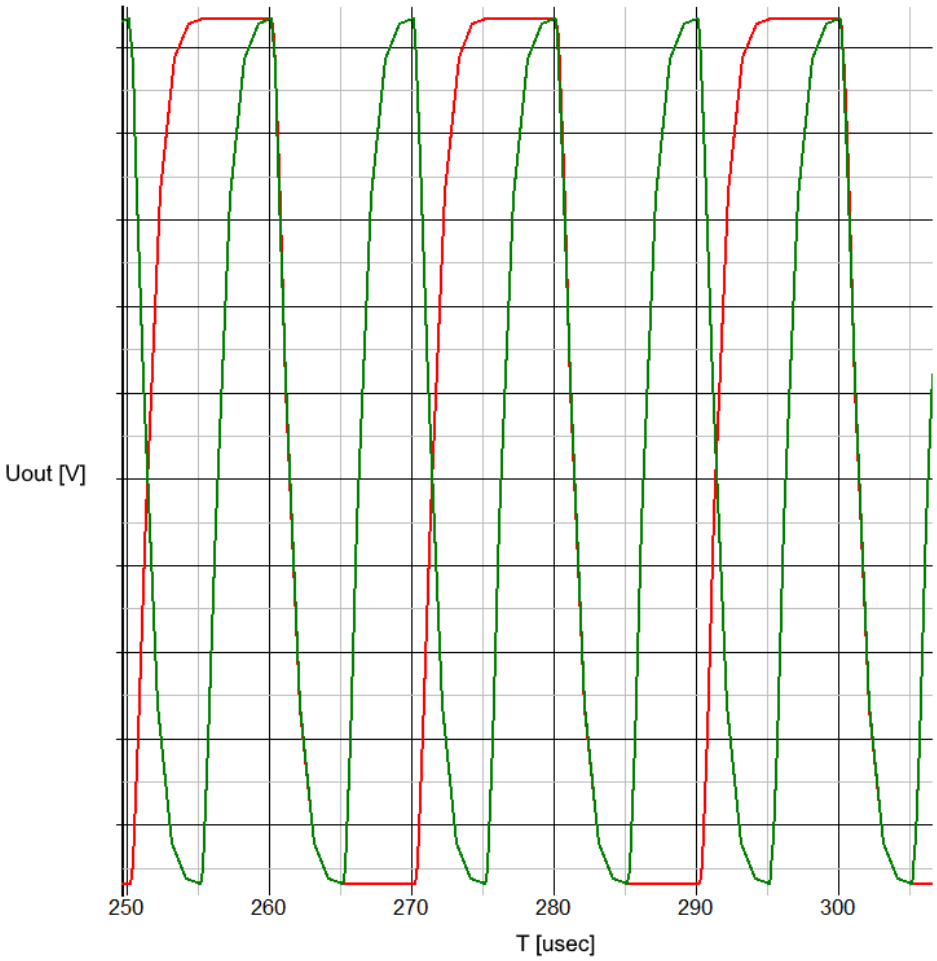

Figure 40: SPICE simulation of the output signal from the TIA, for a 50kHz square wave input (red) and a 100kHz square wave input (green)

5.1.3. Filtering stage

In section 4.6 it is concluded that a voltage amplification stage will be necessary to amplify the received uplink signal to a level that is sufficient for analog-to-digital conversion. The specified maximum input-referenced output noise per channel for the angle measurement of $1pA$ must be well above the resolution of the ADC in order not to have the ADC limit the performance of the quad cell receiver circuit. An additional gain of 100 gives a total gain of $2 \cdot 10^8$, which with an input-referenced noise per channel for the calculation of the angle of incidence of $1pA$ gives a noise voltage of $0.2mV$ at the input of the ADC. However, with this gain an input photocurrent signal of $25nA$ already causes saturation of the filtering stage. Under optimal operating conditions, this value could be achieved in the lasercom system. In order to prevent a loss of angle measurement capabilities in this situation, a switchable gain can be implemented in the filtering stage in order to reduce the filtering stage gain in optimal conditions.

In order to maintain a sufficient margin, the switchpoint for the switchable gain is selected at an input signal of $20nA$. This corresponds to an output signal swing of $4V$. As computed in section 3.7.5, the worst case convertible light power is determined to be $1.3nW$. With the quad cell responsivity of 0.95, this corresponds to a photocurrent signal of $0.3nA$ per quadrant. With the baseline gain of $2 \cdot 10^8$ this corresponds to an output signal of $60mV$. Assuming that at the gain switching point of $20nA$ the input signal must be amplified to the same output signal level in order to arrive at a similar angle measurement accuracy in this situation, the second gain level of the filtering stage should be approximately 2.5.

The amplification and filtering stage can be constructed as a Sallen-Key filter stage with DC-nulling as described in section 4.6. In this way the TIA noise outside the frequency range of interest is attenuated, while all low-frequency beacon light intensity fluctuations and all background light is filtered out as well. This circuit is illustrated in Figure 41. As discussed in section 4.6 the AD8655 will be used in the Sallen-Key filter, while the AD8628 is used to construct the DC-nulling circuit. The DC-nulling circuit adjusts the voltage amplifier feedback voltage level in order to arrive at a DC-voltage level at the output of the filtering stage equal to the reference voltage of $2.5V$. Gain switching is implemented using a switch that selects one of two feedback resistors: a $100k\Omega$ resistor for a gain of 101, or a resistor of $1.5k\Omega$ for a gain of 2.5. As a switch that selects between the two resistors the SN74LVC1G3157 from Texas Instruments is selected, as this is a small and energy efficient analog switch. The 'Gain switch' input in Figure 41 is a digital input that selects the position of this analog switch. This device is specified to have an on-state resistance of 10Ω [58], which for the feedback resistance of $1.5k\Omega$ corresponds to an additional series resistance of 0.7%. However, to determine the gain error contribution from this analog switch, only the difference in feedback resistance between different channels is relevant. This difference is specified to be 0.2Ω maximum, which corresponds to an error of 0.013%, which is small enough to be neglected.

The Sallen-Key filter is designed to be a Bessel-type filter. This type of filter features a minimum amount of signal distortion, which gives a clean output signal without overshoot. In this way the amplitude of the amplified beacon signal can be determined accurately by the AM-demodulation stage, without any significant dependence on the received uplink signal pattern. A 3rd order Sallen-Key filter is selected, as this is the highest low-pass filter order that can be implemented using a single opamp. The optimal component values for $R1$, $R2$, $R3$, $C1$, $C2$ and $C3$ are first calculated using theory from [59], but just as with the TIA design, it is assumed that a SPICE simulation leads to a more accurate prediction of the actual circuit behaviour. For this reason, the component values given in Figure 41 are the component values that give the desired filter behaviour according to a SPICE simulation of this circuit. The frequency response of the circuit as illustrated in Figure 41 is determined using this SPICE simulation, the results for this simulation are given in Figure 42, both for the normal gain and the low gain setting. It should be noted that in the low-gain configuration the shape of the frequency response changes considerably, since with a different gain the low-pass filter no longer shows the desired 3rd order Bessel behaviour when the values for $R1$, $R2$, $R3$, $C1$, $C2$ and $C3$ are not changed as well. The DC-nulling circuit also gives a lower high-pass cut-off frequency in this situation. This will however not be an issue, since with a stronger input signal noise sources will have a much smaller impact. While the circuit noise at the output of the filter stage will be $7.5mV$ RMS according to the SPICE simulation, a major contributor to this noise is the TIA stage noise. If the gain of the filtering stage is decreased when a strong input signal is present, the circuit noise at the output of the filter stage is simulated to be $175\mu V$ which makes this contribution in the error of the angle measurement almost negligible.

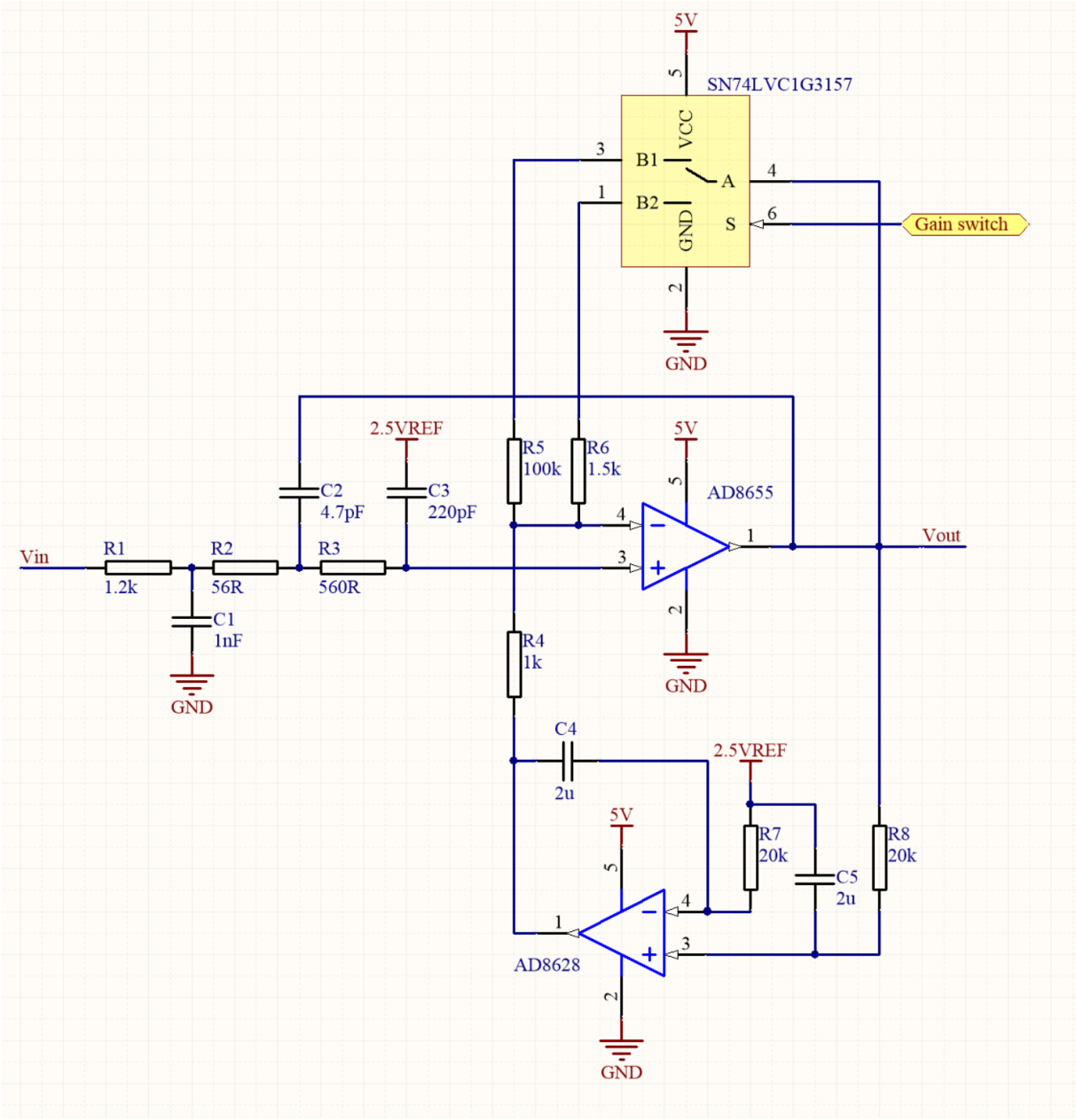

Figure 41: filter stage circuit design

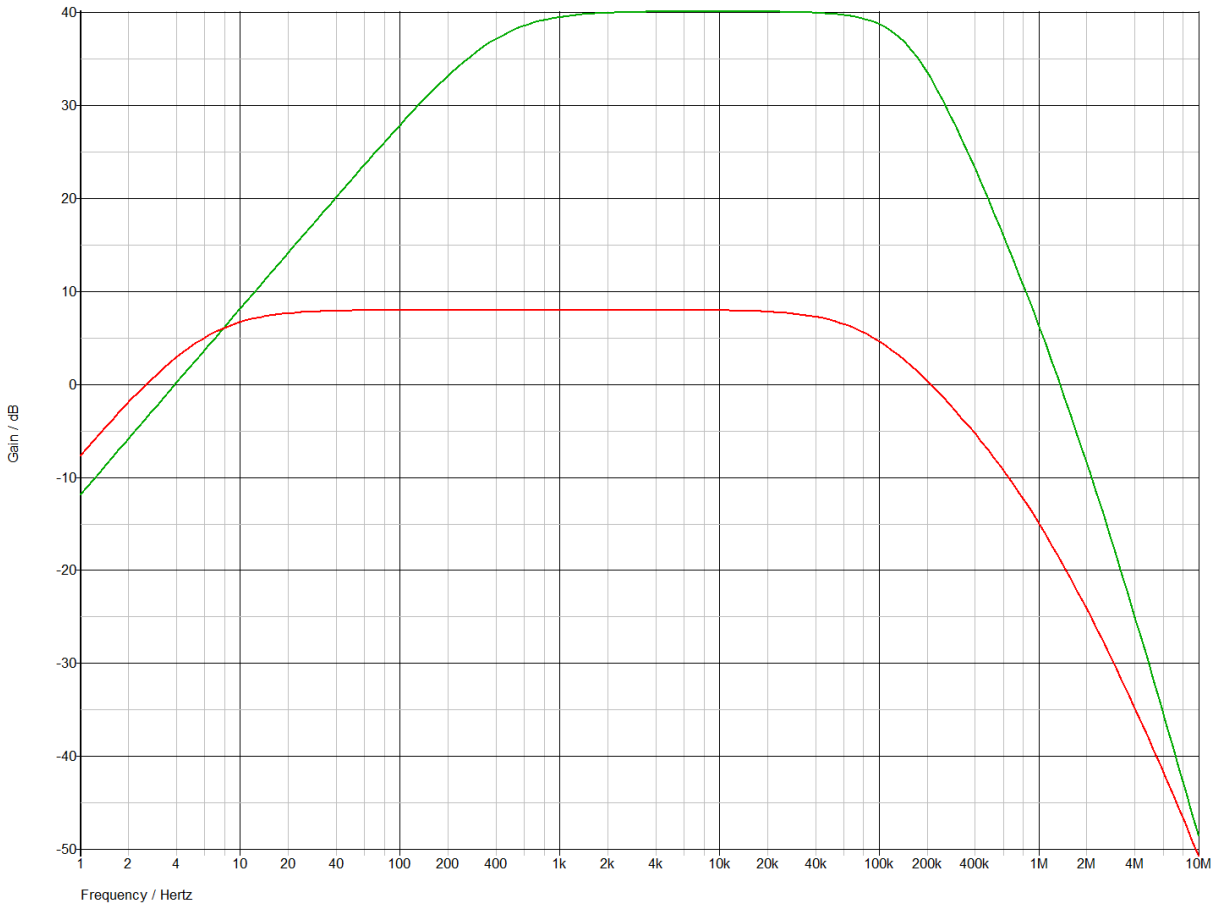

Figure 42: simulated filter stage frequency response for normal gain (green) and low gain (red)

5.1.4. AM-demodulation stage

In section 4.6 two different options are proposed for detecting the amplitude of the amplified beacon for each quadrant, using an opamp-based envelope detector or using an opamp-based rectifier. The opamp-based rectifier is selected since it has a much lower power consumption, but an advantage of the envelope detector is that it only looks at the maximum value of the input signal. Since the output signal from a low-pass filtered rectifier is the average of the absolute value of the input signal, this output signal is influenced by the signal shape of the input signal and thus by differences in the frequency response of each channel in the quad cell receiver circuit. An envelope detector follows the peaks in the input signal as illustrated in Figure 31 and is therefore expected to be more immune to differences between each channel. For this reason both circuits will be constructed and validated experimentally to determine the best solution for the quad cell receiver circuit.

The circuit for the envelope detector is given in Figure 43. The main opamp U1 is the AD8027, this is a fast opamp that is capable of quickly responding if the input voltage is higher than the current output voltage of the envelope detector, without overshooting. This opamp is also known to be radiation tolerant [60]. A disadvantage of this opamp is that it has a significant offset voltage of max $0.8mV$ [61]. To decrease the impact of this offset, a non-inverting amplifier is placed in the feedback line of U1, with opamp U2. This opamp is configured with a gain of 3, which will reduce the offset in the output amplitude voltage with a factor of 3, but will also speed up the response of opamp U1. Diode D2 is placed to limit the upwards voltage swing of U1 to the forward voltage V_f of diode D2, which also improves the speed of opamp U1, but resistor R2 is then necessary to limit the current draw at the output of U2. This will then introduce a new error source, since opamp U1 has a maximum input bias current of $6\mu A$, but

this error can be cancelled out by placing an equal resistor for the non-inverting input of U1, R1.

Capacitor C2 is charged by opamp U1 to store the detected peak voltage value, and the combination of C2 and R4 determines the speed with which capacitor C2 is discharged, and thus the bandwidth of the envelope detector. With the selected component values this bandwidth is set at $1kHz$.

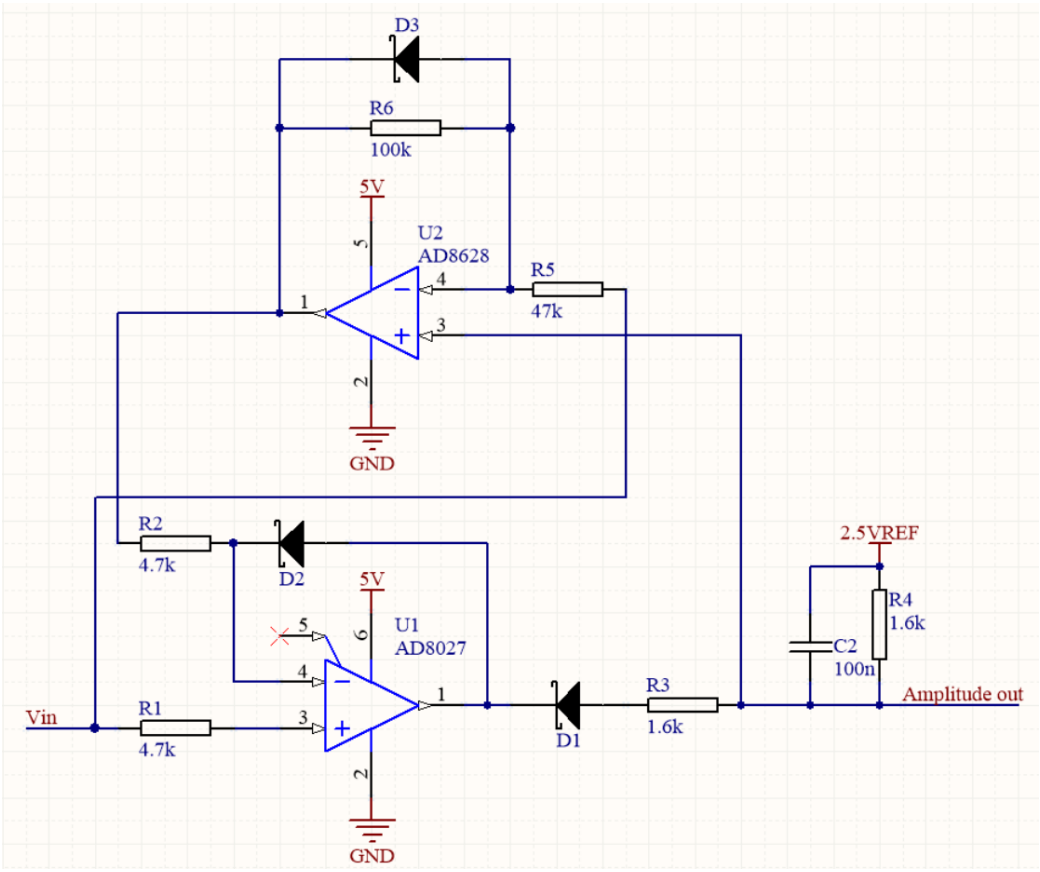

Figure 43: envelope detector circuit design

The circuit design of the opamp-based rectifier is given in Figure 44. The absolute value of the input signal, that is present at the output of U2, is passed through a low-pass filter in order to create an output voltage that follows the amplitude of the input voltage signal. The bandwidth of this filter determines the bandwidth of this AM-demodulator, which with the given values of R6 and C1 is set at $1kHz$.

The RMS noise voltage at the output of the filtering stage is simulated to be $7.5mV$, at a bandwidth of $100kHz$. Assuming that this noise voltage is evenly divided over the full bandwidth, this noise can be written as $24\mu V/\sqrt{Hz}$. At the AM-demodulation bandwidth of $1kHz$ for both circuits, this gives an estimated RMS noise voltage per angle measurement channel of $0.75mV$, which with a gain of $2 \cdot 10^8$ gives an input-referenced output noise per angle measurement channel of $3.75pA$. This is higher than the required $1pA$, but by employing digital filtering in the ATxmega64A4U microcontroller, this noise level can be reduced without using analog filters with impractically large capacitor and resistor values. If for example a digital low-pass filter is used with a bandwidth of 10Hz, an RMS noise voltage of $76\mu V$ per angle measurement channel can be expected, corresponding to $0.38pA$ at the input.

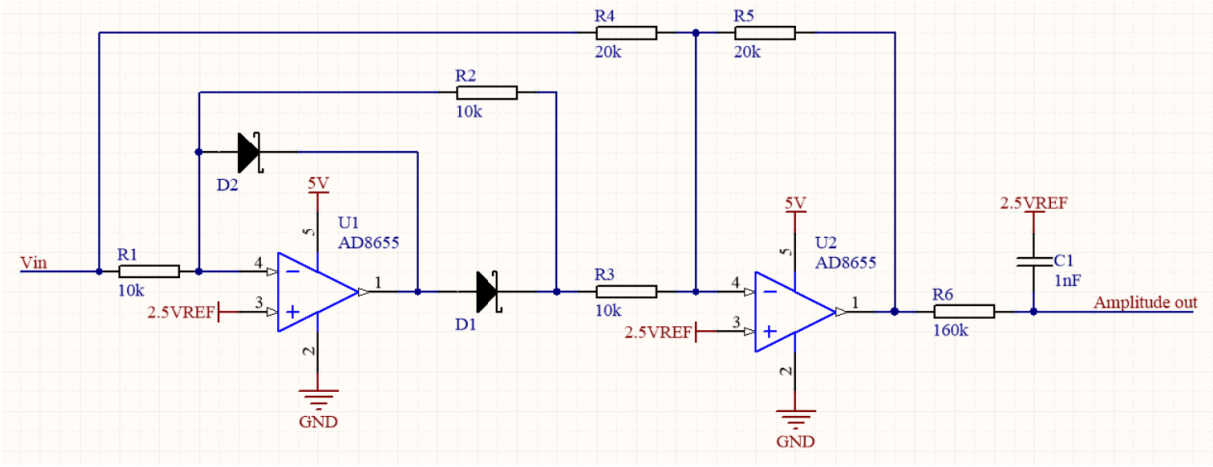

Figure 44: opamp-based rectifier circuit design

5.1.5. Angle measurement

In section 4.6 it is described that the analog to digital conversion of the four amplitude signals, and the consecutive angle of incidence computation, can be performed by an ATxmega64A4U processor. While the computational operations can be performed with high precision and thus a negligible computational error contribution, the analog to digital conversion will introduce errors. The error terms for the ADC in the ATxmega64A4U according to the datasheet of this device [56], along with their impacts on the quad cell receiver circuit design are:

- Non-linearity: the ADC of the ATxmega64A4U is specified to have a maximum non-linearity error of $\pm 2LSB$. If the $2.5V$ reference voltage is used as a reference voltage for the ADC as well, this will give an error of $\pm 0.6mV$ in 12-bit mode.
- Offset error: a small offset voltage is specified, along with an offset drift with temperature and supply voltage. However, it is also described that offset errors can be corrected internally by the ATxmega64A4U so this error source will be ignored.
- Gain error: the gain error is defined as a fixed voltage of $-1mV$ if an external reference voltage is used. While this voltage is specified to drift for different supply voltages and temperatures, this drift will thus be equal for all four channel and will therefore not cause a deviation in the measured current ratios which are used to compute the projected dot position. This error can therefore be ignored for the quad cell receiver electronics.
- Noise: the ADC is specified to have an input noise of $0.4mV$ RMS. With the noise floor at the output of the AM-demodulation stage of $0.75mV$ RMS, this noise contribution will be small in an RMS sum.

While most ADC error sources are negligible or can be corrected in this application, the non-linearity of the ADC will give a maximum deviation between any two cells of $1.2mV$. With the total amplifier gain of $2 \cdot 10^8$, this corresponds to a photocurrent of $6pA$. Since this value is already known and specified, it is not necessary to include this effect in the experimental validation. This value should be added to the measured offset error budget of the experimental setup in order to include this effect in the performance characterisation of the quad cell receiver circuit.

5.1.6. Data conversion

It is described in section 4.6 that a summing amplifier will be used to combine the signals at the output at the filtering stage for each quadrant to arrive at a single uplink data signal. In order to convert this signal to a digital signal that can be interpreted by the FPGA, a comparator can be used to perform a bit decision on the uplink data signal. The processor in the quad cell

receiver circuit, the ATxmega64A4U, contains a comparator module. By employing this module, no additional components are required which is beneficial in terms of power consumption. Another advantage is that some characteristics of the comparator can be adjusted by software, such as the hysteresis level.

An advantage of using hysteresis in the comparator that makes a bit decision is that noise on the signal from the summing amplifier will not be able to influence the detected digital at the output of the comparator. The minimum convertible light power is computed to be $1.3nW$ in section 3.7.5, which with a quad cell sensor responsivity of $0.95A/W$ and a total gain of $2 \cdot 10^8$ corresponds to a minimum output signal at the summing amplifier of $247mV$. The required input-referred noise at the output of the filter stage of $95pA$ multiplied by the gain of $2 \cdot 10^8$ should be less than $19mV$ per channel, since this noise is added for all four channels in the summing amplifier in a square root sum this noise will be $38mV$ at maximum. Since the maximum selectable hysteresis in the comparator of the ATxmega64A4U is $35mV$ in high-speed mode [56], the amplitude of the signal to the comparator module should be reduced to make sure that the noise level on the uplink data signal is well below the hysteresis level, to prevent noise from generating false bit detections. If a gain of 0.1 is selected for the summing amplifier, the noise voltage will be reduced to a level that is well below the medium hysteresis level of the ATxmega64A4U of $20mV$. This will make the probability of a bit detection error negligible.

The circuit design for the summing amplifier is given in Figure 45. As described in section 4.6 the AD8628 is used in this summing amplifier. The supply voltage of this opamp is however set at $3.3V$ instead of the $5V$ of the rest of the analog circuitry, since the output of the summing amplifier will be connected to the ATxmega64A4U which runs at $3.3V$. In order to limit the voltage at the inverting node of this opamp to slightly above $3.3V$ a diode is placed there.

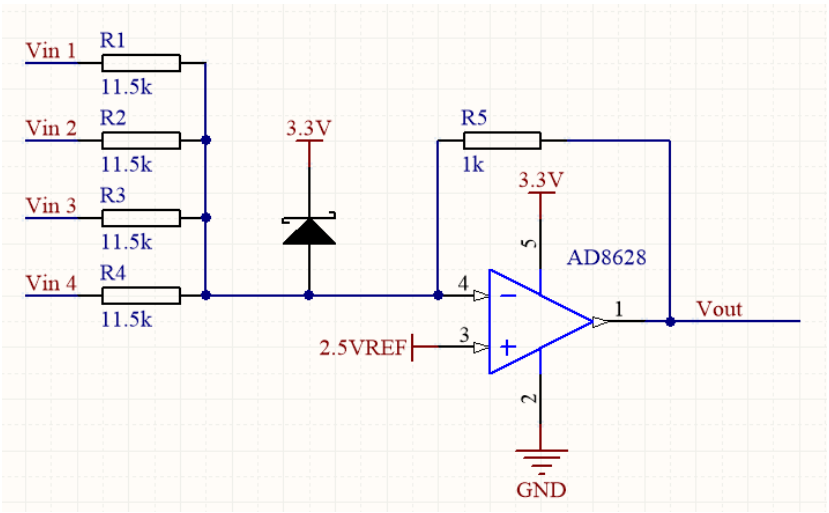

Figure 45: summing amplifier circuit design

5.1.7. Physical construction

The physical construction of the prototype quad cell receiver circuit is illustrated in Figure 46. This prototype is constructed using a four-layer PCB. On the left an EMI cover can be seen, which is used to shield the TIA stage from external interference.

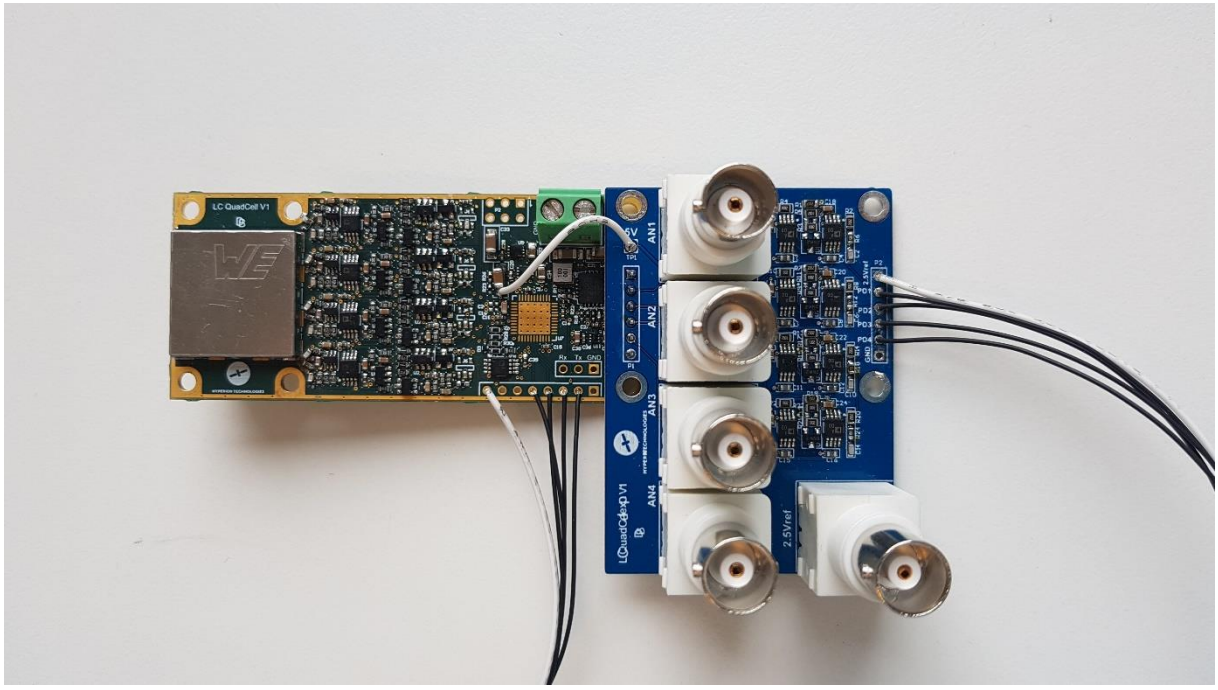

Figure 46: Prototype quad cell receiver circuit

5.2. Experimental setup description

In order to determine whether the requirements on the quad cell receiver circuit as mentioned in section 5.1 have been met, two different types of measurements have to be performed. In order to measure noise on the output of the filter stage and at the output of the AM-demodulation stages a Rigol DS1054z oscilloscope is used. A fourier transform is performed on the data acquired by this oscilloscope in order to determine the noise spectrum. An RMS sum is also computed for the acquired data in order to determine the RMS integrated noise voltage. The noise floor of this setup is illustrated in Figure 47 for a frequency range of $1MHz$ and in Figure 48 for a frequency range of $100kHz$. During the noise measurements no optical signal must be supplied to the input photodiodes, so these are blinded during the noise measurements.

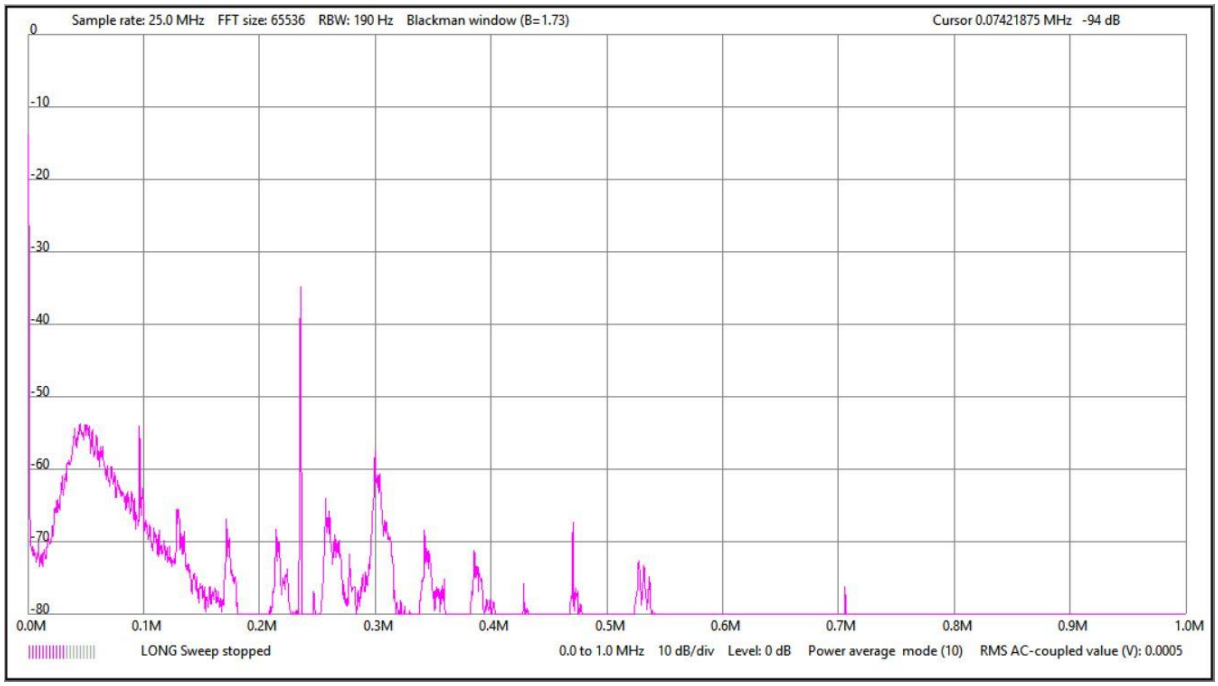

Figure 47: noise measurement setup noise floor, 1MHz

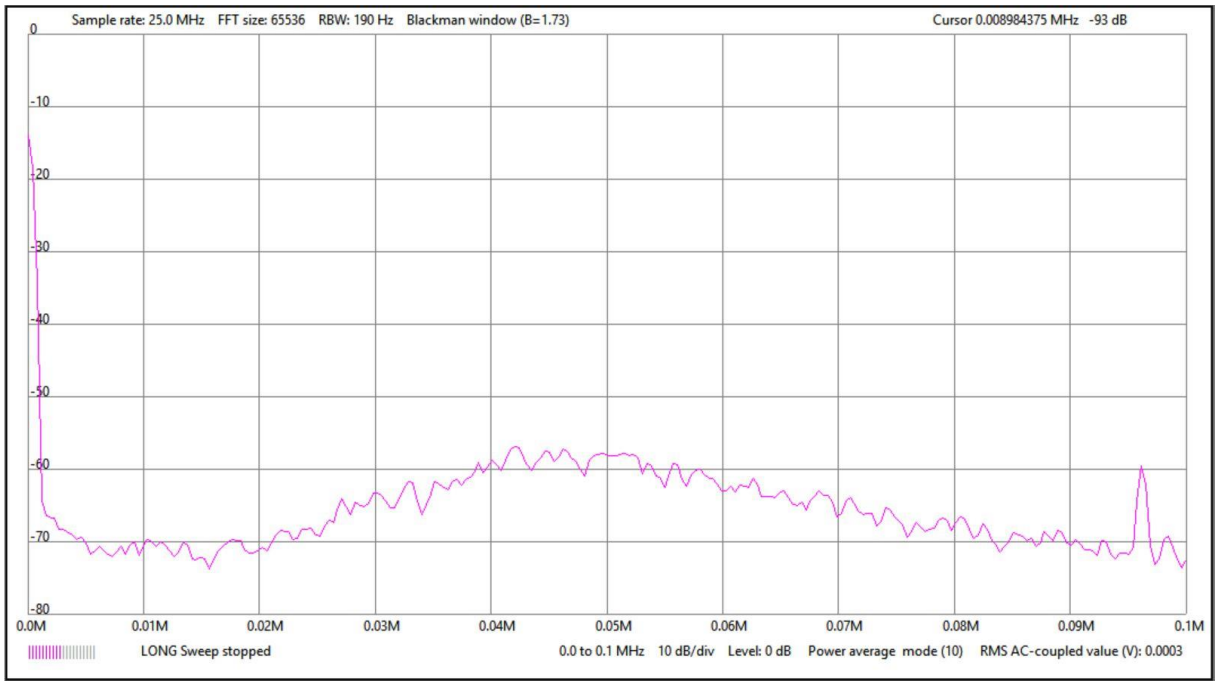

Figure 48: noise measurement setup noise floor, 100kHz

In order to accurately determine the gain- and offset errors between the channels at the output of the AM-demodulation stage a different method can be used, since the output from this stage is a DC-value for a constant input signal. For this an Keysight 34461A 6.5 digit digital multimeter will be used. This device is specified to have an accuracy 0.002% of the current reading, plus 0.0006% of its full range for a range of $1V$ [62]. For the minimum input signal of $1.3nW$ as determined in section 3.7.5, this will give a signal amplitude of $62mV$ at the output of one of the filter stages with the sensor responsivity of $0.95A/W$ and a gain of $2 \cdot 10^8$. This will give an error of $7.2\mu V$ in the digital multimeter, or $36fA$ if this value is expressed as an input-referred value, well below the gain error and offset error requirements on the quad cell receiver circuit.

Since the Rigol oscilloscope is a relatively inaccurate device, the Keysight DMM is also used to measure integrated RMS noise values. The Keysight can measure RMS AC voltages at frequencies between 3 and 300kHz, with a specified accuracy of 1% of the current reading, plus 0.02% of the full scale range. With the predicted noise level at the output of the AM-demodulation stages of $0.75mV$, this will give a total measurement error of $27.5\mu V$ with the minimum full-scale range of $100mV$, small enough to be ignored.

The input signal in the experimental setup is generated by an LED with a wavelength of $800nm$. At this wavelength the responsivity of the photodiodes used in the quad cell sensor is much lower than the value of $0.95\ A/W$ at $1550nm$, which simplifies the setup and does not require additional attenuation to arrive at the required photocurrents. This LED and the quad cell receiver prototype are mounted rigidly, as illustrated in Figure 49. The electrical input signal to the LED is generated by a Peaktech 4060MV signal generator, in order to generate different optical signals.

The distance and orientation of the quad cell receiver and the LED are adjusted to obtain an approximately equal output signal amplitude per quadrant. Since no means was available to measure the output power from the LED, the gain of the TIA and voltage amplifier stage is assumed to be equal to $2 \cdot 10^8$. In this way the input photocurrent magnitude can still be determined from the amplified output signal. Even though in this way differences in gain between each channel are ignored, these fixed gain differences can be determined during alignment of the actual satellite terminal in production as well and are therefore not relevant in the performance characterisation of the quad cell receiver circuit. Deviations in gain with different input signals can however be evaluated in this way.

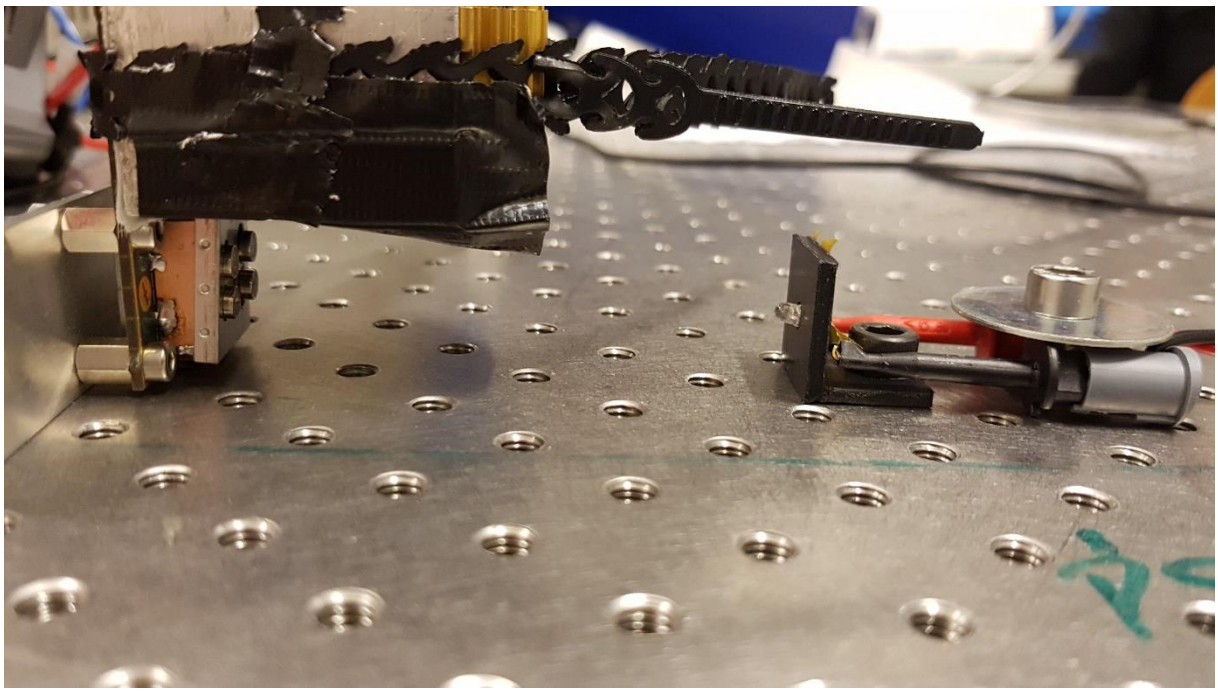

Figure 49: Rigid mounting of the signal generator LED and the quad cell receiver electronics prototype

In order to evaluate the effect of temperature on the quad cell receiver circuit, a resistive heater is mounted on the backside of the prototype, as illustrated in Figure 50. This heater consists of two resistors mounted on a block of aluminium, which acts as heat spreader. Using this heater the temperature of the prototype electronics can be increased evenly by running a current through the resistors.

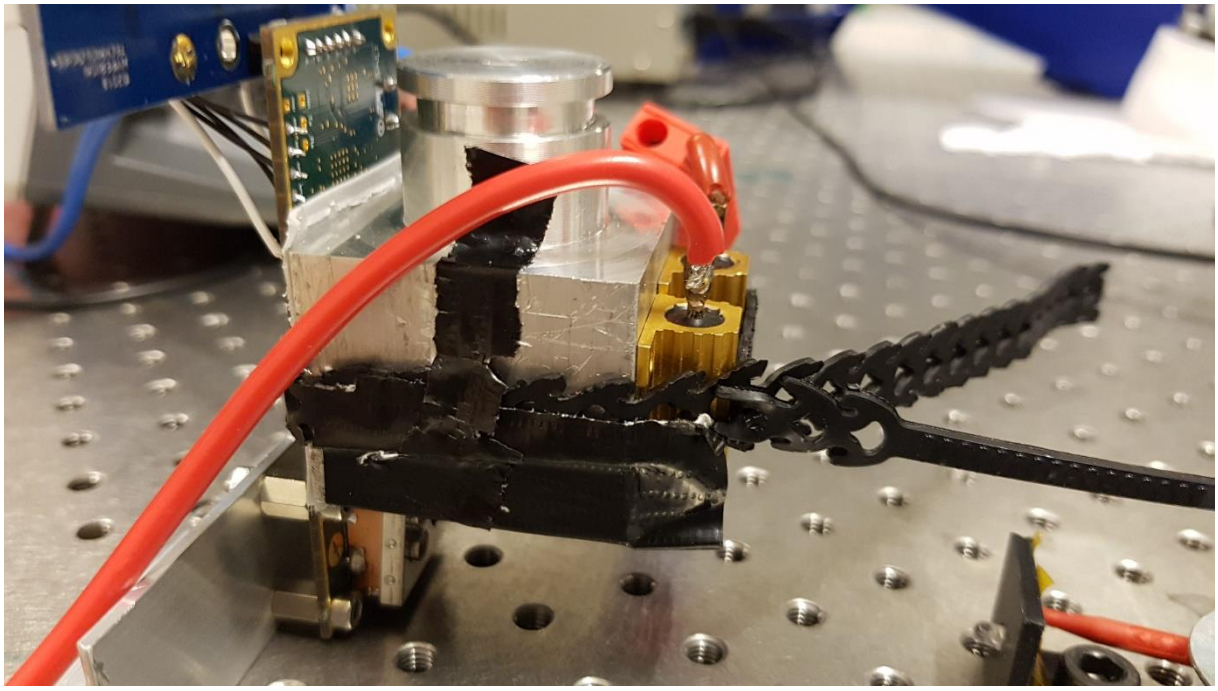

Figure 50: Quad cell receiver prototype resistive heater

5.3. Experimental results

Using the experimental setup described in section 5.2 several experiments are performed in order to characterise the quad cell receiver circuit prototype. The results from these experiments are presented and analysed per circuit section.

5.3.1. Transimpedance amplifier stage experimental characterisation

Since the output signal from the TIA stage is so weak, the information that can be obtained about the behaviour of the TIA stage using the experimental setup is limited. The output noise spectrum from the TIA stage is given in Figure 51. For a situation where no light signal is received by the photodiodes. When comparing this graph with Figure 47, it can be seen that the measured noise signal is barely higher than the noise floor of the Rigol oscilloscope. The noise behaviour below $100kHz$ and the peaks between $100kHz$ and $300kHz$ are caused by the noise floor of the Rigol oscilloscope. The noise level can be seen to decrease with approximately $20dB$ in one decade, between $100kHz$ and $1MHz$, as is expected from a regular TIA. Using the Keysight DMM an accurate integrated RMS noise measurement is performed, the noise at the output of the TIA stage is determined to be $0.20mV\ RMS$. This is significantly higher than the simulated noise level of $0.12mV\ RMS$ as described in section 5.1.2. Possible contributors to this increased noise level are inaccuracies in or incompleteness of the AD8655 SPICE model, and incompleteness of the simulated circuit. Effects that are not simulated are noise on the supply voltage line and parasitic capacitances in the prototype circuit construction. Since the AD8655 as used in the TIA is used close to its bandwidth limit, nonlinear effects that are not included in its SPICE model can start to play a role.

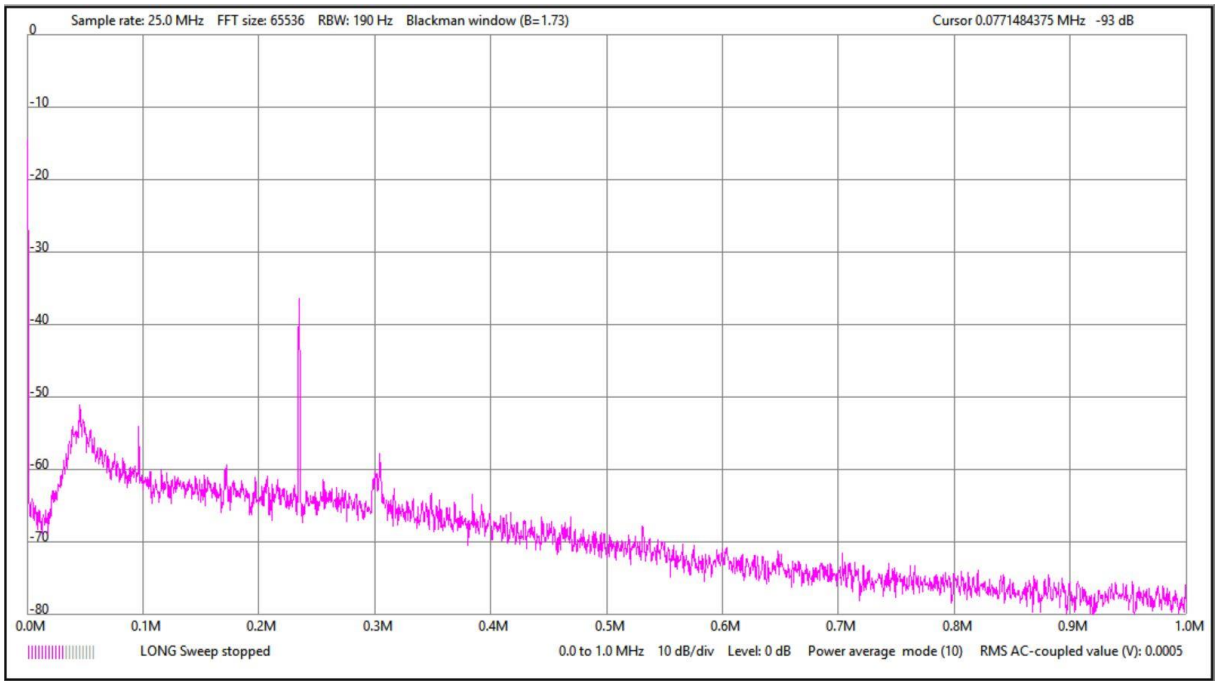

Figure 51: TIA stage output noise spectrum

5.3.2. Filter stage experimental characterisation

The frequency response of the combination of photodiode, TIA stage and filter stage is measured by applying a sinusoidal electrical signal on the optical signal generation LED of equal amplitude for different frequencies. The output signal of each quadrant is acquired using the Rigol oscilloscope and the RMS magnitude of the filter output signal of each quadrant is recorded. Since the incident power on each quadrant is slightly different, the recorded RMS output signal voltages will be normalised to remove these differences by assuming that the gain of each channel is equal in the passband, as described in section 5.2. In Figure 42 it can be seen that around an input signal frequency of $10kHz$ the flattest and maximum frequency response is expected. For this reason the recorded RMS output signal voltages are normalised using the recorded RMS output signal voltage at a sinusoidal input signal of $10kHz$, using:

$$U_{norm} = \frac{U_{rec}}{U_{ref}} \tag{43}$$

Where U_{rec} is the recorded RMS output signal voltage, U_{ref} is the reference RMS output voltage at $10kHz$ and U_{norm} is the normalised RMS output signal. The measured reference voltages are given in Table 13. The resulting frequency responses of the four quadrants are given in Figure 52.

Table 13: Filter stage normalisation reference voltages

	Quadrant 1	**Quadrant 2**	**Quadrant 3**	**Quadrant 4**
RMS reference voltage U_{ref}	$1110mV$	$1040mV$	$988mV$	1035mV

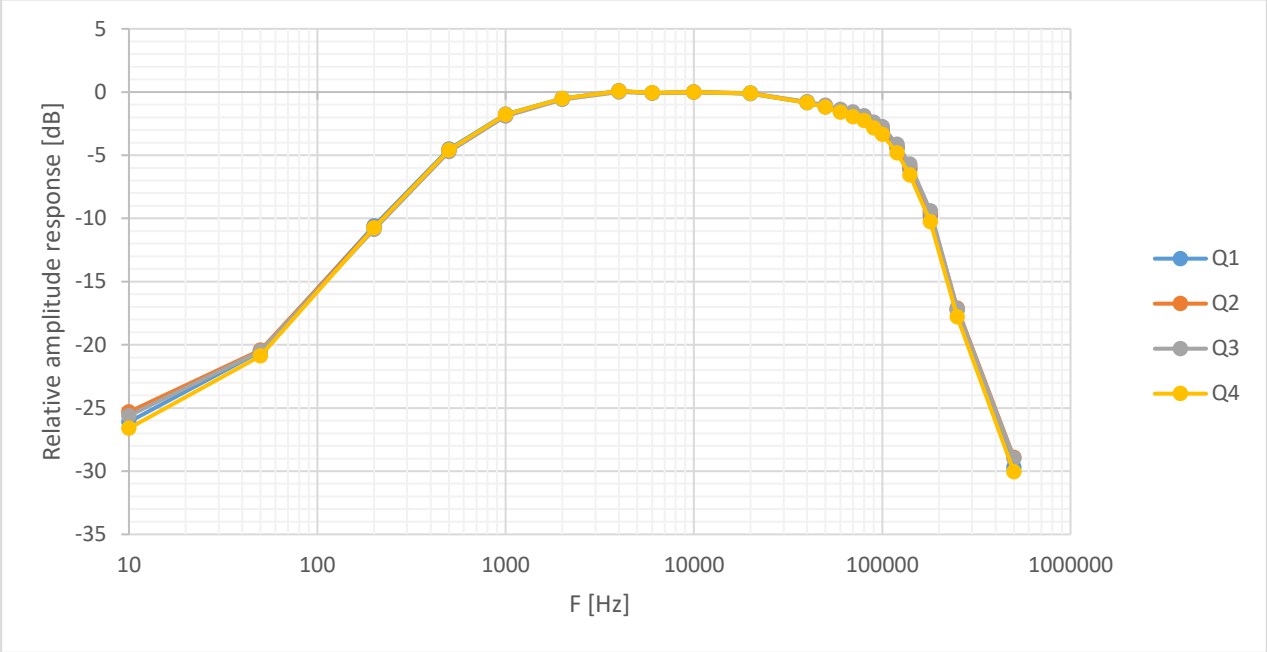

Figure 52: Filter stage output frequency response

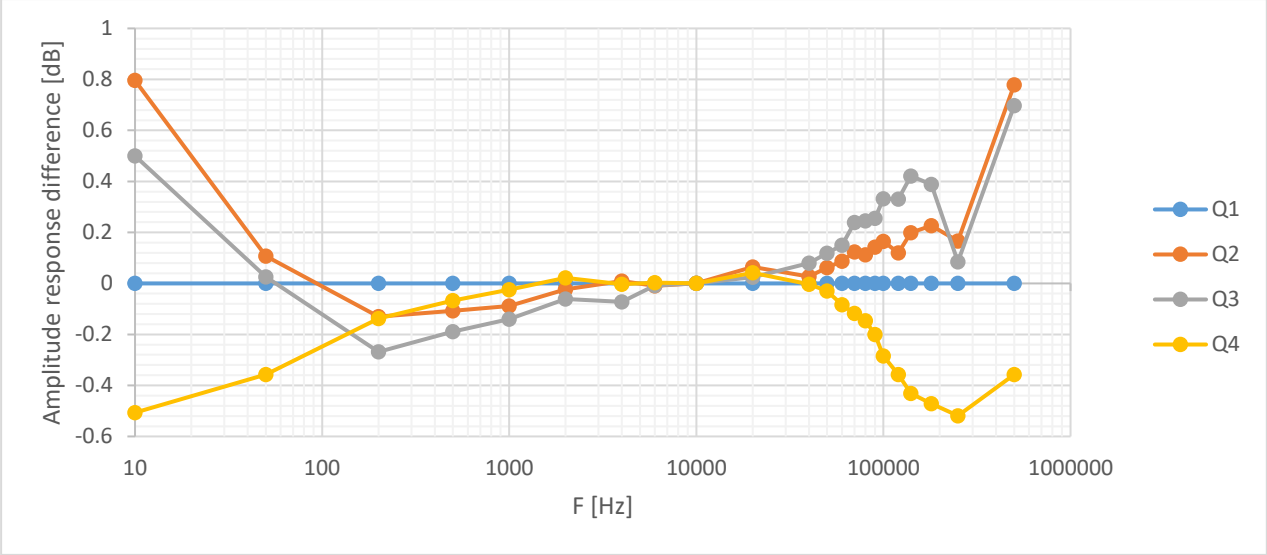

Figure 53: Filter stage output frequency response, deviations between quadrants

Due to the normalisation step, the output signal amplitude at $10kHz$ is defined as $0dB$. When comparing Figure 52 with Figure 42, the measured frequency response matches the simulated response well. A notable difference is the reduced curve slope at low frequencies. It should be noted that at these signal levels the noise floor of the filter stage output signal becomes significant in the RMS output signal amplitude sum, which increases the measured output signal level. Another clear difference is the slight decrease in output signal amplitude at high frequencies below the corner frequency of the filter stage. While parasitic capacitances in the prototype construction can lead to non-ideal filter behaviour, as the capacitor values used in the filter stage are small, imperfections in the optical signal generation LED can also be a factor. To investigate this source, the same experiment was performed using a $1550nm$ laser diode as optical signal source. This response is given in Figure 54. In this graph a much more reasonable frequency response can be seen around $100kHz$, supporting the theory that the LED has a non-flat frequency response. The laser diode was not used for further experiments however, since it was expected that the speckle pattern from this laser diode, coupled with

minimal mechanical drift in the experimental setup, would lead to unacceptable deviations in the incident optical power per quadrant.

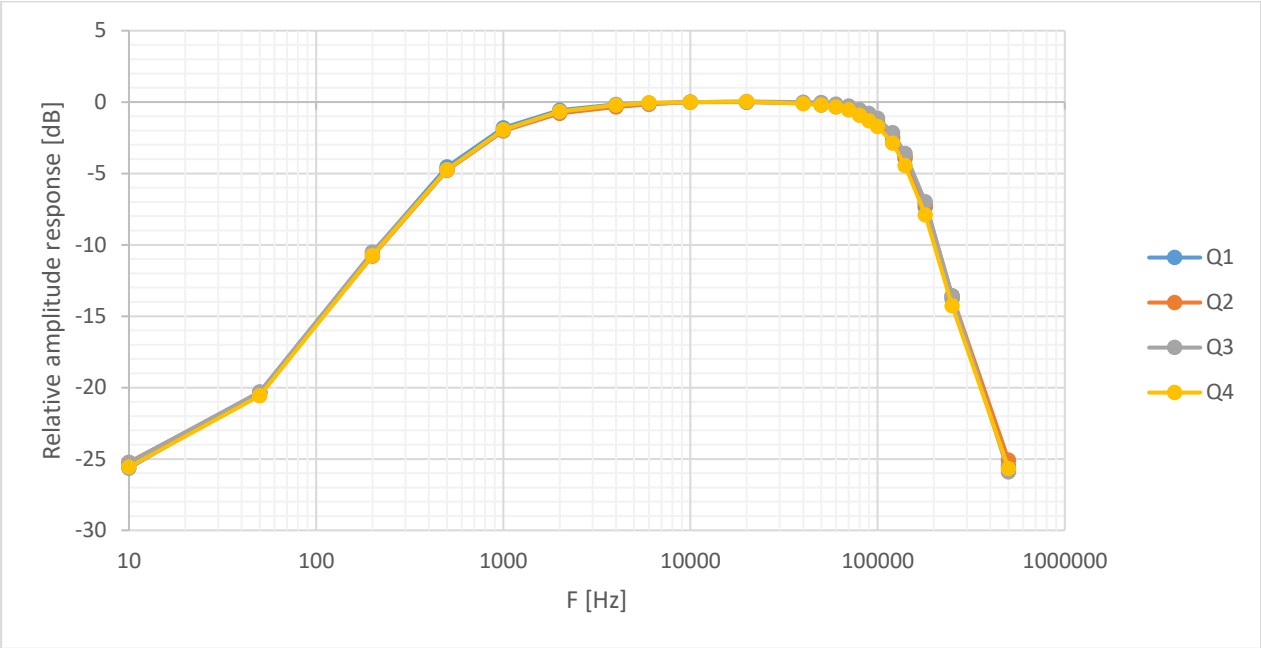

Figure 54: Filter stage output frequency response, Laser diode source

In Figure 53 the deviations between the frequency response of the separate quadrants is illustrated, where quadrant 1 is used as the reference value. It can be seen that within the passband the deviations between the separate quadrants are minute. Around and beyond the corner frequencies of the filter stage these deviations steadily grow, but since the amplifier response at these frequencies is already decreasing, the actual impact of these differences on the output signals will be negligible.

To evaluate the impact of temperature on the frequency response at the output of the filter stage, this experiment is repeated at a temperature of 56°C. In Figure 55 and Figure 56 the temperature variation is illustrated. It can be seen that a slight difference in temperature is present in the PCB, which makes the measurements at elevated temperature an evaluation of the effects of temperature differences between the quadrants as well.

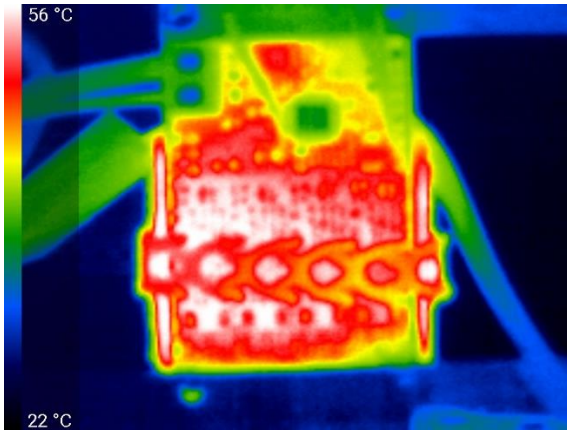

Figure 56: elevated temperature experiment temperature variation

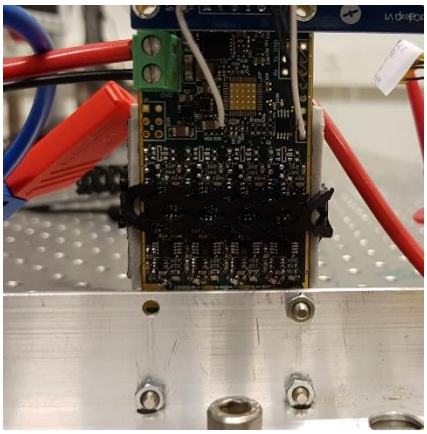

Figure 55: thermal camera reference image

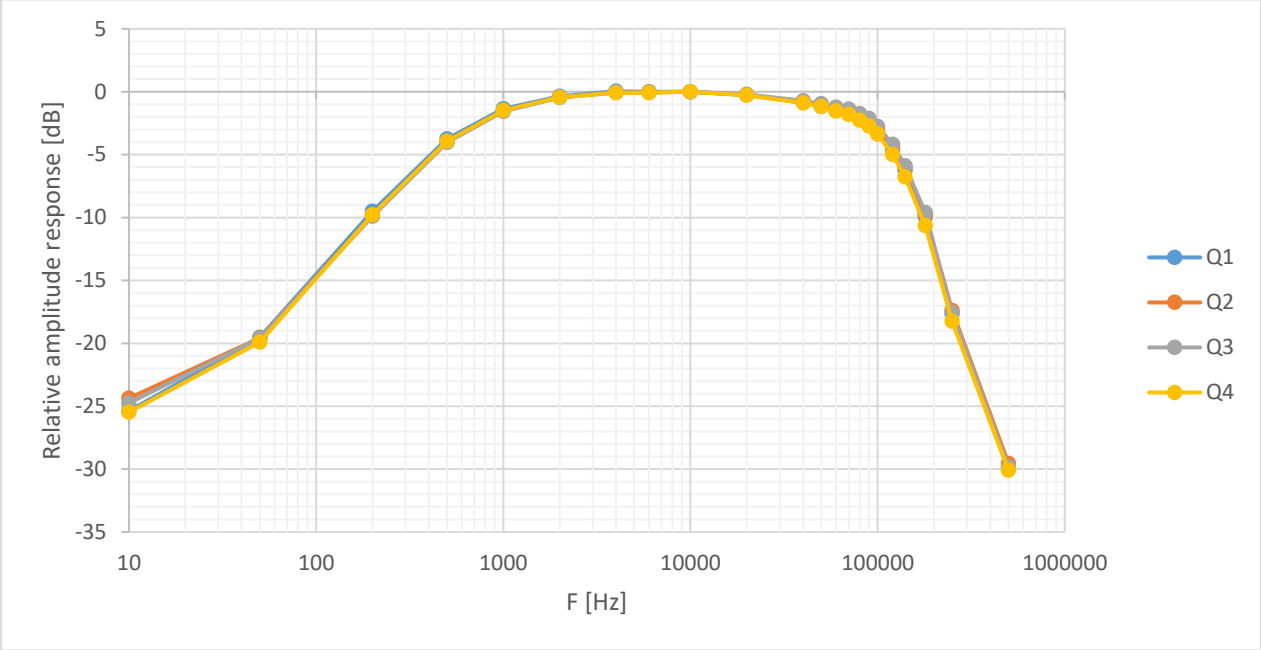

Figure 57: Filter stage output frequency response, elevated temperature

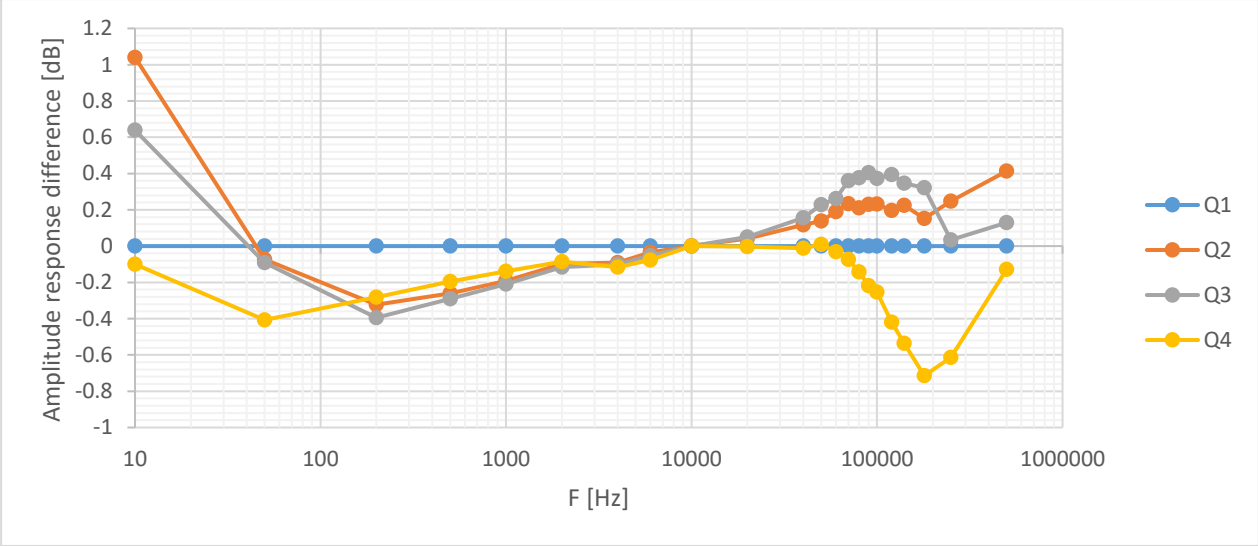

Figure 58: Filter stage output frequency response, elevated temperature, deviations between quadrants

In Figure 57 the measured filter stage output frequency response at higher temperatures is illustrated, along with the differences between the quadrants in Figure 58. It can be seen that these results are highly similar to the results obtained at ambient temperature in Figure 52 and Figure 53. The deviations between the cells within the passband are slightly larger than at ambient temperature, but still not significantly so. These larger deviations can be explained by the difference in temperature over the PCB as illustrated in Figure 56.

In Figure 59 and Figure 60 the differences between the frequency response graph of Figure 52 and the frequency response at elevated temperature of Figure 57 are illustrated, in dB and in %. It can be seen that, especially outside of the passband but also within, the frequency response differences are significant. It is however interesting to note that these deviations are approximately equal for all four quadrants: while the amplifier gain is larger at low frequencies at higher temperatures, this effect is almost the same for all four quadrants. Since the angle measurement is performed by using the differences in photocurrent between the four

quadrants, the impact of elevated temperature on the filter stage frequency response will not be relevant.

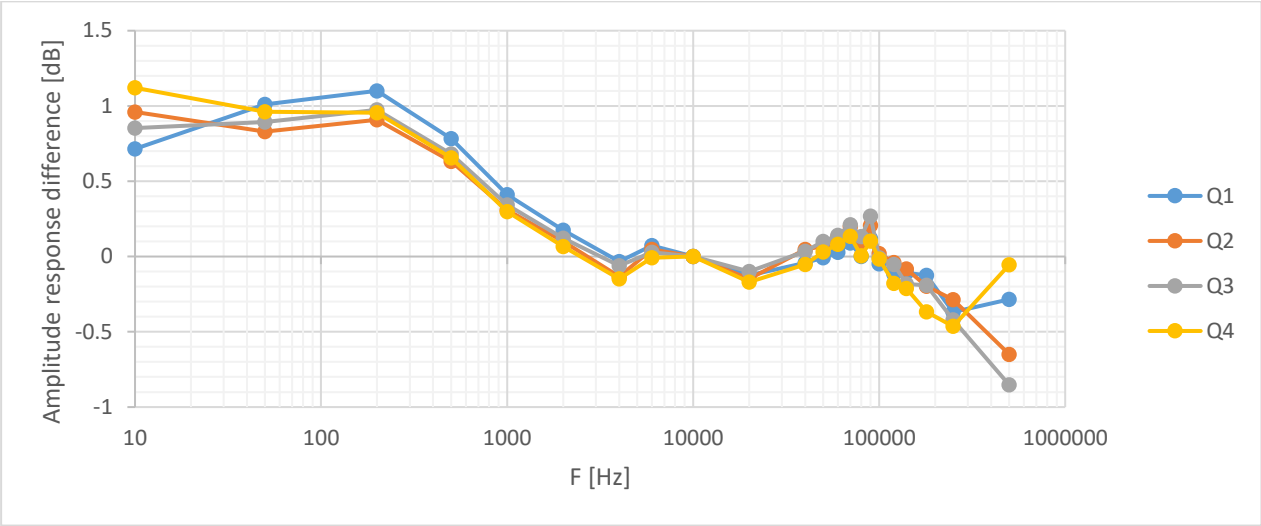

Figure 59: Filter stage output frequency response difference between ambient and elevated temperature, dB

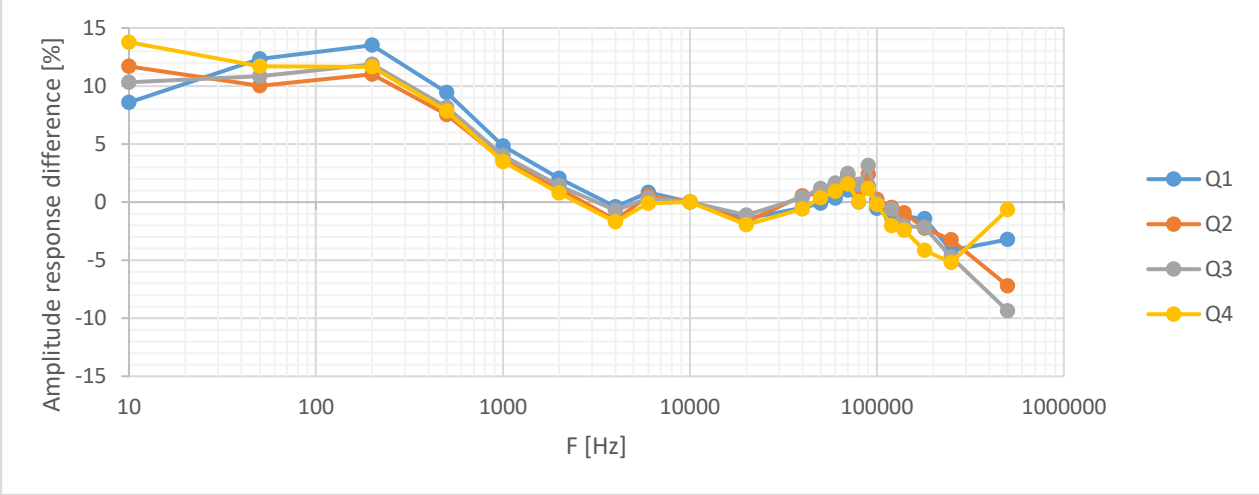

Figure 60: Filter stage output frequency response difference between ambient and elevated temperature, %

The noise spectrum at the output of the filter stage is illustrated in Figure 61, with the noise spectrum at a temperature of 56°C given in Figure 62. It can be observed that the differences between these two spectra are minimal. Next to this, the noise spectrum follows the characteristic TIA noise profile as described in [49]. Above $400kHz$ a large number of noise peaks can be observed. The cause for these peaks is unknown, it could be related to noise from the power supply of the prototype circuit that enters the signal path. The magnitude of these noise peaks is however significantly lower than the characteristic TIA noise, so this effect can be ignored. The integrated noise at the output of the filter stage was simulated to be $7.5mV\ RMS$, as described in section 5.1.3. The actual integrated noise is determined to be $17.9mV$ using the Keysight DMM. This discrepancy can be largely attributed to the noise from the TIA stage, which was almost twice as large as predicted. Next to this the sharpness of the filter response at the corner frequencies as illustrated in Figure 52 appears to be weaker than the simulated filter response from Figure 42. This can cause the filter stage to be less effective at removing noise from the TIA stage output signal than expected. Nevertheless, if the output signal from the TIA stage was only amplified with a gain of 100 and not filtered the noise level at the output of the filter stage would have been $20mV\ RMS$, so the filter stage does have a positive effect on the quad cell receiver circuit performance.

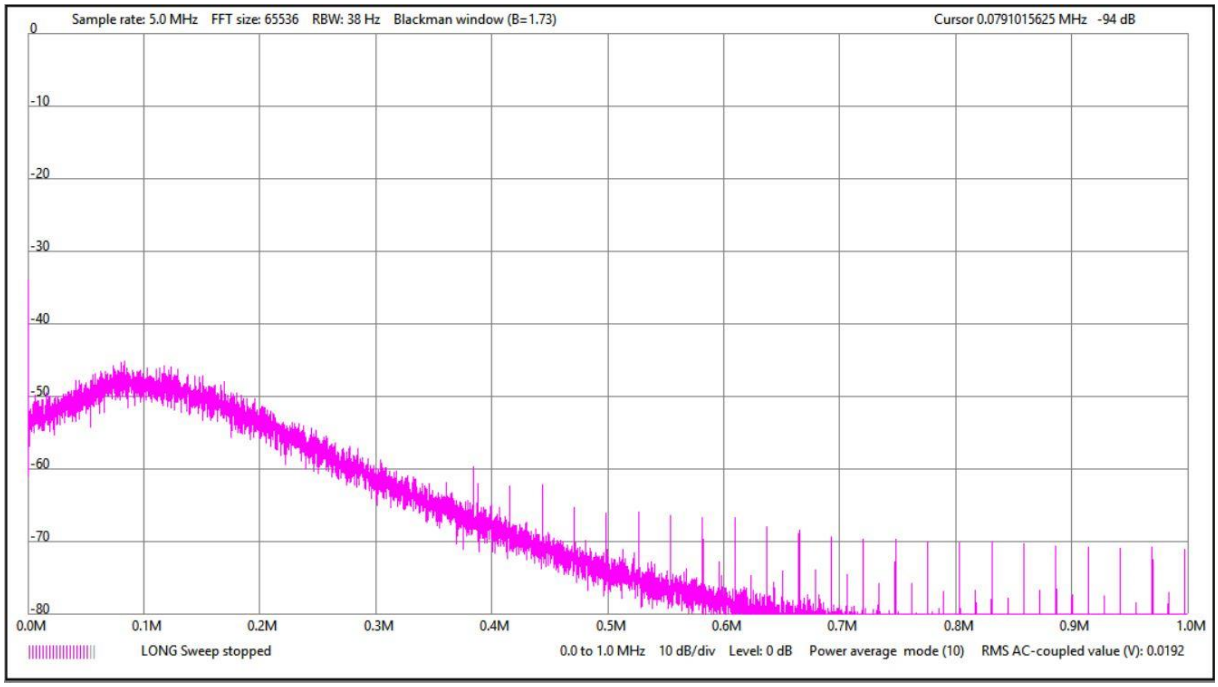

Figure 61: Noise spectrum at filter output, ambient temperature

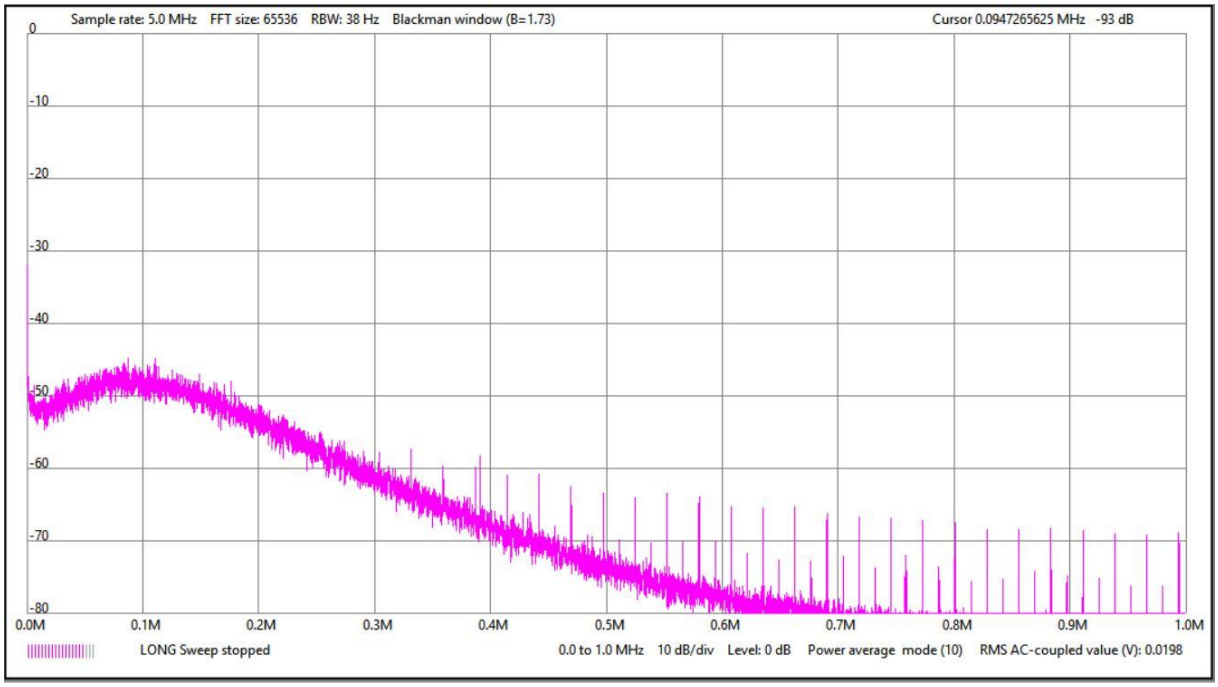

Figure 62: Noise spectrum at filter output, elevated temperature

5.3.3. Summing amplifier characterisation

The noise at the output of the summing amplifier is determined to be $4.9mV\ RMS$ using the Keysight DMM. The noise at the output of the filter stage of $17.9mV$ multiplied by the summing amplifier gain of 0.1, and added four times in an RMS sum would give an expected summing amplifier output noise of $3.58mV\ RMS$. The fact that the measured noise is higher implies that the output noise from the four filter stages is not completely uncorrelated. This further indicates that unmodelled effects, such as the effect of supply voltage noise or reference voltage noise, are contributing to the total noise of the quad cell receiver circuit as these noise sources would add an equal and thus correlated noise to each quadrant.

5.3.4. AM-demodulation circuit characterisation

In the prototype quad cell receiver circuit two AM-demodulation circuits are included: an envelope detector and a rectifier circuit. Both circuits are characterised in order to determine the best option for this application. This characterisation will be done by applying a square wave input signal to the optical signal generation LED, in order to simulate an OOK signal. The frequency of this signal will be fixed at $20kHz$, but the magnitude of this modulation signal will be varied in order to determine the variation between the four quadrants at different input signal levels. Just as with the characterisation of the frequency response at the output of the filter stage, the incident power on each quadrant will be slightly different and the precise magnitude of this incident power is unknown. For this reason the same assumption is made that the gain of the amplification stages is constant at $2 \cdot 10^8$, which allows the use of a reference output signal value to be used to normalise the measured output voltages from the AM-demodulation circuits.

The output voltages from the AM-demodulation circuits are measured using the Keysight DMM in DC mode, which has a low-pass cutoff frequency of $5Hz$. These recorded values are normalised using the RMS output voltages at the output of the filter stages at an input signal of $20kHz$ with a significant magnitude as measured by the Rigol oscilloscope. In Figure 63 the measured normalisation values for the envelope detector circuit measurements are illustrated, with one set of reference signals recorded at the start of the envelope detector measurement series and one set recorded at the end of the measurement series. Unfortunately, the received optical power per quadrant was not constant over the course of these measurements with especially the total received optical power changing significantly, but also the ratio of received optical power per quadrant. Since for the computation of the received light angle of incidence only the ratios of received optical power per quadrant are relevant, these reference signal amplitudes are normalised using the values for quadrant 1 to arrive at scaling factors, as illustrated in the right image of Figure 63. It can be seen that deviations in received optical power per quadrant up to a percent occurred over the course of these measurement series. This is a significant error source, as the required maximum gain error between two quadrants 1%.

To minimise the effects of this input signal drift, instead of using a single set of normalisation values on the recorded AM-demodulation circuit output voltages, an interpolation is made between the scaling factors as illustrated in the right image of Figure 63. By dividing the AM-demodulation circuit output voltage datasets evenly over these interpolated lines between the start and the end of the measurement series, each output voltage dataset will be corrected using its own set of scaling factors. Using the assumption that the drift in input signal magnitude occurred at a steady rate, the effects of this drift are removed most effectively in this way.

Since the received power per quadrant is not directly measured, the received power per quadrant is approximated from the output signal from the AM-demodulation circuit. Using the gain of $2 \cdot 10^8$ that is assumed to be fixed, the power per quadrant is calculated from the recorded AM-demodulation output voltage from quadrant 1 using:

$$P_{in} = \frac{V_{Q1}}{2 \cdot 10^8} \tag{44}$$

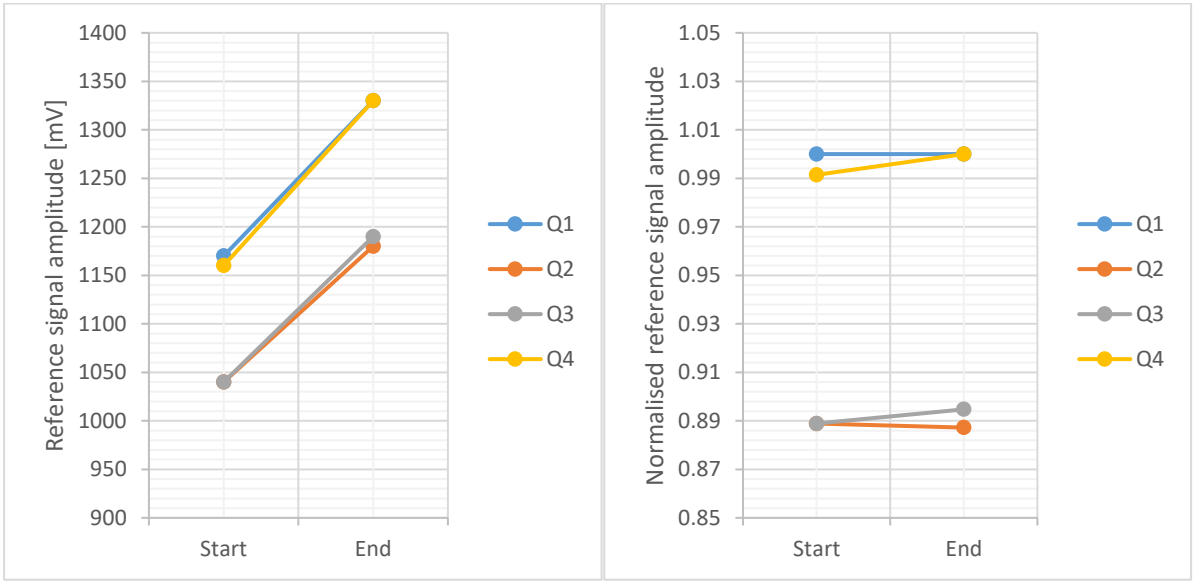

Figure 63: Normalisation values used for the envelope detector measurements, ambient temperature. Absolute values (left) and normalised scaling factors (right)

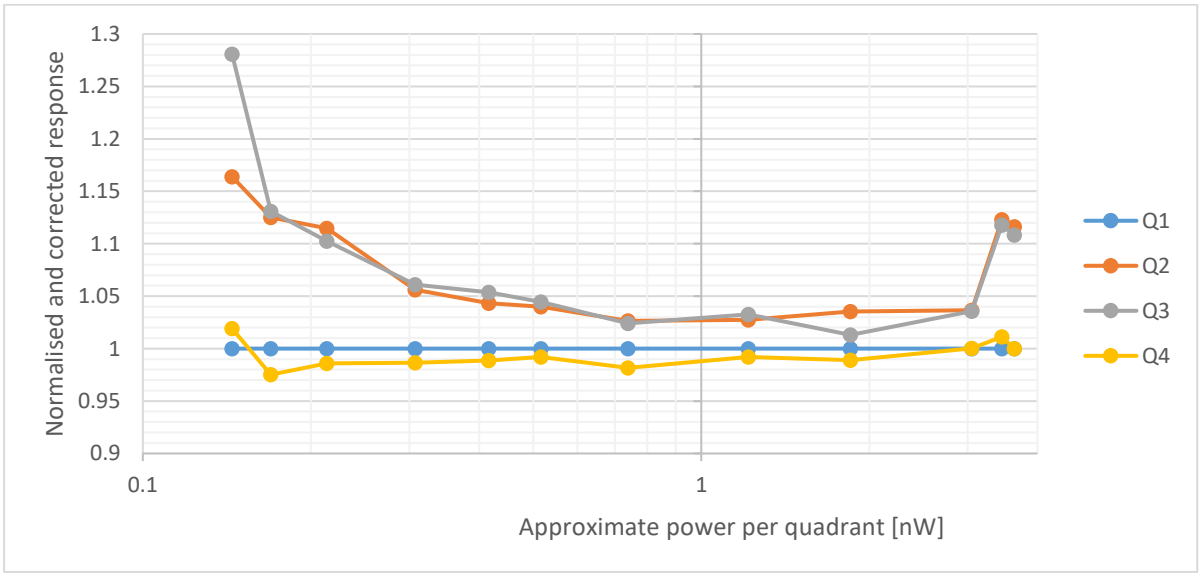

Figure 64: Normalised and corrected envelope detector output voltages, ambient temperature

In Figure 64 the recorded output voltages from the envelope detector at ambient temperature are given. These values have been normalised using the recorded output voltages from quadrant 1 and corrected using the curves from Figure 63. It can be seen that significant deviations between the four quadrants remain. At low input power levels quadrants 2 and 3 deviate significantly from quadrants 1 and 4. An unexpected observation is that the output voltage from the envelope detector seems to saturate at an output voltage (uncorrected) of $700mV$, thereby limiting the maximum optical power per quadrant to $3.5nW$. This causes the significant deviation between the quadrants around this optical power level.

Within the region of interest, with optical powers per quadrant between $0.3nW$ and $3nW$ the deviations between the quadrants are still significant. Even though the average deviation of each quadrant could be calibrated relatively simply for each manufactured lasercom terminal as part of the manufacturing process using a fixed offset and multiplication factor, the deviation of one quadrant over this range of input powers is also considerable. In Figure 64 the largest deviation over this range of input power is observed for quadrant 3, with a total deviation of

4.7%. While the actual deviation will be slightly lower due to drift on the input power per quadrant as illustrated in Figure 63, this error cannot be caused entirely by this drift.

This experiment is repeated at an elevated PCB temperature of 56°C. The normalisation values and scaling factors for this experiment can be seen in Figure 65, the drift in the input signals for this set of measurements was much more significant than in Figure 63. Deviations of up to 2% can be seen. Using the same correction procedure the graph in Figure 66 is created. This graph is similar to the results in Figure 64, with the exception of the response from quadrant 2. Since this quadrant does not seem te behave significantly different from the other quadrants in Figure 65, the only remaining explanation is that the envelope detector circuit might be sensitive to temperature differences.

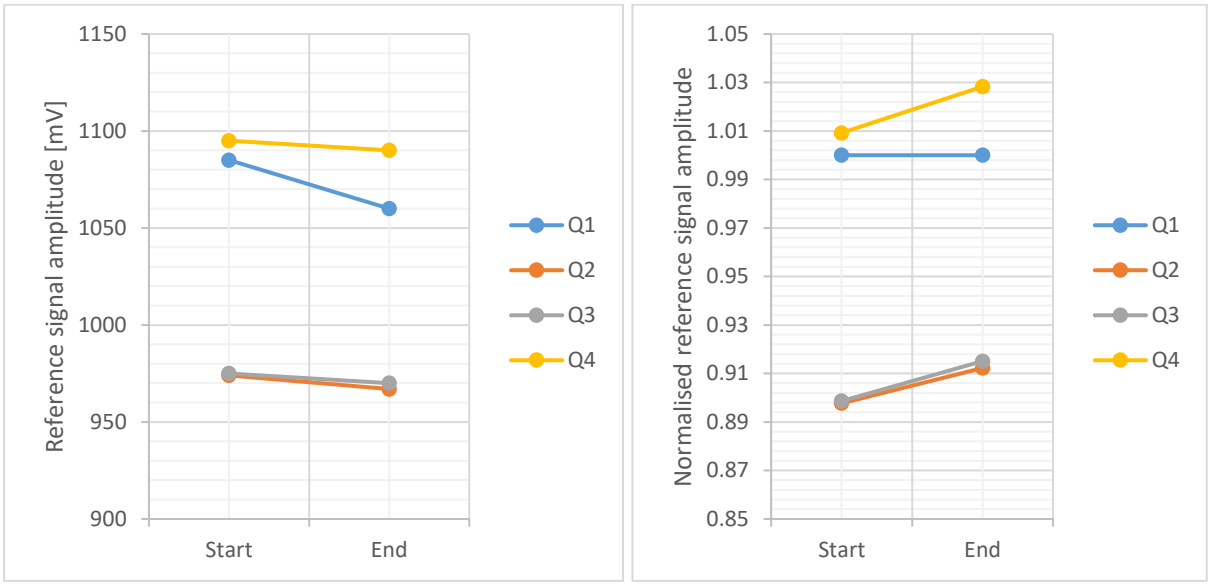

Figure 65: Normalisation values used for the envelope detector measurements, 56°C. Absolute values (left) and normalised scaling factors (right).

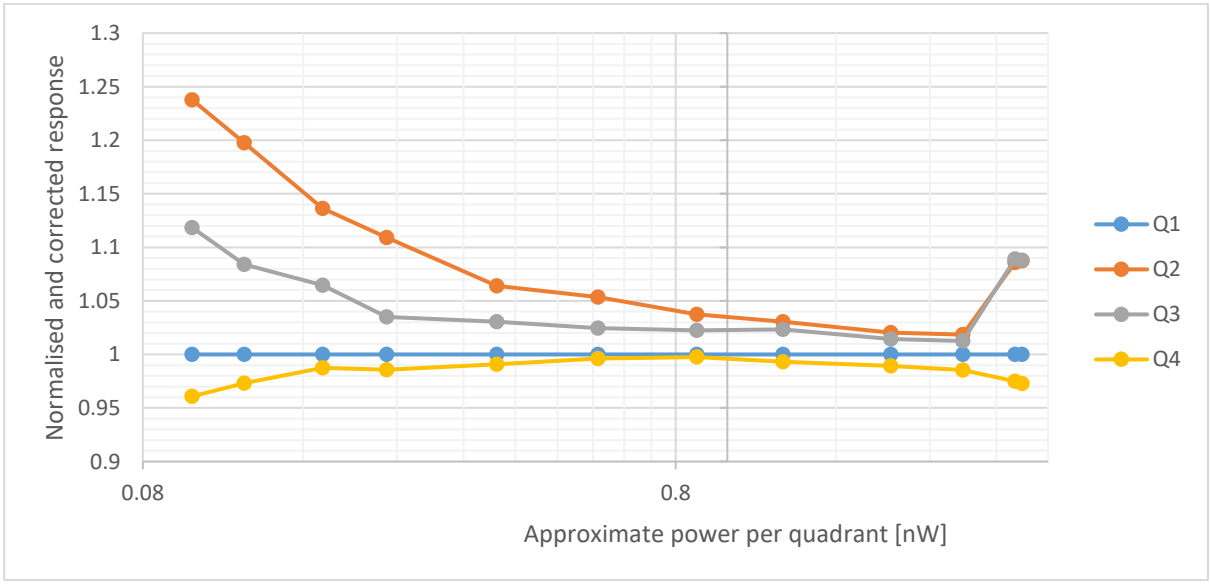

Figure 66: Normalised and corrected envelope detector output voltages, 56°C

The measurements as performed on the envelope detector circuit are repeated on the rectifier circuit. In Figure 67 the normalisation and correction values for the measurement series at ambient temperature are given. Next to a drift for most quadrants, a significant deviation or almost 5% can be observed for quadrant 4. Looking at the resulting normalised and corrected

output response graph in Figure 68 it can be observed that something went wrong in the experimental setup near the end of the measurement series, which caused a jump in signal power on all quadrants, but mainly on quadrant 4. Nevertheless, the deviations between the other channels before this jump and above the minimum light level of $0.3nW$ are small, with the highest deviation visible at quadrant 2 with a deviation of 0.9%, much smaller than the results obtained for the envelope detector. This value can be considered a worst-case result, as this value includes deviations caused by the measurement setup.

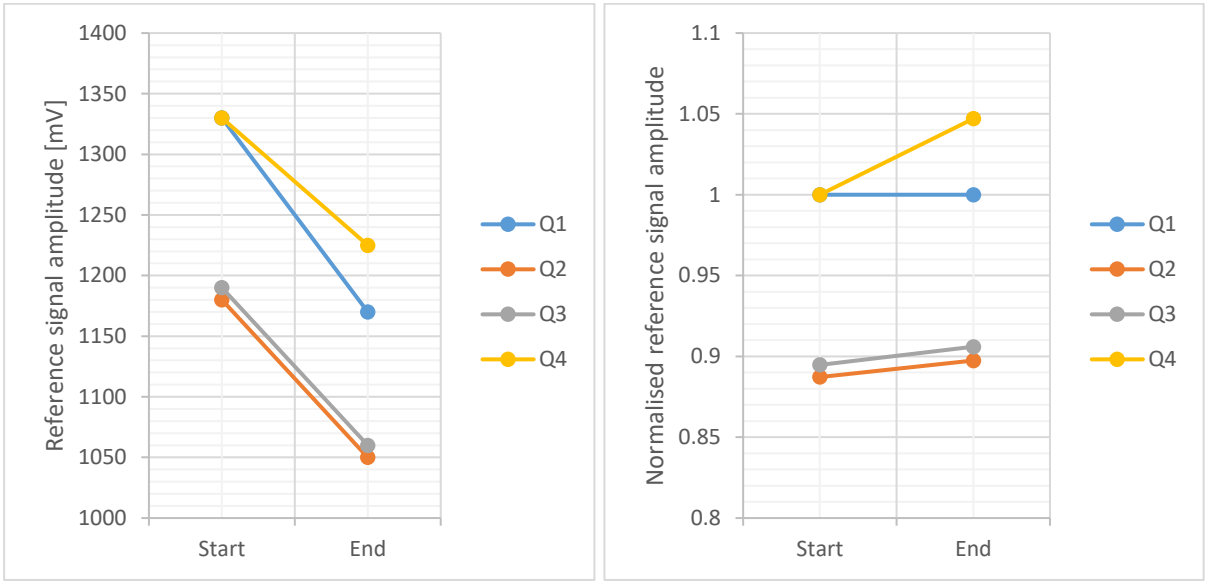

Figure 67: Normalisation values used for the rectifier circuit measurements, ambient temperature. Absolute values (left) and normalised scaling factors (right)

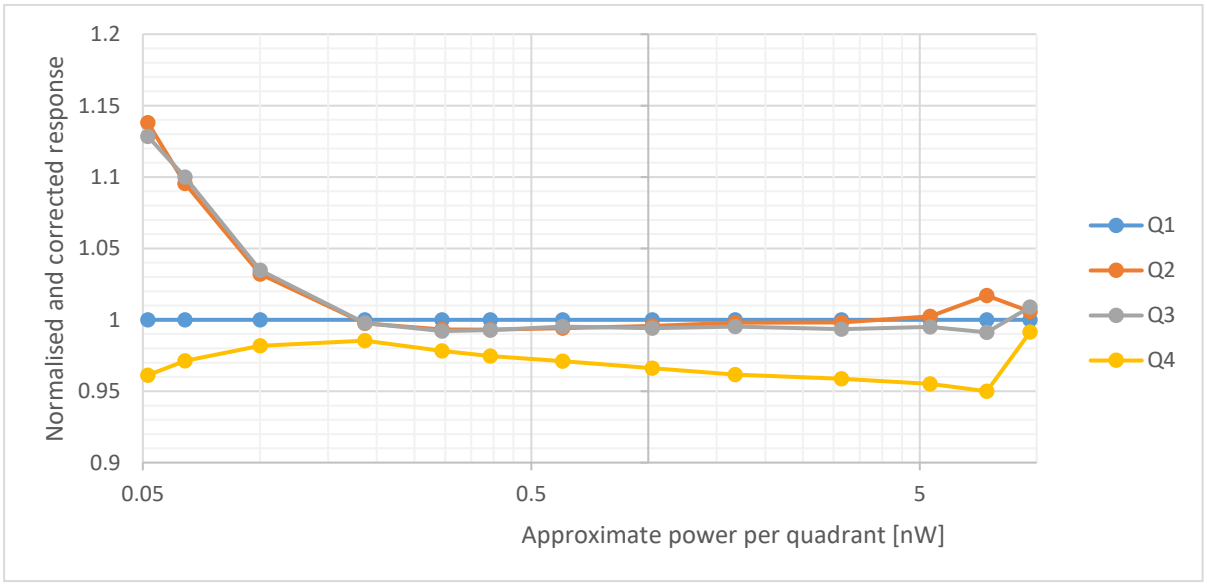

Figure 68: Normalised and corrected rectifier circuit output voltages, ambient temperature

Just as for the envelope detector, the same measurements are performed on the rectifier circuit at elevated temperature. The normalisation and correction values are given in Figure 69. For this measurements series the drift in the experimental setup was much more benign than for the ambient temperature case, with a total drift of approximately 1% for each channel. The resulting characterisation of the rectifier circuit at elevated temperatures is given in Figure 70. The deviations between the four quadrants above the minimum power level of $0.3nW$ are small, the maximum visible deviation is determined to be 1.1%, at quadrant 4. Since this includes errors due to drift in the experimental setup, the actual maximum deviation will be less. It is

also clear that an increased PCB temperature has a negligible effect on the rectifier circuit performance.

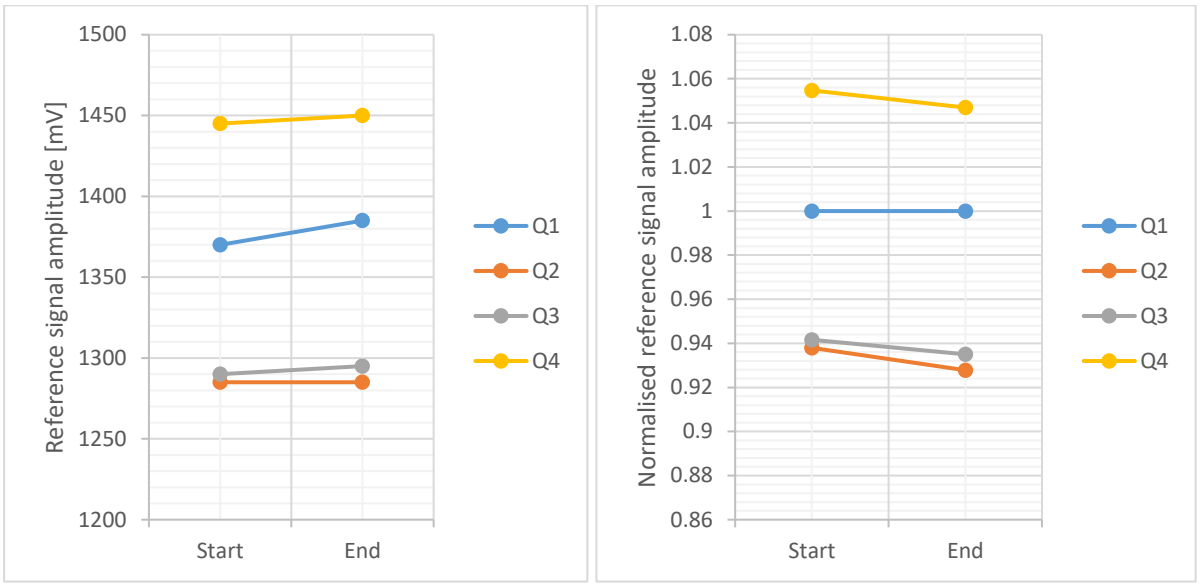

Figure 69: Normalisation values used for the rectifier circuit measurements, 56°C. Absolute values (left) and normalised scaling factors (right).

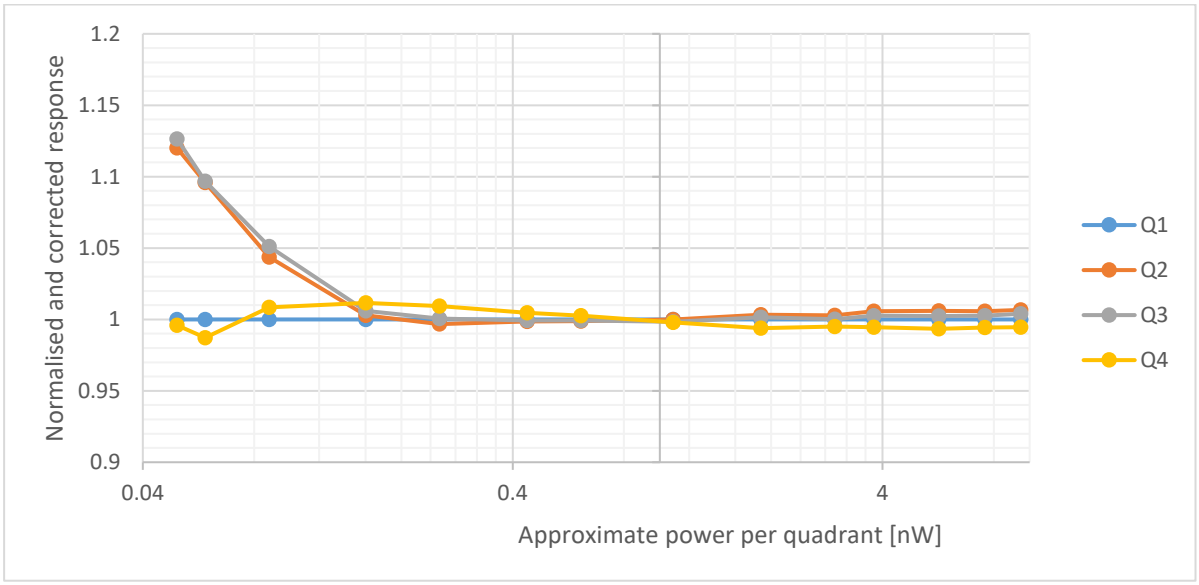

Figure 70: Normalised and corrected rectifier circuit output voltages, 56°C

Using the Keysight DMM the total integrated output noise at the output of the envelope detector and the rectifier circuit is measured. The integrated output noise for the envelope detector is measured to be $2.8mV\ RMS$, for the rectifier circuit this noise is determined to be $1mV\ RMS$. The total noise of $17.9mV$ at the output of the filter stage together with the circuit bandwidth of $100kHz$ and gain of $2 \cdot 10^8$ corresponds to a noise level of $283fA/\sqrt{Hz}$. With the AM-demodulation circuit bandwidth of $1kHz$ an output noise level of $1.8mV\ RMS$ would be expected, which means that the envelope detector adds additional noise to the signal at the output of the filter stage. The rectifier stage appears to reduce the noise at the output of the filter stage, but it should be noted that this is noise is not distributed evenly. In Figure 61 it can be seen that the noise power increases with frequency, so by cutting of this noise at a low frequency a larger portion of the total noise than expected will be removed. The noise at the output of the rectifier output thus corresponds to an effective noise level of $158fA/\sqrt{Hz}$.

To investigate the behaviour of the output noise from the envelope detector and from the rectifier circuit the noise spectrum for both circuits is measured for different input signal magnitudes and for both ambient and elevated PCB temperatures. In Figure 71 the noise spectra for the envelope detector at ambient temperature are given. It can be observed that peaks from the input signal, at $20kHz$, are still present in the output signal from the envelope detector and are quite strong, especially at the maximum input signal power. The low-pass filter at the output from the envelope detector is a simple first-order filter, so a higher order filter might offer better immunity of the envelope detector to the input signal. The envelope detector noise spectra at elevated temperature are given in Figure 72. Although the obtained noise spectra are slightly different from the noise spectra at ambient temperature, no clear trend in these differences can be observed. It should be noted that, as illustrated in Figure 48, the increase in noise around $55kHz$ is caused by the Rigol oscilloscope, not by the envelope detector.

The noise spectra for the rectifier circuit are given in Figure 73 for ambient temperature and Figure 74 for elevated temperature. Similar results as for the envelope detector can be observed, with negligible differences between the results obtained at room temperature and the results obtained at elevated temperature. For the rectifier circuit peaks caused by the input signal are visible in the output signal as well. A notable difference between the envelope detector and the rectifier circuit is that for the envelope detector the noise power increases significantly for lower frequencies, while for the rectifier circuit this increase is much more gradual and benign.

5.3.5. Noise levels overview

The measured noise levels for each output signal as determined in the previous sections are summarised in Table 14. These noise levels are integrated for frequencies above $3Hz$ using the Keysight DMM.

Table 14: Quad cell receiver prototype measured noise levels

Signal	RMS noise level $[mV]$	Input referenced RMS noise $[pA]$
TIA output	0.2	100
Filter stage output	17.9	89.5
Summing amplifier output	4.9	245
Envelope detector output	2.8	14
Rectifier circuit output	1	5

As described in section 5.3.4, the noise at the output of the rectifier circuit corresponds to an effective noise density of $158fA/\sqrt{Hz}$. Looking at the description from [49], while there are different noise sources present in a photodiode detector, the only noise source that is inherent in a photodiode is the shot noise. This is the apparent noise in the output current from a photodiode due to the discrete nature of photons. If an ideal amplifier would be used to amplify this photocurrent that does not add any other noise contributions, and the photodiode would be cooled to low temperatures to prevent thermal noise, the shot noise would still be present in the output signal. The shot noise can therefore be considered the fundamental limit on the lowest noise level that can be achieved in an electro-optical system. The shot noise caused by a photocurrent I_{Ph} is calculated using:

$$I_{shot} = \sqrt{2qI_{Ph}} \tag{45}$$

Where q is the fundamental electron charge and I_{shot} is in $A/\sqrt{Hz}$. With the minimum photocurrent of $0.3nA$ per quadrant, this gives a shot noise of $9.8fA/\sqrt{Hz}$. This means that

there is still quite a difference between the achieved noise level and the theoretically achievable noise level.

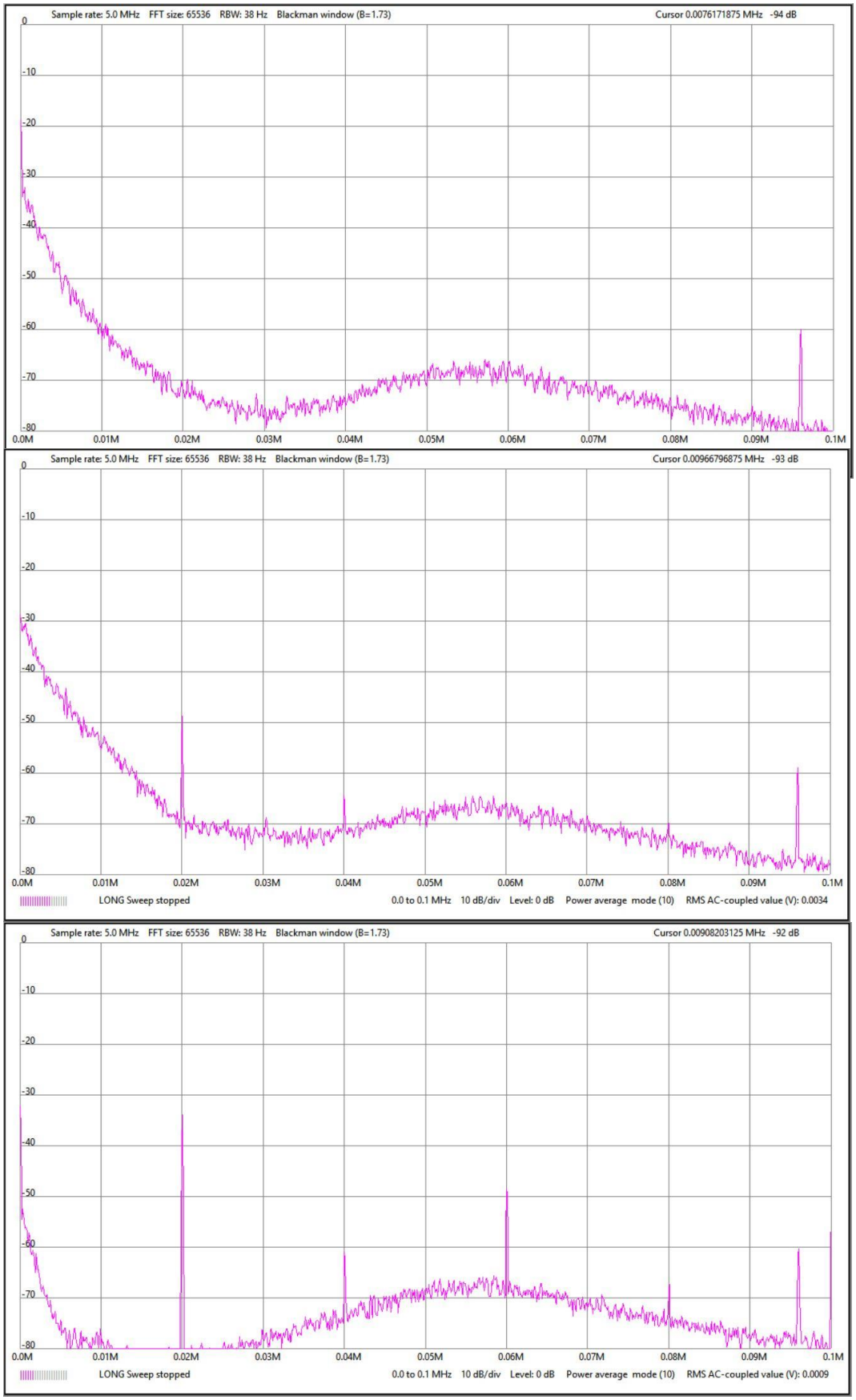

Figure 71: Envelope detector noise spectrum, ambient temperature. No signal (top), minimum signal (middle), maximum signal (bottom)

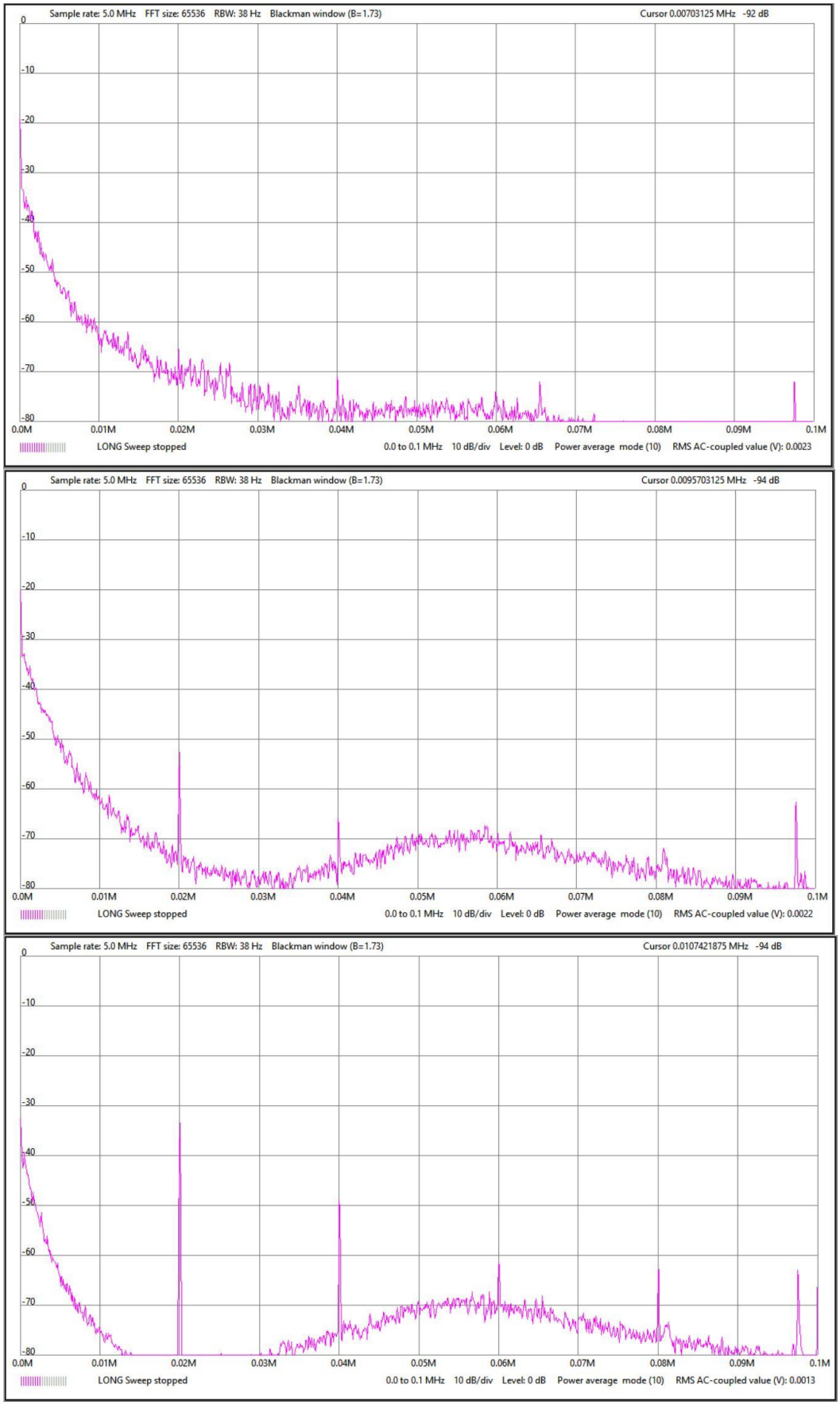

Figure 72: Envelope detector noise spectrum, 56°C. No signal (top), minimum signal (middle), maximum signal (bottom)

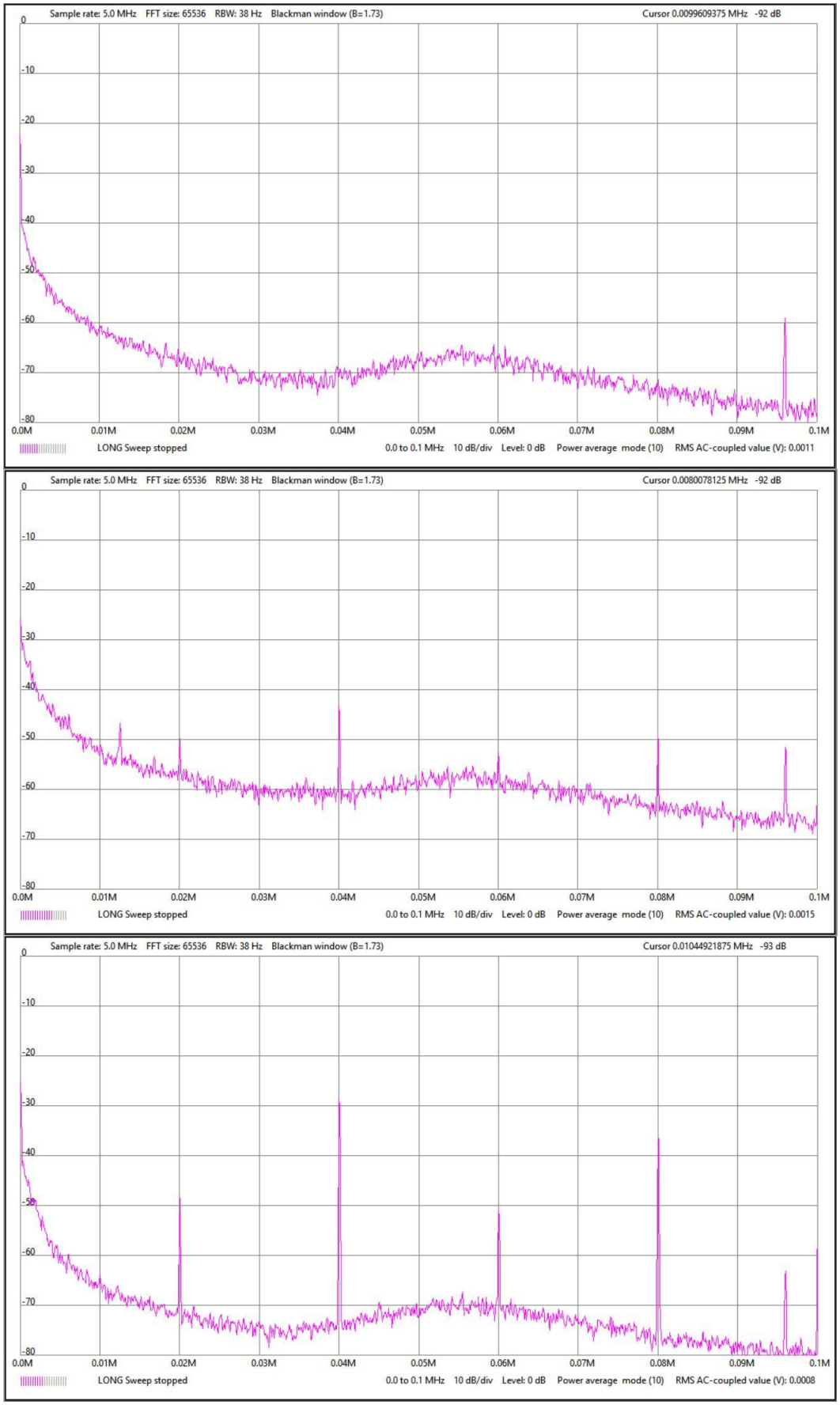

Figure 73: Rectifier circuit noise spectrum, ambient temperature. No signal (top), minimum signal (middle), maximum signal (bottom)

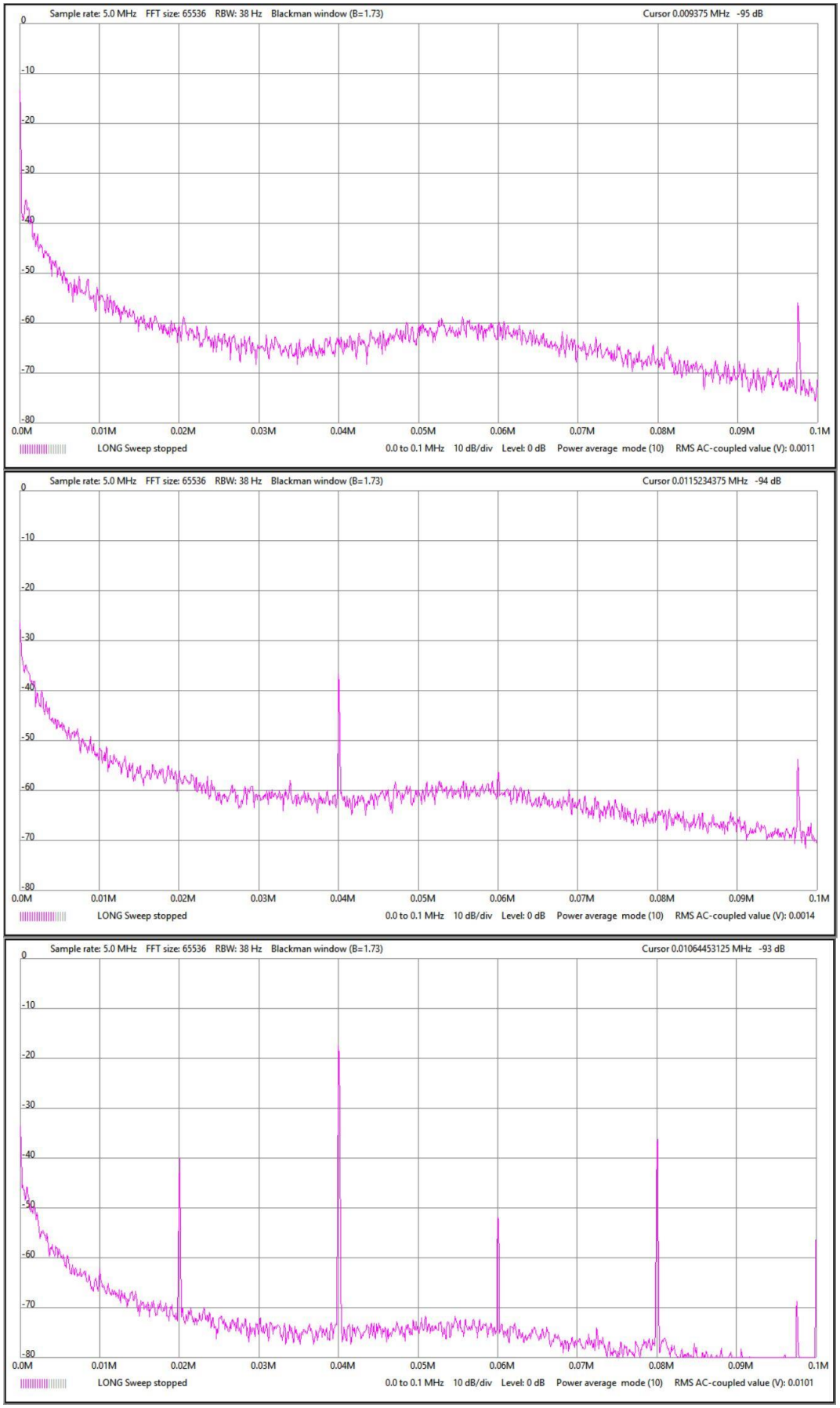

Figure 74: Rectifier circuit noise spectrum, 56°C. No signal (top), minimum signal (middle), maximum signal (bottom)

6 Conclusions & recommendations

6.1. Conclusions

The goal of this work is to describe how a lasercom system can be constructed that fits within the constraints of the CubeSat platform, and that is a commercially viable alternative to radio-based communication systems for CubeSats. To this end, requirements on the lasercom system have been established by Hyperion Technologies that would position this system favourably in the current CubeSat market. These requirements boil down to a target downlink datarate of $1Gb/s$ and a target uplink datarate of $200kb/s$ from a 1U CubeSat module, which has a size of $10 \times 10 \times 10cm$, with a maximum power consumption of $10W$ during communication and $0.5W$ while data is being buffered on this module.

Based on these requirements, a system architecture is proposed with a design solution selected for each required functionality of the lasercom system. To support the statement that this system design will be capable of offering the required performance within the established design constraints, a first-order sizing model is constructed that is capable of estimating the performance of the proposed lasercom system design. This sizing model uses analytical and numerical estimations to quantify the impact of all relevant effects and design parameters on the system performance. Using this model a system design is established that is estimated to achieve the set performance requirements with slightly less power than available during communication with a modelled power consumption of $8.2W$ and slightly more power than requested during data buffering, with a modelled average power consumption of $0.65W$. These results are achieved with an additional signal strength margin of $3dB$ in the uplink and $2.7dB$ in the downlink channels to account for inaccuracies in this first-order sizing model.

Since the constructed sizing model is a first-order model, significant inaccuracies in the predicted system performance can be expected. In order to mitigate this, an assessment is made of the current state-of-art for the use of each component of the proposed lasercom system in a CubeSat application. It is found that while the mechanical and optical design and the photonics are quite mature technologies, some aspects of the proposed electronic design are new or unproven. For this reason the mechanics, optics and photonics are expected to be modelled sufficiently accurately by the first-order sizing model, while for the electronic segment of the lasercom satellite terminal a detailed implementation is evaluated in order to support the assumptions and resulting predictions from the sizing model. The conclusion of this detailed evaluation is that an electronic design can be established using conventional technology that offers the performance necessary for the modelled lasercom system design. The power consumption of the lasercom satellite terminal will however be slightly higher than the power consumption as predicted by the sizing model, with a power consumption of $8.7W$ during communication and a consumption of $0.7W$ during data buffering.

As part of the detailed evaluation of the electronic design of the lasercom satellite terminal one aspect of this design, the quad cell receiver circuit, is evaluated more thoroughly with an experimental test campaign, since this component has to be developed uniquely for this lasercom system. It is however not prohibitively expensive to construct and test a prototype for this component, which makes experimental verification the preferred method for evaluating this component in further detail. This component will amplify and digitise the received uplink data pattern, as well as measure the angle of incidence of the received uplink light in order to correct the pointing of the lasercom satellite terminal. It is found that the noise level at the

output of the pre-amplifier stage in this circuit is much higher than anticipated. While it is assumed that this is partially caused by larger-than-expected stray capacitance in the circuit construction, further measurements indicate that supply voltage or reference voltage noise could play a role as well in this elevated noise level. The input-referenced noise at the output of the amplification stage is measured to be comparable to a photocurrent of $89.5pA\ RMS$, with a noise level of $5pA\ RMS$ for the best-performing angle measurement circuit before digital filtering, which is within the limits as established by the first-order modelled system design. Looking at the theoretical limits on the noise performance, caused by shot noise, it is however theoretically possible to achieve a much better noise performance.

For the accuracy of the angle measurement functionality of the quad cell receiver not only noise levels are relevant, but also further deviations and differences between the four receiver channels. Fixed offsets and differences in gain between the four channels are not measured by the constructed experimental setup, as these error terms can be determined easily during the alignment of the actual satellite terminal in production. Variation in these values under different operating conditions would however be problematic. It was found that in the experimental setup as used to characterise these deviations a drift was present of approximately 1% for most experiments, which causes an unacceptably large additional setup-induced error in the measured deviations. By using an approximate correction method the effects of this drift on the measured performance are reduced. The resulting maximum measured deviation is determined to be 1.1%, but since this value still includes an error term due to imperfections in the experimental setup it is expected that the maximum deviation of 1% as used for the first-order modelled system design will be achieved.

To evaluate the impact of operating temperature on the angle measurement performance, these experiments are repeated at an elevated temperature. It is found that while some aspects of the behaviour of the quad cell receiver circuit change at a different temperature, this deviation is almost equal for all four channels. Since the angle measurement is performed using the ratios of measurements between the four channels instead of using absolute values, this deviation does not impact the accuracy of the quad cell receiver.

Looking at the proposed lasercom system design and comparing this design to the reference lasercom systems as summarised in Table 1 it can be seen that the reference system that is most comparable to the design proposed in this work is the Osiris for BiROS lasercom system. Differences are that for the proposed lasercom system a somewhat better pointing performance is predicted, which allows for a lower downlink laser power. The total power consumption of this satellite terminal is much higher, but it should be noted that multiple components of this terminal are included multiple times in different variants for experimental purposes.

Another reference system that has a comparable design to the proposed lasercom system is the MIT Node. This design uses a similar laser system in the satellite terminal, a different pointing control approach that offers a somewhat worse pointing accuracy and a downlink laser divergence angle that is an order of magnitude larger than the value used in the proposed design. Nevertheless, the estimated datarate of this system is only a factor of 10 lower, so perhaps the error terms in the link budget as considered in this work are evaluated more conservatively.

The results from the detailed evaluation of the electronic design of the lasercom satellite terminal and the results from the experimental verification of the quad cell receiver circuit support the most-unproven and most unknown aspects of the first-order modelled lasercom system design and thereby substantially reduce the uncertainties in this model. Since the other aspects of this model are based on existing and well-established technology, it can be safely concluded that the lasercom system design as proposed in this work is capable of meeting the design requirements as established by Hyperion Technologies, be it with a somewhat higher

power consumption during data buffering than required, and can become a commercially viable and high-performance alternative to radio-based communication systems for CubeSats.

6.2. Recommendations

As the main output of this work is a preliminary system design and not a detailed design for a complete lasercom system, several recommendations can be made for further steps in the development process towards this complete detailed design. As a first step, improvements can be made to the experimental characterisation of the quad cell receiver circuit. Since the measured output errors are of the same order as the drift in the experimental setup, it is likely that the performance of the quad cell receiver will be better than what is currently determined experimentally, but it is not known how much. If the performance of the quad cell receiver is significantly better than predicted perhaps improvements can be made in other aspects of the lasercom system design. To this end the issue of drift in the setup must be solved and ideally some method for measuring the incident light power on the quad cell receiver, such as an optical power meter, must be utilised to verify the assumption that offset- and gain errors in the quad cell receiver can be determined easily during the alignment process of the actual satellite terminal in production.

In the design of the prototype quad cell receiver some areas of improvement are also identified. It is found that the noise at the output of the preamplifier stage is much higher than anticipated. It is expected that stray capacitance in the prototype construction is a contributor to this noise, which can be mitigated with an improved design close to the quad cell sensor, with for example a shorter distance between the sensor leads and the preamplifiers. Other measurements indicate that supply voltage or reference voltage noise could also be a contributor to this increased noise level, so it is recommended to further improve the filtering on these voltage lines.

While the power consumption of the satellite terminal is estimated with sufficient detail in the detailed design evaluation in order to predict that the peak power consumption requirement will be met, and the data buffering average power consumption will be somewhat higher than required, some uncertainties remain in the power consumption of the processor and especially in the power consumption of the FPGA and SSD data buffer, as these power consumptions depend on the precise software implementation of the functionality required from these components. For this reason it is recommended to re-evaluate the power consumption predictions for these components once initial development work on this software implementation has finished.

Lastly, in this report a design for a lasercom system for CubeSats is proposed, based on a first-order sizing approach, with a more thorough analysis for some aspects of this system. Inevitably, assumptions and simplifications are made in this process. For this reason it is recommended to perform system-level tests once a complete prototype system has been constructed to verify that the design as proposed in this work will indeed be able to perform as designed in space. One specific area where an experimental verification is recommended is the closed-loop pointing system of the up- and downlink laserbeams, as this pointing method is quite unique for a CubeSat, by using body pointing of the complete CubeSat in order to point the lasercom terminal. This pointing method can be tested and characterised well on earth.

Bibliography

[1] R. Fields, C. Lunde, R. Wong, J. Wicker, D. Kozlowski, J. Jordan, B. Hansen, G. Muehlnikel, W. Scheel, U. Sterr, R. Kahle and R. Meyer, “NFIRE-to-TerraSAR-X Laser Communication Results: Satellite Pointing, Disturbances, and Other Attributes Consistent With Successful Performance,” Orlando, 2009.

[2] R. Fields, D. Kozlowski, H. Yura, R. Wong, J. Wicker, C. Lunde, M. Gregory, B. Wandernoth and F. Heine, “5.625 Gbps Bidirectional Laser Communications Measurements Between the NFIRE Satellite and an Optical Ground Station,” Santa Monica, 2011.

[3] H. Takenaka, Y. Koyama, D. Kolev, M. Akioka, N. Iwakiri, H. Kunimori, A. Carrasco-Casado, Y. Munemasa, E. Okamoto and M. Toyoshima, “In-orbit verification of small optical transponder (SOTA) –Evaluation of satellite-to-ground laser communication links,” San Fransisco, 2016.

[4] H. J. Kramer, “SOCRATES (Space Optical Communications Research Advanced Technology Satellite),” 2017. [Online]. Available: https://directory.eoportal.org/web/eoportal/satellite-missions/content/-/article/socrates. [Accessed 6 10 2017].

[5] T. Kuwahara, K. Yoshida, Y. Sakamoto, Y. Tomioka, K. Fukuda, M. Fukyama, N. Sugimura and H. Kunimori, “Satellite-to-Ground Optical Communication System on Low Earth Orbit Micro-satellite RISESAT,” Fukuoka, 2012.

[6] T. Kuwahara, K. Yoshida, Y. Tomioka, K. Fukuda and H. Kunimori, “Kuwahara, Toshinori; Yoshida, Kazuya; Sakamoto, Yuji; Tomioka, Yoshihiro; Fukuda, Kazufumi; Fukyama, Masato; Sugimura, Nobuo; Kunimori, Hiroo,” Logan, 2013.

[7] S. W. Janson, R. P. Welle, T. S. Rose, D. W. Rowen, D. A. Hinkley, B. S. Hardy, S. D. La Lumondiere, G. A. Maul and N. I. Werner, “The NASA Optical Communication and Sensors Demonstration Program: Preflight Update,” Logan, 2015.

[8] H. J. Kramer, “AeroCube 7-OCSD (AeroCube - Optical Communication and Sensor Demonstration),” 2016. [Online]. Available: https://directory.eoportal.org/web/eoportal/satellite-missions/a/aerocube-ocsd. [Accessed 6 10 2017].

[9] C. Schmidt, “OSIRIS Update and Outlook,” DLR, Oberpfaffenhofen, 2016.

[10] C. Schmidt, M. Brechtelsbauer, F. Rein and C. Fuchs, “OSIRIS Payload for DLR’s BiROS Satellite,” Kobe, 2014.

[11] E. Clements, “Integration and Testing of the Nanosatellite Optical Downlink Experiment,” MIT STAR Lab, Cambridge, MA, 2017.

[12] D. Sinclair and K. Riesing, “The Rainbow Connection - Why Now is the Time for Smallsat Optical Downlinks,” Logan, 2017.

[13] Micron Technology, Inc., “Technical Note Calculating Memory System Power for DDR3,” Micron Technology, Inc., 2007.

[14] Micron Technology, Inc., “TN5201 LPDDR3 Power Calculator,” Micron Technology, Inc., 2015.

[15] Samsung Electronics, “Samsung SSD 960 PRO M.2,” Samsung Electronics, Suwon, 2016.

[16] K. Petermann, Laser Diode Modulation and Noise, 1st ed., Dordrecht: Kluwer Academic Publishers, 1988.

[17] Thorlabs, Inc., “C-Band Optical Amplifiers (BOAs and SOAs), 1550 nm,” 2018. [Online]. Available: https://www.thorlabs.com/newgrouppage9.cfm?objectgroup_id=3901. [Accessed 31 January 2018].

[18] C. Narayanan, A. Bruce Buckman and I. Busch-Vishniac, “Noise Analysis for Position-Sensitive Detectors,” *IEEE Transactions on Instrumentation and Measurement,* vol. 46, no. 5, pp. 1137-1144, 1997.

[19] S. Kuiper, W. Crowcombe, J. Human, B. Dekker, E. Nieuwkoop, A. Meskers, G. Witvoet, L. Kramer, M. Lemmen, H. Lagemaat, W. van der Hoogt and M. van Koppen, “High-Bandwidth and Compact Fine Steering Mirror Development for Laser Communications,” Hatfield, 2017.

[20] Hamamatsu, “G6849 series datasheet,” Hamamatsu Photonics K.K., Hamamatsu, 2013.

[21] M. Geyer, “Geometric Analysis of an Observer on a Spherical Earth and an Aircraft or Satellite,” U.S. Department of Transportation, Cambridge, MA, 2013.

[22] OSI Optoelectronics, “Photodiode Characteristics and Applications,” OSI Optoelectronics, Hawthorne, 2013.

[23] iXblue, “DR-DG-10-MO-NRZ datasheet,” iXblue, Besancon, 2017.

[24] Gooch & Housego, “HYDRA Mid-Power Booster Erbium-Doped Fiber Amplifier,” Gooch & Housego, Ilminster, 2017.

[25] Gooch & Housego, “High Bandwidth DFB Lasers – AA0701 Series,” Goch & Housego, Boston, 2016.

[26] Thorlabs, “PDQ30C Specsheet,” Thorlabs, Newton, NJ, 2017.

[27] Hyperion Technologies, “CP400.85 Processing Platform Flyer,” Hyperion Technologies, Delft, 2016.

[28] Microsemi Corporation, “Microsemi Power Estimator v3e,” February 2017. [Online]. Available: https://www.microsemi.com/document-portal/doc_download/136554-polarfire-power-estimator. [Accessed 2 February 2018].

[29] B. Klofass, “Planet Labs Ground Station Network,” in *13th Annual CubeSat Developers Workshop*, San Louis Obispo, 2016.

[30] Atmel Corporation, “Atmel SAM E70 datasheet,” Atmel Corporation, San Jose, 2016.

[31] Integrated Silicon Solution, Inc., “IS42SM16800H Datasheet,” ISSI, Milpitas, 2015.

[32] CCSDS, “High Photon Efficiency Optical Communications Coding & Modulation, Proposed Draft Recommended Standard,” CCSDS Secretariat, Washington, 2015.

[33] R. Kumar, K. P. Raju and K. Khasim, “Convolutional Code of Rate 2/3 to Approach the Theoretical Limit Imposed by Shannon’s Channel Capacity,” *International Journal of Computer Science & Technology,* vol. 2, no. 1, pp. 26-29, 2011.

[34] Xilinx, “Single Error Correction and Double Error Detection (SECDED) with CoolRunner-II CPLDs,” Xilinx, San Jose, 2003.

[35] A. Msir, F. Monteiro, A. Dandache and B. Lepley, “Design of a high speed parallel encoder for convolutional codes,” *Microelectornics Journal,* no. 35, pp. 151-166, 2004.

[36] Microsemi, “Polarfire FPGAs,” Microsemi, Aliso Viejo, 2017.

[37] NVM Express Workgroup, “NVM Express revision 1.3,” NVM Express, Inc., Wakefield, 2017.

[38] J. Johnson, “FPGA Drive FMC Schematics,” 5 June 2016. [Online]. Available: http://fpgadrive.com/download/FPGADriveFMC_SCH_RevB-2.PDF. [Accessed 10 February 2018].

[39] Microsemi, “Polarfire Evaluation Kit Board Schematics,” Microsemi, Aliso Viejo, 2017.

[40] Maxim Integrated Products, Inc., “MAX17558 Datasheet,” Maxim Integrated Products, Inc., San Jose, 2016.

[41] Maxim Integrated Products, Inc., “MAX17232 Datasheet,” Maxim Integrated Circuits, Inc., San Jose, 2017.

[42] A. Colder, N. Croitoru, P. D'Angelo, M. DEMArchi, G. Fallica, A. Favalli, S. Leonardi, M. Levalois, P. MArie, R. Modica, P. Rancoita and A. Seidman, “Effects of ionizing radiation on BICMOS components for space application,” Toulouse, 2002.

[43] B. D. Reddell, C. R. Bailey, P. M. O'Neill, K. V. Nguyen, R. Gaza, C. Patel, J. Cooper, T. Kalb, E. Beach and L. Mason, “Compendium of Single Event Effects Test Results for Commercial Off-The-Shelf and Standard Electronics for Low Earth Orbit and Deep Space Applications,” NASA Johnson Space Centre, Houston, 2017.

[44] Maxim Integrated Products, “MAX3795 Datasheet,” Maxim Integrated Products, Sunnyvale, 2004.

[45] Texas Instruments Incorporated, “LM5117 Datasheet,” Texas Instruments Incorporated, Dallas, 2015.

[46] D. Faizullin, K. Hiraki, H.-I. team and M. Cho, “Improvement of sun angle accuracy from in-orbit data of a quadrant photodiode sun sensor,” *International Journal or Research Granthaalayah,* vol. 5, no. 5, pp. 54-67, 2017.

[47] A. Damato, “Envelope effect,” 2007. [Online]. Available: https://en.wikipedia.org/wiki/Envelope_detector#/media/File:Analytic.svg. [Accessed 15 February 2018].

[48] P. Janweijer, “8B/10B Coding, 64B/66B Coding,” Nikhef, Amsterdam, 2008.

[49] M. Gallant, “Transimpedance noise calculation,” 2012. [Online]. Available: http://jensign.com/noise/index.html. [Accessed 8 July 2017].

[50] Analog Devices, Inc., “AD8655 datasheet,” Analog Devices, Inc., Norwood, MA, 2013.

[51] F. Malou, D. Dangle, F. Bezerra, J. Garnier, S. Sifflet, W. Falo and J. Pascal, “Compendium ofTID and SEL Test Results for Various Candidate Spacecraft Electronics,” IEEE, Piscataway, 2007.

[52] H. Zumbahlen, “Sallen-Key Filters,” Analog Devices, Norwood, MA, 2017.

[53] Analog Devices, Inc., “AD8628 Datasheet,” Analog Devices, Inc., Norwood, MA, 2014.

[54] Public domain, “Opamp summing amplifier,” 26 January 2009. [Online]. Available: https://commons.wikimedia.org/wiki/File:Op-Amp_Summing_Amplifier.svg. [Accessed 20 February 2018].

[55] R. Habash, “ELG4136 Lecture 8,” University of Ottawa, Ottawa, 2017.

[56] Atmel Corporation, “ATxmega64A4U Datasheet,” Atmel Corporation, San Jose, 2014.

[57] Maxim Integrated Products, Inc., “MAX8902 Datasheet,” Maxim Integrated Products, Inc., San Jose, 2015.

[58] Texas Instruments, “SN74LVC1G3157 Datasheet,” Texas Instruments, Dallas, 2017.

[59] J. Karki, “Active Low-Pass-Filter Design,” Texas Instruments, Dallas, 2002.

[60] R. Harboe-Sørensen, M. R. Hailey, B. Nickson and P. D. Thomas, “Radiation Testing to Determine the TID Susceptibility and SEL LET Thresholds of COTS Devices, 13 Different Types, for the GAIA Project,” ESA/ESTEC, Noordwijk, 2007.

[61] Analog Devices, Inc., “AD8027 Datasheet,” Analog Devices, Inc., Norwood, MA, 2015.

[62] Keysight Technologies, “Keysight 34461A Datasheet,” Keysight Technologies, Santa Rosa, 2017.